Electron beam generation and structure of defects in carbon and boron nitride nanotubes

Alberto Zobelli

Université Paris-Sud XI
Technische Universität Dresden

THESIS

presented for obtaining
the doctor degree in physics by

Alberto Zobelli

ELECTRON BEAM GENERATION AND STRUCTURE OF DEFECTS IN CARBON AND BORON NITRIDE NANOTUBES

Defended October 3, 2007 in front of the jury composed by

Alexandre REVCOLEVSCHI ..	*President*
Christian COLLIEX	*Thesis directors*
Gotthard SEIFERT	
Florian BANHART	*Reporters*
Laurent PIZZAGALLI	
Christopher P. EWELS	*Examinators*
Alexandre GLOTER.....	
Thomas HEINE.....	

ABSTRACT

The nature and role of defects is of primary importance to understand the physical properties of C and BN single walled nanotubes. Transmission electron microscopy (TEM) is a well known powerful tool to study the structure of defects in materials. However, in the case of SWNTs, the electron irradiation of the TEM may knock out atoms. This effect may alter the native structure of the tube, and has also been proposed as a potential tool for nanoengineering of nanotubular structures.

Here we develop a theoretical description of the irradiation mechanism. First, the anisotropy of the emission energy threshold is obtained via density functional based calculations. Then, we numerically derive the total Mott cross section for different emission sites of carbon and boron nitride nanotubes with different chiralities. Using a dedicated STEM microscope with experimental conditions optimised on the basis of derived cross-sections, we are able to control the generation of defects in nanotubular systems. Either point or line defects can be obtained with a spatial resolution of a few nanometers.

The structure, energetics and electronics of point and line defects in BN systems have been investigated. Stability of mono- and di- vacancy defects in hexagonal boron nitride layers is investigated, and their activation energies and reaction paths for diffusion have been derived using the nudged elastic band method (NEB) combined with density functional based techniques. We demonstrate that the appearance of extended linear defects under electron irradiation is more favorable than a random distribution of point defects and this is due to the existence of preferential sites for atom emission in the presence of pre-existing defects, rather than thermal vacancy nucleation and migration.

Resumé La nature et le rôle de défauts est de première importance pour la compréhension des propriétés physiques des nanotubes monoparoi (SWNT) de carbone et nitrure de bore. La microscopie électronique en transmission (TEM) est un outil très puissant pour l'étude des défauts dans les matériaux mais dans le cas de SWNT les atomes peuvent aussi être éjectés par l'irradiation électronique. Cet effet peut changer la structure initiale du tube mais peut être également vu comme un outil potentiel pour "usiner" des structures nanométriques.

Nous avons développé un outil théorique pour la description du mécanisme d'irradiation. Dans un premier temps, nous avons dérivé, par des calculs basés sur la théorie de la fonctionnelle de densité, la carte des seuils d'énergie d'émission. Ensuite, nous avons dérivé numériquement la section efficace total de Mott pour différents sites d'émission dans des nanotubes de carbone et nitrure de bore. Utilisant un microscope STEM, nous avons été capables de contrôler la génération de défauts dans des systèmes nanotubulaires avec des conditions expérimentales optimisées sur la base de nos calculs de section efficace. Défauts ponctuels ou lignes de dislocation peuvent ainsi être obtenus avec une résolution spatiale de quelques nanomètres.

La structure, l'énergie et les propriétés électroniques des défauts ponctuels et des lignes de défauts ont été étudiées dans les systèmes de BN. L'énergie d'activation et les chemins réactionnels pour la diffusion de mono et de bi-lacunes dans du BN hexagonal ont été dérivés en utilisant le "nudged elastic band method" combiné avec les techniques basées sur la fonctionnelle de la densité. Nous avons aussi démontré que l'apparition de défauts étendus est plus favorable qu'une distribution aléatoire de défauts ponctuels et que cela est dû à l'existence de sites préférentiels pour l'émission d'atomes en présence de défauts préexistants plutôt qu'à des phénomènes de migration et nucléation thermique des lacunes.

Kurzzusammenfassung Die Art und die Rolle der Defekte ist von größter Wichtigkeit für das Verständnis der physikalischen Eigenschaften der einwändigen Kohlenstoff- und Bornitrid-Nanoröhren. Das Transmissionselektronenmikroskop ist ein sehr leistungsfähiges Instrument für die Strukturananalyse von Materialdefekten. Jedoch kann die im TEM herrschende Elektronenbestrahlung Atome aus einwändigen Nanoröhren herausstoßen. Einerseits kann dieser Effekt die ursprüngliche Struktur der Nanoröhre verändern, andererseits kann er aber auch als eine Möglichkeit zum Bearbeiten von nanoröhrenartigen Strukturen aufgefasst werden (nanoengineering).

Wir haben eine theoretische Beschreibung des Bestrahlungsmechanismus entwickelt. Zuerst haben wir mit Hilfe von dichtefunktionalbasierten Berechnungen den richtungsabhängigen Schwellenwert der Ausstoßenergie ermittelt. Anschließend haben wir numerisch den vollständigen Mott-Wirkungsquerschnitt für unterschiedliche Ausstoßstellen in Kohlenstoff- und Bornitrid-Nanoröhren

unterschiedlicher Chiralitäten hergeleitet. Indem wir ein Rastertransmissionselektronenmikroskop (STEM) in mit Hilfe des hergeleiteten Wirkungsquerschnittes optimierten Versuchsbedingungen benutzt haben, konnten wir die Defektbildung in nanoröhrenartigen Systemen kontrollieren. Punkt- und Liniendefekte können auf diese Weise mit einer Ortsauflösung von wenigen nm erzeugt werden.

Die Struktur, die Energie und die elektronischen Eigenschaften der Punkt- und Liniendefekte in Bornitridsystemen sind untersucht worden. Die Aktivierungsenergien und die Reaktionswege der Diffusion und der Bildung von Einzel- und Doppelgitterlücken wurden mit Hilfe der mit dichtefunktionalbasierten Methoden kombinierten "nudged elastic band method" (NEB) hergeleitet. Wir haben auch gezeigt, dass die Bildung von langen Liniendefekten gegenüber einer Zufallsverteilung der Defekte vorteilhafter ist, und das dies eher aufgrund der Existenz von präferenziellen Atomausstoßstellen in der Gegenwart von vorher entstandenen Defekten als aufgrund der thermischen Migration der Gitterlücken der Fall ist.

TABLE OF CONTENTS

List of Figures, Tables and Abbreviations

List of Figures

List of Tables

List of Abbreviations

BN-NT	Boron nitride nanotube
DFT	Density functional theory
DFTB	Density functional tight binding
EELS	Electron energy loss spectroscopy
h-BN	Hexagonal boron nitride
HREM	High resolution electron microscopy
LDA	Local density approximation
MD	Molecular dynamics
MEP	Minimum energy path
MWNT	Multi walled nanotube
NEB	Nudged elastic band method
STEM	Scanning transmission electron microscope
SWNT	Single walled nanotube
TEM	Transmission electron microscopy

AKNOWLEDGEMENTS

I would like here to express words of gratitude to all those who helped to make this thesis possible.

I must firstly acknowledge my two thesis supervisors, Christian Colliex and Gotthard Seifert, for having allowed me to conduct my thesis in the best conditions. I'm particularly grateful for the precious freedom and independence they allowed me in conducting my research.

This thesis would not be possible without the daily help of Alexandre Gloter and Chris Ewels. To them goes all my gratitude for their support, guiding and working very close to me during these years.

A special thank to the European comunity and the European network "Fullerен like materials" for financial support, for the possibility to work by different network members and for many trips and nice restaurants all around Europe.

The kind help of Stefan Csillag, coordinator of the network, made possible this great scientific and human experience. A big thanks to Stefan also for having hosted me for a long period in Sweden and having given the possibility to use the microscopes in Stockholm and Uppsala.

Malcolm Heggie has kindly supported a long period of this thesis. Thanks to him for the many visits in Brighton and pleasant conversations.

At the beginning of this thesis there was the kind attention of Odile Stefan: it is mainly thanks to her that I got the possibility to spend a pre-doctoral period that has successively evaluated in this thesis.

Some of the best results presented in this work are due to the continuous developments done on the STEM microscope by Marcel Tence whom I would like to express my gratitude.

I would like to remember here also all the colleagues in Orsay and Dresden that I have work with during these years. With them I got the possibility to work in a pleasant environment and to share good moments also outside the lab walls.

Aside from my colleagues I must thank all my friends in Italy, France and Germany for providing a fundamental non work-related support.

On a more personal level I'm grateful to my mother and father for their unending encouragement during my academic studies. Even from far away their support has been a big help for me.

Finally, I offer my heartfelt thanks to Vika for being a devoted and wonderful companion during these years. *Grazie Vika!*

.. e osservar gli effetti della natura che, quantunque appariscano minimi e di nessun conto, non devono mai dal filosofo disprezzarsi, ché le operazioni di natura son tutte in pari grado degne di maraviglia; e perché anco da cose comuni, direi in certo modo vili, si posson trarre notizie molto curiose e nuove, e bene spesso remote da ogni immaginazione.

***

Galileo

CHAPTER 1

INTRODUCTION

> Writing in English is the most ingenious torture ever devised for sins committed in previous lives.
>
> James Joyce

PROGRESS on the synthesis processes in material science has made available in the last twenty year a large number of systems structured at a nanometrical scale. After more than twenty years since the discovery of fullerenes [1], nanoscience has become now a mature field of research covering a broad range of topics and it is still a rapidly growing domain. During the last years the transfer of nanosystems from the laboratories to real technological applications appears more feasible.

The landmark publication of the new nanotubular phase of carbon by S. Ijima in 1991 [2] has represented one of the major progress in nanoscience. Nanotubes structure corresponds to the rolling of the hexagonal lattice of a single or several graphite sheets into a cylindrical molecular structure. In the past years nanotubes have been successfully sythetized from a large number of different layered materials as BN [3], WS_2 [4], MoS_2, TiO_2 etc. Between these materials boron nitride (BN) in its hexagonal phase has the structural parameter the closest to the one of graphite.

Nanotubes have unique electronic and mechanical properties that make them potentially useful in a wide variety of applications. A large number of studies have demonstrated that carbon nanotubes have an extremely high strength resistance, they are good heat conductors and they can be either unidimensional metallic conductors or semiconductors depending from their chirality. However, the presence of defects in the tube lattice [5, 6] can strongly affect the original properties of the perfect nanotubes, with a degradation or improvement of specific chemical or physical characteristics. On this basis it appears of fundamental importance to know the

exact role played by different defective structures in setting up the effective electronic, chemical and mechanical properties of the tubes. Furthermore, a correct description of the dynamics of defect formation and their thermodynamical behavior should open new possibilities for the functionalisation through a controlled creation of specific defective structures.

The current synthesis methods do not produce perfect nanotubes. Basically, native defects appears at the synthesis since entropy and kinetics of synthesis reactions could stack the system into metastable defective states without reaching the structural ground state of the defect free nanotube. Afterwards, the handling of nanotubes samples can also provoke the appearance of defective structures. Chemical treatments are largely used for the side functionalisation of the tubes and chemical attacks are also used for opening the nanotube caps in the synthesis of filled nanotubes. These procedures deeply modify the morphology of the tubes through bond breaking and atom removal. Nanotube irradiation can also be deliberately used to alter the chemical, mechanical and electronic properties of the tubes. However irradiation is also an unavoidable secondary effect occurring when highly energetic particles are used to investigate structural and spectroscopic properties of the tubes.

Useful insights on irradiation effects can be obtained from the data on the irradiated bulk however many traditional concepts of irradiation physics are not directly applicable to nano-materials. Furthermore irradiating nanostructured systems can more dramatically affect specific physical properties appearing at such reduced dimensional scale.

Irradiation experiments on nanotubes have been performed using many different energetic particles, such as γ rays [7, 8], electrons [9, 10], protons [11, 12] and ions [13], on a large variety of tubular systems. It has been widely demonstrated that through irradiation it is possible to obtain alteration of nanotube properties of primary importance for application. For example Kis and coworkers [10] have shown a strong stiffening of bundles of carbon nanotubes after electron irradiation. In the work of Gomez-Navarro and coworkers [13], an Ar^+ ion bombardment of carbon nanotubes provoked a dramatic increase in the tube electrical resistivity.

Irradiation as a side effect of analytical experimental techniques is of particular importance in transmission electron microscopy (TEM). Compared to non-spatially resolved techniques, electron microscopy allows the observation of individual nanotubes at the cost of a consequent high irradiation density. The energetic electrons of the beam (energy of the order of magnitude of 100 keV) are capable of removing single atoms from the

lattice through direct knock-on collisions [14, 15]. It is now well demonstrated that TEM can be a powerful technique for imaging defective structures generated by the *in-situ* irradiation of the microscope electron beam itself. As an example Hashimoto and coworkers have shown the appearance of single vacancies and dislocation lines in single graphitic carbon layers [16]. More recently further experiments on single walled carbon nanotubes heated above 2000 K have shown the first images of pentagonal and heptagonal rings associated with Stone-Wales bond rotations [17]. These latest structures were previously theoretically predicted to be stable [18] but they were never been directly imaged before.

In spite of the recent improvements in microscopy techniques that have shown the possibility of creating and imaging defects, defect generation in nanotubes is still largely an uncontrolled process. In standard microscopy techniques, samples are homogeneously irradiated and defects appear randomly all over the illuminated zone which eventually leads during observation to extended wavy morphologies up to a complete tube amorphisation [19]. The crystallinity of the tube can be eventually preserved during the TEM observation through thermal treatments [20, 21, 22, 23] that promotes migration and nucleation of vacancies produced by irradiation [24, 25, 26]. Other works have shown that through the use of focused probes is possible to modify the structure of multiwalled carbon nanotubes at a nanometrical scale [27, 28].

The cited works show a relative control on the irradiation process but the potentialities related to electron irradiation into a transmission electron microscope are still far from being completely enlighted. Microscopy experiments are usually not conducted at optimal irradiation conditions mainly due to a certain inaccuracy in the description of irradiation processes and of defects thermal behavior. Furthermore microscopy images show both point and extended defects but to date no work have clearly linked the formation and transition from point to line defects in nanotubes. Finally numbers of questions remain open on the morphological modifications induced by irradiation and on their effective role in the changes of nanotubes physical and chemical properties. Once these questions will find an answer, electron irradiation could be realistically used as a precise tool for functionalising the nanotubes.

In this thesis work we will tackle different aspects regarding electron irradiation of single walled carbon and boron nitride nanotubes. This study has been conducted both theoretically and experimentally using transmission electron microscopy techniques and theoretical simulations based on

the density functional theory. We will see how theoretical simulations from one side can provide a fundamental contribution for a correct interpretation of experimental results and from an other side give an essential insight in the design of further irradiation experiments.

In spite of the structural similitude between carbon and BN nanotubes, few studies have been addressed on this relatively new material. The stability of boron nitride based nanotubes have been first theoretically proposed by Rubio *et al.* shortly after the discovery of carbon nanotubes [29]. Multiwalled BN nanotubes have been successively synthesized by Chopra *et al.* [3] using a simple arc discharge technique and currently their production is routine in a number of laboratories. The synthesis of single walled nanotubes is a more difficult task. Introducing catalytic particles in the electrods of an arc discharge reactor Loiseau *et al.* [30] have firstly obtained single walled nanotubes. The efficiency in the synthesis of single walled BN nanotubes have been improved through a catalyst free process using laser ablation of a h-BN target [31]. However the current synthesis procedure does not produce samples of a purity comparable to the one of single walled carbon nanotubes. The importance of BN nanotubes as new wide band gap nanomaterial is primarily due to their homogeneous electronic behavior: tubes of different chiralities are all semiconductors with almost the same theoretical optical band gap of 6.2 eV [32, 33] and experimentally determined at 5.8 eV [34]. However, as for carbon nanotubes, boron nitride nanotubes are not defect free. Although there have been some theoretical studies of individual isolated native [35, 36, 37, 38] and mechanically induced defects [39, 40], there is no experimental identification of point or line defects in such nanotubes, or studies of their interaction and aggregation. Moreover, the important case of divacancies has not yet been treated.

This thesis is structured as follows. An overview of the different experimental and theoretical methods used during this thesis will be given in chapter 2. In the first part of the chapter we will illustrate the basis of transmission electron microscopy with a particular attention addressed to scanning transmission microscopy, technique used in experiments of local electron irradiation. In the second part of the chapter we will describe the basis of the density functional theory which represents an efficient method for solving the many-body Schrödinger equation of complex systems. In many of the investigated problems the size of the structures or the time scale of the system evolution would have made the use of standard DFT techniques too time consuming. For this reason we have largely used the

density functional theory in its tight binding approximation (DFTB) whose principles will be given in chapter 2. In the conclusion of the chapter we will illustrate an "automatic" way for finding complex reaction paths represented by the nudged elastic band method (NEB).

In the third chapter of this thesis several experimental and theoretical aspects concerning defects in single walled BN nanotubes will be addressed. Firstly we will present a complete study of structure and energetics of mono- and di- vacancies in h-BN and BN nanotubes. High resolution experiments have successively been performed on single walled BN nanotubes that have been provided to us by R. Arenal de la Concha and A. Loiseau[1] (details of the synthesis of the tubes are reported in Refs. [31, 41]). HREM images will show the appearance under electron irradiation of both single point defects and extended dislocation lines on the tube walls. The route for going from a simple single vacancy picture to extended defective structures will be discussed in details considering both vacancy thermal stability and a possible migration-nucleation mechanism and the existence of preferential sites for vacancy creation under electron irradiation. Using the nudged elastic band method we will derive activation energies and reaction paths for diffusion and nucleation of mono- and di- vacancy defects in hexagonal boron nitride layers. The temperature dependence of entropic and vibrational contributions to the free Gibbs energies will be explicitly taken into the description of the phase diagram for vacancy migration. Extending the analysis of the formation energies, we will show that clustering of multiple vacancies is energetically favorable and leads to extended defects which locally change the nanotube diameter and chirality. The chapter will conclude on the electronic configuration of defects and on their possibility to affect on the electronic and optical properties of the tubes.

Despite the large interest shown in recent years for nanotube electron irradiation a complete description of the sputtering cross section is still missing. The analysis of formation energies of different defective structures gives only an indirect insight on their creation probability under electron irradiation. A more correct description should explicitly consider the dynamics of atom sputtering and the energy barrier that should be overpassed. These problems will be discussed in chapter 4 where we will give a theoretical description of irradiation of carbon and boron nitride nanotu-

[1] Laboratoire d'Etudes des Microstructures, UMR 104 CNRS-ONERA ONERA B.P. 72, Châtillon, France.

bes. In a first step the anisotropy of the atomic emission energy threshold will be obtained within extended molecular dynamics simulations based on the density functional tight binding method. In a second step, we will numerically derive the total Mott cross section for different emission sites as a function of the incident electron energy. Extending the calculations to defective carbon nanotubes we will provide a direct proof of the existence of a "laddering" mechanism which promotes the appearance of long defective lines.

The calculations of the total knock-on cross section for various nanotubes can be used as a guideline for the optimisation of irradiation conditions in TEM experiments. In chapter 5 we will show a series of experiments of local electron irradiation conducted within a STEM microscope. Localised morphological modification of nanostructured systems through electron irradiation have been reported up to now only on the large multiwalled nanotubes. On the basis of the previously derived cross sections and using a subnanometrical electron probe we will show the possibility of a nanometrical control of the defect production on single walled carbon and boron nitride nanotubes. In particular we will show the possibility to reshape the nanotubes and to locally change their chirality at a nanometrical scale.

In chapter 6 we will conclude on the different perspective that this work might open. If electron irradiation have been seen up to now as a side effect on TEM experiments we believe that its control as a post-synthesis treatement could positively be used in the local tuning of physical and chemical properties of nanostructured systems.

CHAPTER 2

EXPERIMENTAL AND THEORETICAL TECHNIQUES

THIS THESIS has investigated defective structures and electron irradiation in carbon and boron nitride nanotubes both from a theoretical and an experimental point of view. In particular, we have combined transmission electron microscopy experimental techniques with theoretical simulations based on the density functional theory. This chapter gives a basic overview of the experimental and theoretical techniques used in this thesis work. During the first part of the chapter we will give an over view of the different microscopy techniques used throughout this work. In particular standard trasmission electron microscopy techniques, that will be illustrated in section 2.1, have been employed for direct imaging of individual defective structures in single walled BN nanotubes. In section 2.2 we will focus on the scanning transmission electron microscopy (STEM) used as a tool for shaping the nanotubes through a localised electron irradiation. In the second part of the chapter we will illustrate the basis of the density functional theory (§ 2.4) and how it has been implemented into the `AIMPRO` code (§ 2.5). Standard density functional techniques become rapidly too time consuming for the study of systems with a large number of atoms, as it is for defective nanostructures. In Sec 2.6 we will present the tight binding approximation of the density functional theory (DFTB) that allows to calculate systems of thousand of atoms. For concluding in Sec. 2.7 we will describe the nudged elastic band method (NEB), a computational procedure to detect transition states and migration paths, and its efficient combination with the DFTB method.

2.1 Transmission electron microscopy

Figure 2.1 gives a simplified schematic representation of a conventional transmission electron microscope (TEM). A field emission gun generates a

stream of monochromatic electrons that are accelerated at a usual operating energy in the range between 80 and 300 keV. These electrons are then transferred by a system of condenser lenses into a thin parallel beam. At this stage, the beam is restricted by the condenser aperture, eliminating electrons travelling at high angle (those far from the optic axis). The beam illuminates then the sample and is partially transmitted. An objective lens focuses the transmitted electrons into an image which is successively enlarged by an optical system made of several intermediate and projector lenses. The final image is observed on a phosphor screen or on other detection systems such as photo films or CCD cameras. Several optional objective and selected area metal apertures can restrict the beam. The objective aperture enhances contrast by blocking out high-angle diffracted electrons. The selected area aperture enables the user to define the specimen area selected for the acquisition of difffraction patterns.

Compared to conventional microscopy, high resolution transmission electron microscopy (HRTEM) does not use amplitudes, *i.e.* absorption by the sample, for image formation. On the contrary, contrast arises from the self-interference in the image plane of the electron wave itself. This allows to image cristallographic or amorphous structures at an atomic scale and makes HRTEM one of the main tools for morphological studies of solids, nanostructures and biological samples. The interference process resulting in high resolution images formation (where each imaging electron interacts independently with the sample) have been described in many text books [42]. At the sample surface, the wave function of an incident electron can be approximated as a plane wave. The electronic plane wave invests homogeneously the specimen which diffracts the incident wave in a set of plane waves whose frequencies correspond to the distribution of spatial frequencies of the sample crystal structure.

The case of single walled nanotubes imaging (light element and limited amount of projected atoms) can be considered as an ideally thin material and belongs to the usually called weak phase object approximation. For such thin specimens the plane wave function will experience a position dependent phase shift that is related to the total projected atomic potential of the specimen. A frequence dependent dephasing is then introduced by the spherical aberrations and the defocusing properties in the microscope optics. An image is finally produced whose contrast arises from the interference between different diffracted waves. For a HREM-TEM sytem, several resolution limits may be defined such as point resolution and information limit. Point resolution is defined as the smallest detail that can

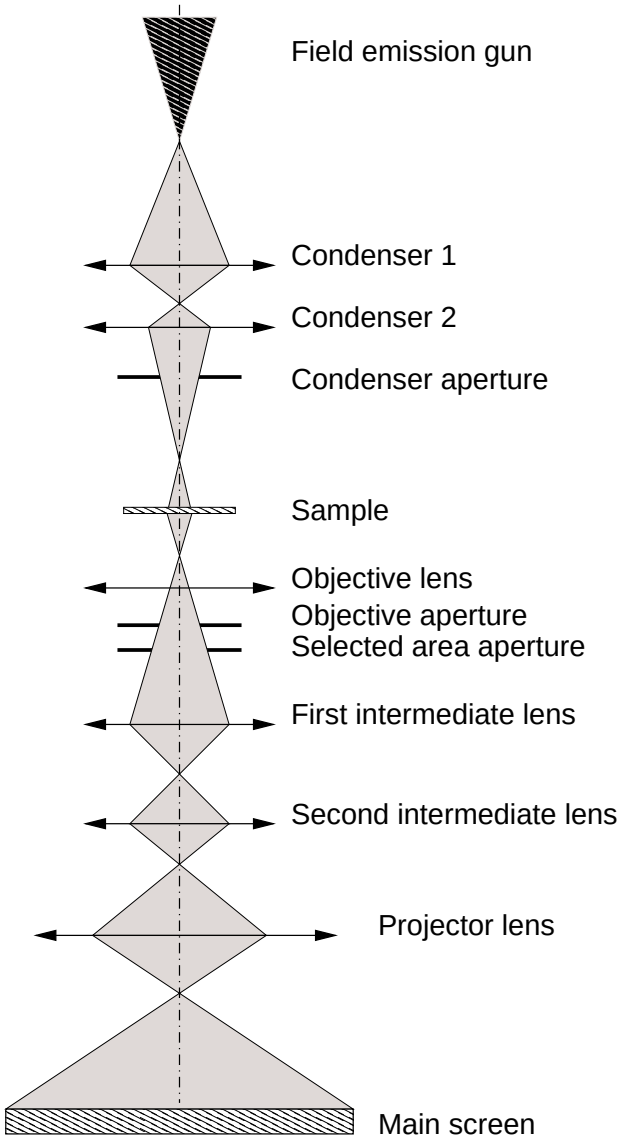

Figure 2.1: *Simplified schematic representation of a transmission electron microscope.*

be interpreted directly from the experimental images in terms of the structure, provided that the object is very thin. The information limit represents the smallest detail that can be resolved by the instrument. It is inversely proportional to the highest spatial frequency that is still transferred with appreciable intensity from the electron wave field at the exit plane of the specimen to the image plane.

2.1.1 Experimental set-up

High resolution images presented in this thesis have been obtained at the Ångstrom physics laboratory in the Uppsala University. The laboratory is equipped with a FEI Tecnai F30 transmission electron microscope. The instrument is equiped with a Schottky field emission gun and operates to a maximum accelerating voltage of 300 kV. The system has a point resolution of 0.19 nm and an information limit of 0.12 nm.

2.2 The STEM microscope

Experiments of local irradiation of single walled nanotubes have been cunducted using a dedicated scanning transimission microscope (STEM). A schematic representation of a STEM microscope is given in Fig. 2.2. Electrons are emitted by a cold field emission gun (FEG) which gives a natural energy width of the electron beam limited to 0.3 eV. A system of electromagnetic lenses focuses the electron beam on the surface of the specimen forming a sub-nanometrical probe of 0.5-1 nm diamter. The scanning of the electron beam at the surface of the sample is guaranteed by two coils sitting before the objective lens. Oppositely to conventional TEM microscopes, there is no additional optics after the objective lens. A series of detectors allows to collect at different angles the electrons elastically or inelastically scattered.

In STEM microscopes, images are formed sequentially by scanning with the electron probe the surface of the sample and by a synchronised collection of the signal which is generated by a nanometric volume defined by the lateral size of the probe and the sample thickness. Images can be registered in different modes using detectors positioned at different angles with respect to the optic axis. Bright field images are obtained by collecting part of the transmitted beam at low angle close to the microscope axis. Similarly to standard transmission electron microscopy, the signal results

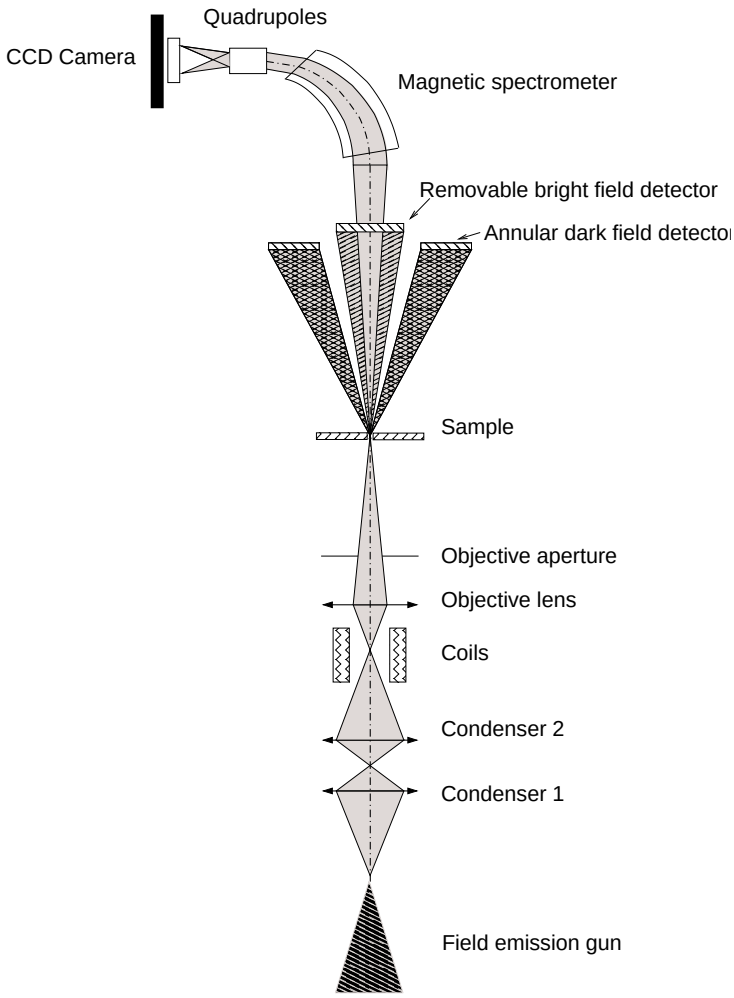

Figure 2.2: *Schematic representation of a scanning transmission electron microscope.*

from a coherent process. High angle annular dark field images (HAADF) are on the contrary formed by collecting electrons scattered at high angle. This is possible using a detector centered on the optic axis of the microscope and having a hole at its center. The HAADF intensity depends from composition, thickness and density of the sample and can be estimated according to the formula:

$$I_{el} = I_0 \rho t \sigma_{el} \tag{2.1}$$

where I_0 is the incident beam intensity, ρ is the atom density in the analysed volume and t is the sample thickness and σ_{el} is the elastic cross section. This last term has a dependence on the atomic number of the target atom given by $Z^{4/3}$. Thicker or densier zones of the sample appear on the images as brighter regions on a darker background. HAADF images deliver a direct information on the morphology of the nano-object analysed and can be used for mesuring the quantity of matter at different regions of the specimen.

2.2.1 Experimental set-up

In this thesis work, experiments have been performed in a VG-HB501 STEM equipped with a tungsten cold field-emission gun. The vacuum in the vicinity of the sample was around $5 \cdot 10^{-8}$ torr and has been obtained with an oil-free pumping system. High mechanical sample stability was obtained by a top-entry sample holder system, we will see in Chap. 5 how this stability was of fondamental importance for experiments of local electron irradiation on nanoobjects. The beam convergence half-angle was set to about 7.5 mrad and the used pole piece has a spherical aberration of around 3.1 mm. For voltage energy of 100 keV, it corresponds to the formation of an electron probe of around 0.8 nm in diameter at the sample surface. Electron probe sizes were slightly degraded when lower voltages such as 60 or 80 keV were used. Bright field (BF) images have been obtained with a collection semi-angle of 1.25 mrad and dark field (DF) images have been obtained with collection angle between 25 and 200 mrad. In irradiation experiments, for BF/DF imaging the acquisition time was limited to 1-2 seconds and when needed beam blanking was used before the sample in order to limit the electron irradiation required to image the nanotube. Electron beam currents have been calibrated by a direct measurement of the current inside the drift tube of an EELS spectrometer

using a Keithley pico-amperometer.

2.3 The many body problem

Simulation of properties of real molecules and solids can give important informations both qualitative and quantitative for the designing and interpreting experiments in chemistry and solid state physics. The high level of accuracy obtained in the last years by experimental techniques have promoted a continous improvement of simulation methods.

Classical representations using parametrized models such as interatomic potential or bond-change models have been in the past a valuable support to the understanding of a large class of systems and it still continues to be used in wide number of experiments. However the use of quantum mechanical methods of simulation is becoming of more and more fundamental importance with the improvement of the experimental techniques and the always more reduced scales accessible to experiments.

The Schrödinger equation can be easily constructed for an ensemble of many particules however its direct analytical solution becomes unfeasible beyond the simpliest systems. Several solutions have been proposed over the past years, based on different sets of approximations. The density functional formalism has been demonstrated to be an accurate method for solving the ground state of a many-electron problem. Reconducting the many particle problem to a single particle one, DFT might be seen as a pragmatic approach, allowing to explore larger problems than those solvable with the all-electron Schrödinger equation.

In this part of the chapter we will illustrate the fundamental hypothesis standing behond the density functional theory. In section 2.6 we will illustrate the tight binding approximation of standard density functional theory and how this method can be employed to explore larger systems then those accessible by standard DFT.

2.3.1 The many particle Schrödinger equation

Considering a problem involving N_e electron and N_n nuclei, the total wave function of the system depends both on the electron spatial and spin coordinates $\mathbf{r}_i$ and s_i and on the nuclei spatial coordinates $\mathbf{R}_\alpha$:

$$\Psi \equiv \Psi(\mathbf{r}_1, s_1, \ldots, \mathbf{r}_i, s_i, \ldots, \mathbf{r}_{N_e}, s_{N_e}; \mathbf{R}_1 \ldots \mathbf{R}_\alpha \ldots \mathbf{R}_{N_n}) \tag{2.2}$$

The Schrödinger equation for this ensemble of nuclei and electrons can be expressed by

$$\hat{H}\Psi(\mathbf{r},\mathbf{R}) = E\Psi(\mathbf{r},\mathbf{R}) \tag{2.3}$$

E is the many-body energy of the system and $\hat{H}$ is the many-body non relativistic hamiltonian which can written in the form:

$$\hat{H} = T_n + T_e + V_{e-e} + V_{\text{ion}} + V_{n-n} \tag{2.4}$$

The terms T_n and T_e are respectively the nuclei and electrons kinetic energies, V_{e-e} the electron-electron interactions, V_{ion} the electron-nuclear interactions and V_{n-n} the nuclear-nuclear interaction. Ignoring sping-orbit coupling interaction and spin spin interaction the term of the hamiltonian can be explicity written. Noting M_α and Z_α the mass and charge of the atom $\mathbf{R}_\alpha$ we can explicit write the different terms of equation 2.4 in atomic coordinates:

$$\begin{aligned}
T_n &= -\frac{1}{2}\sum_{\alpha=1}^{N_n}\frac{1}{M_\alpha}\nabla_\alpha^2 \\
T_e &= -\frac{1}{2}\sum_{i=1}^{N_e}\nabla_i^2 \\
V_{e-e} &= +\frac{1}{2}\sum_{\substack{i,j=1\\ i\neq j}}^{N_e}\frac{1}{|\mathbf{r}_i-\mathbf{r}_j|} \\
V_{\text{ion}} &= -\sum_{i,\alpha=1}^{N_e,N_n}\frac{Z_\alpha}{|\mathbf{r}_i-\mathbf{R}_\alpha|} \\
V_{n-n} &= +\frac{1}{2}\sum_{\substack{\alpha,\beta=1\\ \alpha\neq\beta}}^{N_n}\frac{Z_\alpha Z_\beta}{|\mathbf{R}_\alpha-\mathbf{R}_\beta|}
\end{aligned} \tag{2.5}$$

The kinetic energy terms are summed over all the N_n atoms and N_e electrons whereas the term $1/2$ on the electron-electron and nuclear-nuclear interactions remove the double counting in the sum.

2.3.2 Born-Oppenheimer approximation

The large mass difference between electrons and nuclei makes electron response practically instantaneous to nuclear motion. The many-body wave function can subsequently be separated into two parts depending only from the electronic and nuclear coordinates:

$$\Psi(\mathbf{r};\mathbf{R}) = \psi_{\mathbf{R}}(\mathbf{r})\psi(\mathbf{R}) \tag{2.6}$$

where $\psi_{\mathbf{R}}(\mathbf{r})$ is the electron wave function which corresponds to a certain distribution of the nuclei. The quantum mechanical problem of solving the ground state wave function of a solid can be reduced to the solution of the Schrödinger equation of the electrons in a given frozen configuration of the nuclei. This approximation is called the Born-Oppenheimer approximation.

2.4 Density functional theory

The density functional theory, originally developped in the works of Hohenberg and Kohn [43] and Kohn and Sham [44], provides some simple method for describing exchange and correlation effects in an electron gas. The work of Hohenberg and Kohn [43] has proved that the total energy of the system, including exchange and correlation interactions, is a unique functional of the electron density. The successive work of Kohn and Sham [44] has demonstrated the possibility to replace the many particle problem by an equivalent set of one-electron equations. The minimum of the electron density functional corresponds to the ground state energy of the system and the corresponding density is the single particle ground state density.

Considering a set of doubly occupied electronic states $\{\psi_i\}$ (we note occ the total number of these states) the Kohn-Sham function for the total energy is written in the following form:

$$\begin{aligned} E[\{\psi_i\}] = \sum_{i}^{\text{occ}} \langle\psi_i| -\frac{\triangle}{2} + V_{\text{ion}} + V_H[n(\mathbf{r})]|\psi_i\rangle \\ + E_{\text{XC}}[n(\mathbf{r})] + E_{\text{ion}}(\{\mathbf{R}_\alpha\}) \end{aligned} \tag{2.7}$$

where $E_{\text{ion}}(\{\mathbf{R}_\alpha\})$ is the Coulomb energy of the nuclear-nuclear inter-

actions of the nuclei distribution $\{\mathbf{R}\}$, V_{ion} is the nuclei electron potential, E_{XC} is the exchange correlation functional and the term V_H is the electron-electron Hartree potential given by

$$V_H[n(\mathbf{r})] = \frac{1}{2}\int \frac{n(\mathbf{r}')}{|\mathbf{r}-\mathbf{r}'|}\mathbf{d}^3\mathbf{r}' \tag{2.8}$$

the electronic density $n(\mathbf{r})$ is derived from the set of single electron wave functions ψ_i:

$$n(\mathbf{r}) = \sum_{i}^{occ} |\psi_i(\mathbf{r})|^2 \tag{2.9}$$

2.4.1 Kohn-sham equations

The minimum of the Kohn-Sham energy functional (Eq. 2.7) represents the ground state energy of a system of electrons in the potential generated by a $\{\mathbf{R}_\alpha\}$ nuclei distribution. In the density functional formalist the solution of the many body Schrödinger equation corresponds to find the set of wave functions $\{\psi_i\}$ which minimises the total energy functional. The work of Kohn and Sham [44] has demonstrated that the problem correponds to solve the set of single particle equations given by:

$$\left[-\frac{1}{2}\nabla^2 + V_{\text{ion}}(\mathbf{r}) + V_H(\mathbf{r}) + V_{\text{XC}}(\mathbf{r})\right]\psi_i(\mathbf{r}) = \epsilon_i\psi_i(\mathbf{r}) \tag{2.10}$$

where ϵ_i represent the Kohn-Sham eigenvalues correspondent to the ψ_i wave function. V_{XC} is the exchange correlation potential formally defined deriving the exchange correlation functional of equation 2.7 in respect to the electron density:

$$V_{\text{XC}} = \frac{\delta E_{\text{XC}}[n(\mathbf{r})]}{\delta n(\mathbf{r})} \tag{2.11}$$

The Kohn-Sham equations translate the many electron mutual interacting problem onto the problem of a single electron moving into an effective potential generated by the other electrons. Knowing the exchange correlation functional E_{XC} one can solve self-consistently the set of equations 2.10. Using the expression 2.9 the electron charge density $n(\mathbf{r})$ is obtained from the occupied wave functions ψ_i and from it we can derive the electron potential to introduce in the Kohn-Sham equations 2.7. Using a variational principle, this routine is repeated iteratively up to obtain a set of

wave functions $\{\psi_i\}$ which represent a stationary solution of the Kohn-Sham equations. This set corresponds to a minimum of the total energy functional $E[\{\psi_i\}]$ which is the ground state energy of the system.

2.4.2 Local density approximation

Whereas the DFT theory gives an exact solution of the many body Schrödinger equation, the exact general form of the exchange correlation functional is still unkown. However the explicit form has been derived for homogeneous electron gas at high and low density. Under the hypothesis that the exchange-correlation contribution to the total energy varies only gradually at short range, to a first approximation it can be assumed that it is constant and it has the same value as for a uniform electron gas of same density. In the local-density approximation (LDA) the total exchange-correlation energy can then be written in the form of the integral

$$E_{\mathrm{XC}} = \int \varepsilon_{\mathrm{XC}}[n(\mathbf{r})]n(\mathbf{r})d^3r \tag{2.12}$$

where $\varepsilon_{\mathrm{XC}}[n(\mathbf{r})]$ is the exchange and correlation energy per electron in a uniform electron gas density $n(\mathbf{r})$. The main drawback of LDA is the underestimation of the forbidden electronic band gap of semiconductor crystals. Alternative functional incorporating longer range effects, such as GGA (Generalized gradient approximations), are available but are not used here.

2.5 DFT as implemented in the AIMPRO code

During this thesis work, DFT calculations have been performed using the `AIMPRO` code (acronim for *Ab Initio Modelling PROgram*). The code have been continously developed during the last twenty years by groups at Exeter, Newcastle and Luleå universities. `AIMPRO` allows to calculate systems up to one thousand of atoms with a reasonable computational effort[1] and to derive a large number of physical properties as Mulliken charges, vibrational spectra, EELS spectra etc.

[1] As example the electronic ground state for a defective planar graphite sheet containing 198 atoms has been computed in 53 minutes using 8 PIV CPUs

In this section we will present the basis of the DFT implementation into the AIMPRO code. More details about the computational methods are given in Refs. [45, 46, 47]. Further informations can also be found in the AIMPRO web page (http://aimpro.ncl.ac.uk/).

2.5.1 Basis functions

AIMPRO uses Cartesian Gaussian orbitals of the form:

$$\phi_i(\mathbf{r}-\mathbf{R_i}) = (x-R_{ix})^{l_1}(y-R_{iy})^{l_2}(z-R_{iz})^{l_3}e^{-\alpha(\mathbf{r}-\mathbf{R_i})^2} \tag{2.13}$$

These orbitals are then centered on the nuclei positions $\mathbf{R_i}$. In the case all the l_i coefficients are equal to 0 the orbitals are simply spherical symmetric gaussian functions, also called s-gaussian orbitals. In the case that only one $l_i = 1$, the others beeing 0, the functions are p-Gaussians orbitals while if the sum of the l_i is 2, the set of six orbitals generate five d-orbitals and one s orbital. The advantage in using gaussian orbitals is that, for all the integrals, it is possible to provide analytical solutions. For supercell calculations, Bloch basis functions are constructed from this gaussian function set.

2.5.2 Pseudopotentials

Explicitely incorporating in the calculations core states means to use a big basis function. Furthermore, the orthogonality to core electrons wavefunctions impose to the valence electron wavefunctions strong oscillations close to the nucleus. However the chemical properties of an atom are almost entirely dependent upon the atom's valence electrons and their interaction with neighbouring atoms while the core states are relatively independent of the atom's environment. Core electrons can then be neglected from calculations by replacing the atomic potential by a pseudopotential V^{ps} where the core electrons create a screening effective potential which acts upon the valence electrons. An imposed constraint is that, outside of a chosen cut-off radius r_c, the pseudo valence wavefunctions have to match exactly that of their real all electron counterpart.

However, such a pseudopotential will contain terms arising from the interaction of core and valence electrons and hence will not be transferable to different chemical environments. A transferable ionic potential

$V_{\text{ion}}^{\text{ps}}$ is constructed by substracting the potential (coulombic and exchange-correlation) arising from the valence states to the pseudopotential V^{ps}:

$$V_{\text{ion}}^{\text{ps}} = V^{\text{ps}}(\mathbf{r}) - \int \frac{n^{\text{ps}}(\mathbf{r}')}{|\mathbf{r}-\mathbf{r}'|}\mathbf{d}^3\mathbf{r}' - E_{\text{XC}}[n^{\text{ps}}(\mathbf{r})] \tag{2.14}$$

where n^{ps} is the charge density arising from the valence electrons. When employing the pseudopotential formalism, a number of approximations are made. First a one-electron picture is used to divide the electrons into core and valence states. Secondly, the frozen core approximation considers that the core states are independent of the atoms environment. Finally, the small core approximation assumes that the valence and core states do not overlap signicantly and hence we consider the total exchange correlation energy E_{XC} as a sum of two terms depending separately from the core electron density and the valence electron density. In cases where the overlap is significant, it may be necessary to apply non-linear core corrections to the pseudopotential

The calculations presented in the next chapters employ the Hartwigsen Goedecker Hutter (HGH) pseudopotentials [48]. These pseudopotentials are norm-conserving, *i.e.* their integrated sum matches that of the all electron function. HGH pseudopotentials are explicitly designed to be optimised for Gaussian basis sets.

2.5.3 B and N pseudopotentials

Boron and nitrogen pseudo-potentials are generated using the Hartwingster Goedecker Hutter scheme. Atom centred Gaussians (5 per atom) are used for the wavefunction basis, each multiplied by spherical harmonics up to a maximum angular momentum of *l*=1. For the Gaussian with the second smallest exponent the maximum is *l*=2. The energy cut-off used in the bloch transformation is 150 Hartrees.

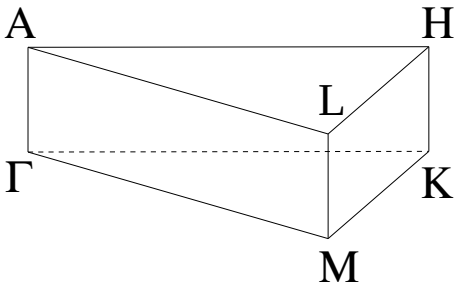

Figure 2.3: *Schematic representation of the reduced Brillouin zone for an h-BN cristal.*

The reduced Brillouin zone for an h-BN cristall is represented in figure 2.3 where we have indicated the high symmetry points. In figure 2.4 we have represented the band structure diagram of h-BN obtained using the de-

scribed pseudopotentials and basis. As previously mentioned the LDA approximation gives an underestimation of the electronic band-gap. We obtain a band-gap of 4.4 eV whereas it has been experimentally estimated in 5.8 eV [34]. Higher level theoretical calculations find a band gap of 6.2 eV [32, 33].

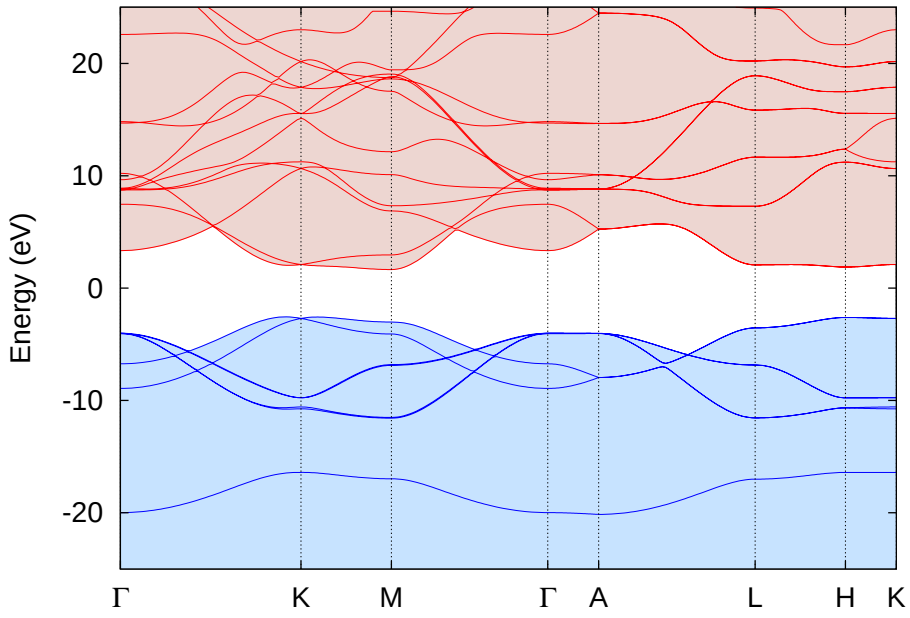

Figure 2.4: *Bandstructure of the hexagonal phase of boron nitride obtained by DFT-LDA using the AIMPRO code with the pseudopotentials and energy cut-offs described in Sec. 2.5.3.*

2.6 Density functional tight binding

Standard DFT computation methods give quite satisfactory results for solid state simulations at a relatively low computational cost. Using limited computer resources this technique allows to easily calculate systems containing up to hundred atoms. However, the increasing interest in solid state physics on defects and nanostructures induces to consider structures containing thousand of atoms and to investigate large number of possible different morphological configurations. In this context, the use of DFT becomes rapidly too time expensive. From an other side, standard tight-binding (TB) techniques represent a well experimented method able to

calculate atomic and electronic structures, energies and forces for larger molecular and condensed systems. Standard tight-binding consists in expanding the eigenstates of the system in orthogonalised atom-like orbitals and to consider a parametrised Hamiltonian whose elements are fitted on the band structure of reference systems [49]. However the transferability of the method could fail when describing bonding situation far from the equilibrium structures for which parameters have been derived.

A good compromise between DFT and standard TB is represented by the density functional tight binding method (DFTB). This technique can be seen as an hybrid between DFT and TB and it gives excellent results in simulating complex nanoscale materials at a limited computational cost. Within the last ten years DFTB has been applied in the study of a large variety of problems in chemistry, physics, materials science and biochemistry given results comparable with other higher end techniques [50]. Excellent results have been obtained in the simulation of a large variety of physical properties: atomic and electronic structures, vibrational spectra, optical response, magnetisation. In the following we will give a rapid overview on the basis of the DFTB method in its basic non charge self-consistent approach. Successive theoretical extentions will be not considered. Indeed the original version of the DFTB method has been demonstrated to be enough accurate for the purpose of this study

2.6.1 Non SCC-DFTB

Semiempiral tight-binding models have been widely used in the simulation of molecular and solid systems. Whereas these methods have been often treated as simply fitting and interpolation schemes, their validity can be justified in relation with more fundamental theories [51]. Density functional tight binding is a scheme which can be derived from the standard Kohn-Sham theory. The Kohn-Sham function for the total energy written in Eq. 2.7 is minimised by a ground state density $n_0 = n_0(\mathbf{r})$. We consider a small norm conserving fluctuation $\delta n = \delta n(\mathbf{r})$ around this reference density and we note $\int d\mathrm{r}$ as $\int$. Wherever a second integration coordinate is required similarly the symbols n_0', $\delta n'$, $\int'$ are used. Equation 2.7 can then be rewritten as:

$$
\begin{aligned}
E[\{\psi_i\}] = \sum_i^{\text{occ}} \langle\psi_i| -\frac{\triangle}{2} + V_{\text{ion}} + \int' \frac{n_0'}{|\mathbf{r}-\mathbf{r}'|} + V_{\text{XC}}[n_0]|\psi_i\rangle \\
- \frac{1}{2}\int\int' \frac{n_0'(n_0+\delta n)}{|\mathbf{r}-\mathbf{r}'|} - \int V_{\text{XC}}[n_0](n_0+\delta n) \\
+ \frac{1}{2}\int\int' \frac{\delta n'(n_0+\delta n)}{|\mathbf{r}-\mathbf{r}'|} + E_{\text{XC}}[n_0+\delta n] + E_{\text{ion}}(\{\mathbf{R}_\alpha\})
\end{aligned}
\tag{2.15}
$$

The hamiltonian derived from the input density n_0 can be written in the form of the operator $\hat{H}_0$:

$$
\hat{H}_0 = -\frac{\triangle}{2} + V_0 = -\frac{\triangle}{2} + V_{\text{ion}} + \int' \frac{n_0'}{|\mathbf{r}-\mathbf{r}'|} + V_{\text{XC}}[n_0] \tag{2.16}
$$

We use a Taylor expansion at the first order for the E_{XC} term around the reference density n_0. Equation 2.15 can thus be written as:

$$
\begin{aligned}
E[\{\psi_i\}] = \sum_i^{\text{occ}} \langle\psi_i|\hat{H}_0|\psi_i\rangle - \frac{1}{2}\int\int' \frac{n_0' n_0}{|\mathbf{r}-\mathbf{r}'|} + E_{\text{XC}}[n_0] \\
- \int V_{XC}[n_0]n_0 + E_{\text{ion}}(\{\mathbf{R}_\alpha\}) \\
+ \frac{1}{2}\int\int' \left(\frac{1}{|\mathbf{r}-\mathbf{r}'|} + \left.\frac{\delta^2 E_{\text{XC}}}{\delta n \delta n'}\right|_{n_0} \right) \delta n \delta n' + \mathcal{O}(\delta n^3)
\end{aligned}
\tag{2.17}
$$

The first and second line give the zero-th order terms in δn of the expansion, the third line gives the second and third order terms. All first order contributions cancel. In the standard DFTB method terms of order higher than zero are normally neglected. The DFTB total energy depends then only on the input density n_0 and on the nuclei-nuclei repulsive potentials and can thus be expressed as a sum of one and two center potentials:

$$
E_0^{\text{TB}}[\{\psi_i\}] = \sum_i^{\text{occ}} \langle\psi_i|\hat{H}_0|\psi_i\rangle + E_{\text{2cent}} \tag{2.18}
$$

This expression for the total energy can further be simplified approximating the two center contributions by the sum of short-ranged repulsive pair potentials $v_{\text{rep}}^{\alpha\beta}$:

$$E_{2\text{cent}} \approx \frac{1}{2}\sum_{\alpha\neq\beta} v_{\text{rep}}^{\alpha\beta}(|\mathbf{R}_\alpha - \mathbf{R}_\beta|) = E_{\text{rep}}(\{\mathbf{R}_\alpha\}) \tag{2.19}$$

The solution of the Kohn-Sham equation is obtained expanding the single particle Kohn-Sham orbitals ψ_i of the global system in terms of atom-centered localised basis functions ϕ_μ:

$$\psi_i(r) = \sum_\mu C_{\mu i}\phi_\mu(\mathbf{r} - \mathbf{R}_\alpha) \tag{2.20}$$

The basis functions ϕ_μ are usually expressed as a linear combination of Slater type orbitals[2]:

$$\phi_\mu = \sum_{n,\zeta,l_\mu,m_\mu} a_{n,\zeta} r^{l_\nu+n} e^{-\zeta r} Y_{l_\mu m_\mu}\frac{\mathbf{r}}{r} \tag{2.21}$$

where l and m are respectively the angular momentum and magnetic quantum number associated with the orbital μ. Five different values of ζ and n=0,1,2,3 forms a sufficent accurate expansion for all elements up to the third row. This Slater type orbitals are determined by solving a modified Kohn-Sham equation for a free standing neutral pseudo-atom:

$$\left[-\frac{1}{2}\nabla^2 + V_{\text{ion}}(\mathbf{r}) + V_H(\mathbf{r}) + V_{\text{XC}}(\mathbf{r}) + \left(\frac{r}{r_0}\right)^N\right]\phi_\mu(\mathbf{r}) = \epsilon_\mu^{\text{psat}}\phi_\mu(\mathbf{r}) \tag{2.22}$$

The additional term $(r/r_0)^N$ has been introduced to improve the band structure calculations and, compared to the free standing atom, it compress the electron wave function close to the nucleus [52].

Applying the variational principle to the energy functional of Eq. 2.18 we obtain the Kohn-Sham equation of the system. According to the orbital expansion in a pseudoatomic basis (Eq. 2.21), the Kohn-Sham equation can be written as a set of algebrical secular equations:

$$\sum_\nu^M C_{\nu i}(H_{\mu\nu} - \varepsilon_i S_{\mu\nu}) = 0 \qquad \forall\mu, i \tag{2.23}$$

with

[2] Alternatively the basis functions ϕ_μ can be expressed as a linear combination of atom centered cartesian gaussian orbitals.

$$H_{\mu\nu} = \langle \phi_\mu | \hat{H}_0 | \phi_\nu \rangle$$
$$S_{\mu\nu} = \langle \phi_\mu | \phi_\nu \rangle \qquad \forall \mu \in \alpha \qquad \nu \in \beta \tag{2.24}$$

The dimension of the secular equation is much smaller than in most of the standard density functional methods and there is no need for self consistency looping. According to the expression of the hamiltonian $\hat{H}_0$ in a sum of a kinetic part and a one electron potential V_0^α centered on the atom α (Eq. 2.16), the matrix elements $H_{\mu\nu}$ are written as:

$$H_{\mu\nu} = \begin{cases} \varepsilon_\mu^{\text{neutal free atom}} & \text{for} \quad \alpha \neq \beta \quad \& \quad \mu = \nu \\ \{\psi_\mu^\alpha | \hat{T} + V_0^\alpha + V_0^\beta | \psi_\nu^\beta\} & \text{for} \quad \alpha \neq \beta \\ 0 & \text{for} \quad \alpha = \beta \quad \& \quad \mu \neq \nu \end{cases} \tag{2.25}$$

The diagonal elements of the matrix are the eigenvalues of the free atoms which garanties the correct limit for free standing atoms. The non diagonal elements of the hamiltonian and the overlap matrix can be tabulated as a function of the distance between the two centers. Equation 2.23 can thus be solved non self-consistently for any given configuration of atomic coordinates. Once the set of secular equations is solved the sum of the eigenvalues is added to the pair-potential repulsive energy E_{rep} to give the total energy for that particular arrangement of the frozen atoms. The repulsive pair energy term can be tabulated as a function of the distance between two nuclei:

$$E_{\text{rep}}(R) = \left\{ E_{\text{LDA}}^{\text{SCF}}(R) - \sum_i^{occ} \varepsilon_i(R) \right\} \Bigg|_{\text{reference structure}} \tag{2.26}$$

The first term of the right part of the equation is the total cohesive energy of a reference molecule derived from a self consistent DFT-LDA calculation and the second one the TB band structure energy obtained solving equation 2.23. A manual fitting process for the derivation of the $E_{\text{rep}}(R)$ typically proceeds by identifying a series of structures (crystals or small molecules) with examples of the chemical bonds which should be reproduced by the parameter set. The bond lengths are then systematically variated and the DFT total energy and DFTB bandstructure energy are calculated. This process requires a large amount of human intervention and pose a strong limit to the derivation of new parameters sets. However

first attempts to automatise this fitting procedure have been reported [53].

Interatomic forces used for structural optimisations and molecular dynamics simulations are derived from an explicit calculation of the gradient of the total energy of Eq. 2.18. Fig. 2.5 summarises the different steps of the DFTB calculation algorithm. Within the DFTB method all the DFT integrals and the repulsive interractions are calculated in advance limiting significantly the computation effort and speeding up drammatically the calculations. Thus, compared to standard DFT schemas, the tight binding approximation give access to much larger systems and longer MD simulations.

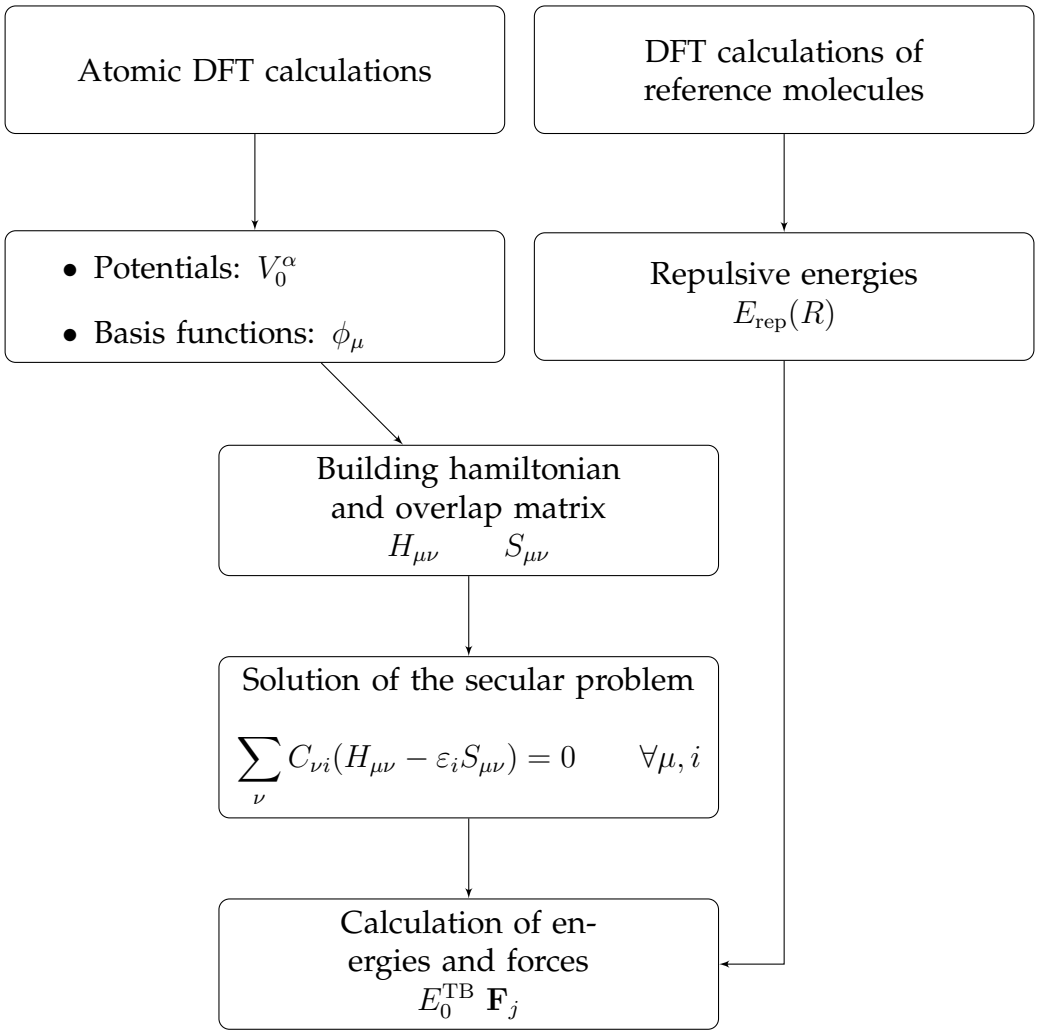

Figure 2.5: *Graphical representation of the algorithm of DFTB calculations*

The original DFTB schema here presented has been extended in order to improve total energies, forces and transferability. For particular systems the previous neglected second order charge fluctuations (Eq. 2.17) might becomes too large to be transferable and simply tabulated within the repulsive potential. The DFTB self consistent charge extension (SCC-DFTB) take explicitely into account this second order term [54]. The charge transfer is thus approximated by atom centered charge fluctuations δn and treated self consistently. Recently Spin polarisation effects have also been included in the DFTB schema showing the possibility to derive magnetic properties for large systems [55].

2.6.2 Codes and parameters

In the course of this thesis DFTB techniques have been employed when standard DFT techniques were too time consuming. In particular DFTB calculations have been used for relaxing large defective structures in BN and carbon nanotubes (Secs. 3.6,5.1.1). In combination with NEB techniques we have also obtained by DFTB vacancy migration paths in h-BN (Sec. 3.4.2). Finally DFTB based molecular dynamics simulations have been conducted in the study of electron irradiation induced atom ejection from BN and carbon nanotubes (Sec. 4.2).

DFTB calculations have been performed using mainly the `deMon2k` code [56]. although the new `DFTB+` code [57] has also been used on few occasions. Phonon frequencies analysis in Sec. 3.4 have been calculated with the older `dylax` code. For carbon systems we have used the set of parameters originally derived by Porezag *et al.* [58]. It has been shown that this set of parameters is highly transferable and have been used successfully in the study of molecular systems, graphite, diamond and carbon nanotubes. Matrix elements for B, N, BN, and NH have been derived by Widany *et al.* [59]. In the same work the authors show how this set of parameters gives exellent results for a large number of molecular and crystal structures. This set has been successively used in the study of BN fullerenes [60, 61] and BN nanotubes [62]. In Fig. 2.6 the electronic band structure diagram of h-BN calculated with this parameter set is compared with a pseudopotential DFT-LDA calculation. The DFTB approximation is qualitatively correct for bands in the valence region but it fails in the conduction band due to the limited basis on which orbitals are expanded and the non consideration of three centers integrals. However the inaccuracy in the determination of unoccupied bands does not affect the result

obtained for structural optimisations.

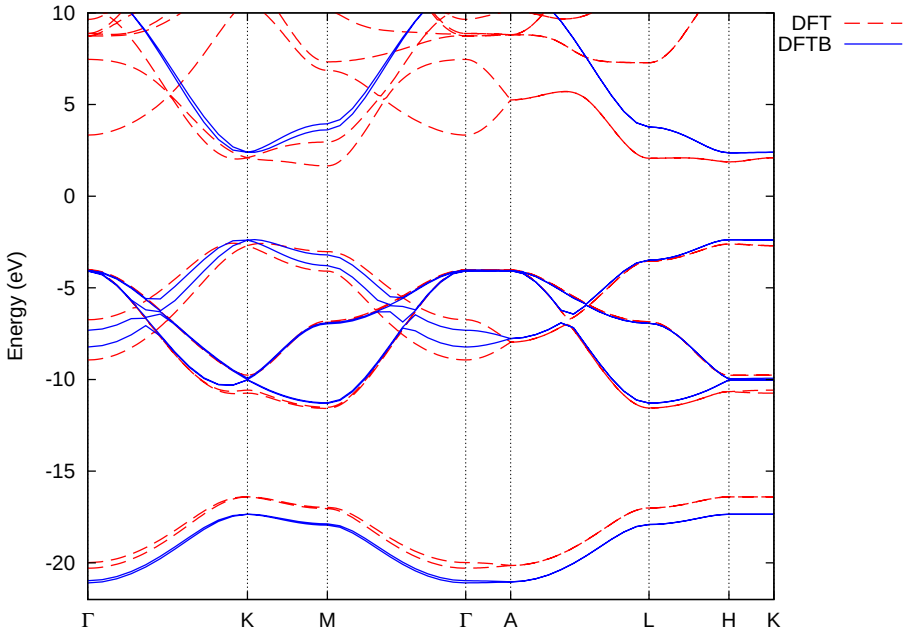

Figure 2.6: *Comparison between the bands structure diagram of h-BN obtained by DFTB (full line) and standard DFT-LDA (dashed line).*

2.7 Nudged elastic band method

The study of transition processes such as the dynamics of chemical reaction or the diffusion mechanism in a solid can be conducted in a direct way using standard molecular dynamics or Monte Carlo approaches. In recent years the use of *ab initio* methods has allowed to obtain a more precise derivation of thermodynamical parameters such reaction rates or diffusion coefficients [63]. However, the time scale at which chemical reaction occurs, makes the use of molecular dynamics simulations extremely time consuming and only conceivable for small molecular systems.

A different approach consists in exploring the configuration space assuming some supplementary hypothesis on the reaction path and obtaining activation barriers from static calculation of energy minimisation under certain structural bounds. Within the different paths connecting the initial and final reaction states, the minimum energy path (MEP) has the greatest statistical weight. Along the MEP, the forces acting on the atoms

point only along the path. The maximum along the path is a saddle point of the potential energy surface which corresponds to the reaction transition state. The total energy associated with this state is the reaction activation energy from which further thermodynamical quantitites can be derived. Within the different methods developed for deriving the MEP the nudged elastic band method (NEB) has been widely used in a broad range of problems [64, 65, 66].

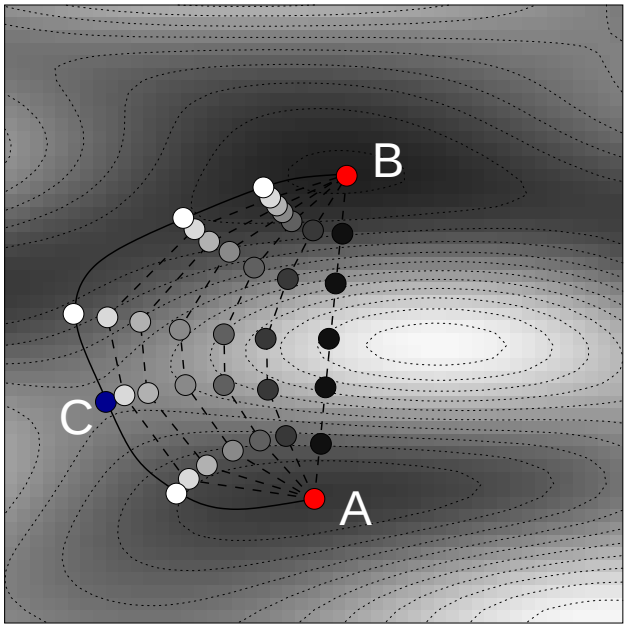

Figure 2.7: *Schematic representation of the NEB techniques in a bidimensional configuration space. Intial and final states are indicated respectively with the letters A and B. The reaction transition state is indicated by the letter C.*

Figure 2.7 gives a schematic representation of how the NEB proceeds in a bidimentional configuration space. The initial and final reaction states are indicated respectively by the letters A and B, the transition state is indicated as C. The states A,B and C are connected by the MEP represented in the figure by a solid line. A first chain of images $\{R_i\}$, represented in Fig. 2.7 by the darker serie of dots, is build by linear interpolation of the initial and final configurations. Successively all the intermediate images are moved simultaneously using a molecular dynamics algorithm where on each image R_i acts a Newton force F_i expressed by:

$$\vec{F}_i = -\vec{\nabla} V(R_i)|_{\perp} + \vec{F}_i^s|_{||} \tag{2.27}$$

$\vec{\nabla}V(R_i)|_\perp$ is the component of the true force orthogonal to the path and $\vec{F_i^s}|_{||}$ is the component parallel to the path of an additional spring force connecting image R_i with the two contigous images R_{i-1} and R_{i+1}. In Fig. 2.7 we have represented the evolution of the initial chain of states on the potential surface: lighter chains of states represent successive molecular dynamics steps. After several iterations the intermediate states of the chain tend to be aligned on the MEP. Using a limited number of images, it is possible that any image would coincide with the saddle point of the reaction. A post treatement using interpolation techniques is then necessary for deriving the correct energy associated with the transition state. The original scheme described here has been improved using a non homogeneus spring force along the reaction path which leads during the MD simulation to a progressive increasing of the image density around the transition state [65, 66].

Compared to other techniques, NEB only requires structural information concerning the initial and final states, with optionally few other intermediate configurations. It is thus a suitable technique for exploring in an efficient way a large region of the configuration space and for deriving even complicated minimum energy paths. No *a priori* assumption for the migration path is required, in particular there is no need to enforce symmetry at the saddle point. Due to the slow convergence of the method, the use of standard density functional based techniques is too time consuming. The use of empirical techniques or force fields or classical potentials is not suitable due to their inability to describe phenomena far from equilibrium configurations for which parameters have been derived. A good compromise between *ab initio* density functional theory and classical empirical tight-binding methods can be obtained using density functional tight binding theory (DFTB) which reduces the computational time by some orders of magnitude while remaining a quantum method. It has already been shown that the combination of DFTB and NEB gives results comparable to other higher-end techniques [67]. A NEB routine has been recently implemented by R. Barthel into the `deMon2k` code which has been used in this thesis work.

CHAPTER 3

DEFECTS IN h-BN AND BN NANOTUBES

IT IS WELL established that carbon nanotubes synthesis processes make the formation of native defects very probable. Defects can also be introduced *post synthesis*, willingly or unintentionally, through chemical or physical post-treatments used for purification or functionalisation of the tubes. Furthermore, investigation methods that use energetic particles are not completely "non destructive techniques" and they can induce important morphological modifications. As well as carbon nanotubes, we expect that BN-nanotubes are not synthetised defect free and that defects can be easily introduced in successive handlings of the tubes. Previous theoretical studies have suggested that single vacancies can exist in graphitic BN sheets [68], and similar defects have also been proposed in BN nanotubes [35, 36, 69]. Experimentally, electron paramagnetic resonance (EPR) has detected paramagnetic centers on hexagonal BN [70, 71] and electron irradiated hexagonal BN [72] and those results have been interpreted with the presence of carbon substitutional or nitrogen vacancies. More recently similar effects have been obtained in multiwalled BN nanotubes [73, 74].

However, numbers of questions remain still open for defects on h-BN and BN nanostructures, to some of which we will give an answer during this chapter. In particular, we will show through TEM experiments the possibility to direct image vacancies in single walled BN nanotubes. On the basis of a systematical analysis of structure and energetics of point defects in BN SWNTs, we will demonstrate that, under electron irradiation, primarily divacancies are formed. HREM images show also the appearence of more extended defective structures, that will be explained as dislocation lines in the hexagonal lattice of the tubes. The route for going from simple point defects to more extended dislocation lines will be discussed into details. In particular after having derived migration paths using a DFTB-NEB approach, we will discuss the thermal stability of point defects in h-BN and their impossibility at room temperature to migrate

and nucleate into larger defective structures. An alternative route, which will be discussed, is the existence of preferential emission sites once primary vacancies are present in the sample. For concluding the chapter we will show how all possible defects produced by irradiation have a similar electronic structure which corresponds to that one of BN divacancies.

3.1 Defects in h-BN and BN nanotubes: structure and energetics

3.1.1 Computational method

For h-BN defective structures we have considered a 7×7 supercell containing 98 atoms. Different sizes of the elementary cell were tested in order to minimize the interaction energy between defective structure in adjacent cells. Since we are only interested in defective structures in mono layers, the calculations have a single plane in the elementary cell and the c parameter of the lattice is large enough (~ 12 Å) to avoid interlayer interactions. Considering the large size of the unitary cell, just the Γ point has been used in the self-consistency cycles. For BN nanotubes we have considered a tetragonal lattice and a $\times 4$-supercell along the tube axis. The cell parameter orthogonal to the tube axis has been chosed in order to have a minimum distance of 15 Å between tube walls in adjacent cells.

The formation energies of the defective systems are calculated as a function of the chemical potential of the boron and nitrogen species, the electronic chemical potential and the total charge q of the system:

$$E_f\left(N_i^q\right) = E_t\left(N_i^q\right) - n_B\mu_B - n_N\mu_N + q(\mu_e + \varepsilon_e) \tag{3.1}$$

where E_t is the total energy of the defective system, n_B (n_N) and μ_B (μ_N) are respectively the total number of boron (nitrogen) atoms and the chemical potential. The electronic chemical potential μ_e is measured with respect to the top of the valence band (ε_e). As reference for the nitrogen we have taken an N_2 molecule, for the boron a B_{12} cluster. In this study we have considered only neutrally charged defects. For a detailed discussion on the formation energy of charged defects on BN nanotubes as function of the electron chemical potential see Piquini *et al.* [36].

3.1.2 Monovacancies

In a single walled BN nanotube, single vacancy formation energies are a function of nanotube diameter. The formation energy for a neutral single boron vacancy increases from $E_{V_B} = 8.20$ eV in a (8,0) nanotube (diameter 1.25 nm) to 8.82 eV for a (14,0) tube (diameter 2.22 nm), to 11.22 eV for planar *h*-BN. The equivalent figures for the nitrogen vacancy are E_{V_N} = 7.02 eV [(8,0) tube], 7.24 eV [(14,0) tube] and 8.91 eV (*h*-BN). There is a qualitative structural difference between the monovacancy in a *h*-BN sheet and in a nanotube. In the planar structure (Fig. 3.1) the equilibrium geometry conserves three-fold D_{3h} symmetry around the missing atom for both boron and nitrogen single vacancies. The relaxed structures exhibit a small relaxation of the three neighbouring atoms: 0.10 Å inward for the B atoms around the nitrogen vacancy (V_N) and 0.09 Å outward for the N atoms around the boron vacancy (V_N) with respect to their unrelaxed positions.

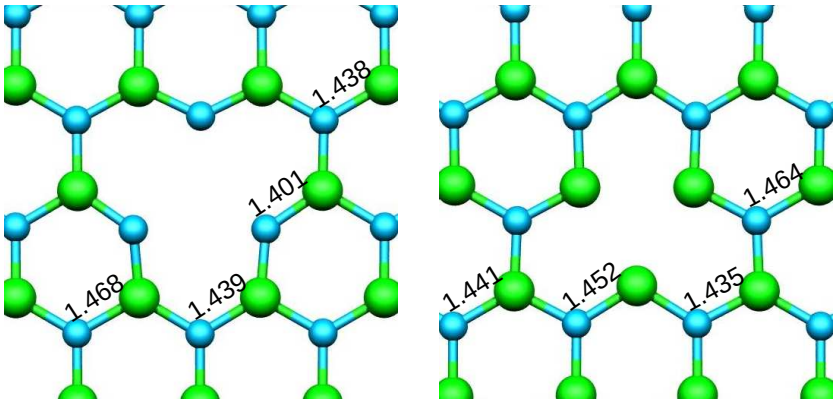

Figure 3.1: *Relaxed structure of a boron (left pannel) and nitrogen (right pannel) single vacancies in a h-BN sheet. Significant bond lenghts are reported in Angstrom.*

In the case of a nanotube (Fig. 3.2), the curvature induces sufficient lattice deformation to permit local bond reconstruction between two atoms neighbouring the vacancy with a preferential orientation of this reconstructed bond orthogonal to the tube axis. This behaviour explains the diameter dependence of the vacancy formation energies. Vacancy formation energies increases monotonically with the diameter of the tubes: bond reconstruction into larger diameter tubes induces a larger steric frustration. The *h*-BN case corresponds to the limit of an infinit diameter tube where bond reconstruction doesn't occur. In table 3.1 we report the formation energies of boron and nitrogen vacancies for a set of armchair and zigzag BN

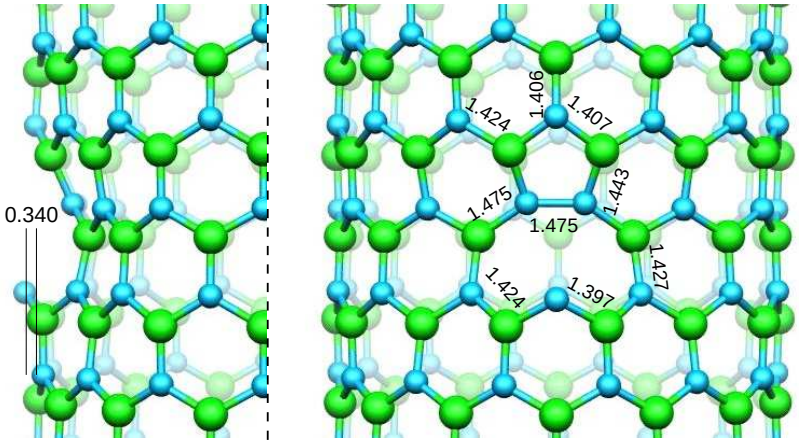

Figure 3.2: *Relaxed structure of a (14,0) BN nanotube with a nitrogen vacancy (left pannel: partial side view, right pannel front view). Bond lenghts, reported in figure, are expressed in Angstrom.*

nanotubes. For equivalent tube diameters energy formations are higher in armchair compared to zigzag tubes. This effect occurs becouse in zigzag tubes the recostructed bond lies orthogonally to the tube axis whereas in armchair tubes it forms an angle of 30° in respect to the tube axis.

3.1.3 Vacancy pairs

A more complete picture of vacancies in h-BN and BN nanotubes emerges once we consider vacancy pairs. The interaction energy between two vacancies depends on their separation, and different vacancy combinations are possible. Figure 3.3 shows relaxed structures for different types of divacancies in an h-BN plane obtained varying their mutual distance. Due to the B-N alternance, vacancies in next neighbouring sites are boron-nitrogen vacancy pairs (V_{BN}^{1st}). B-N vacancy pairs are also vacancies in third neighbour sites (V_{BN}^{3rd}) whereas vacancies in second or fourth neighboring sites form boron-boron (V_{BB}^{2nd} and V_{BB}^{4th}) or nitrogen-nitrogen vacancy complexes (V_{NN}^{2nd} and V_{NN}^{4th}).

Formation energies (E_f) and binding energies[1] (E_b) for the different va-

[1] We define the binding energy E_b between two vacancies as:

$$E_b(V_{1-2}) = E_f(V_1) + E_f(V_2) - E_f(V_{1-2})$$

where $E_f(V_1)$ and $E_f(V_2)$ are respectively the formation energies of the separeted single vacancies V_1 and V_2 and $E_f(V_{1-2})$ is the formation energy of the final configuration.

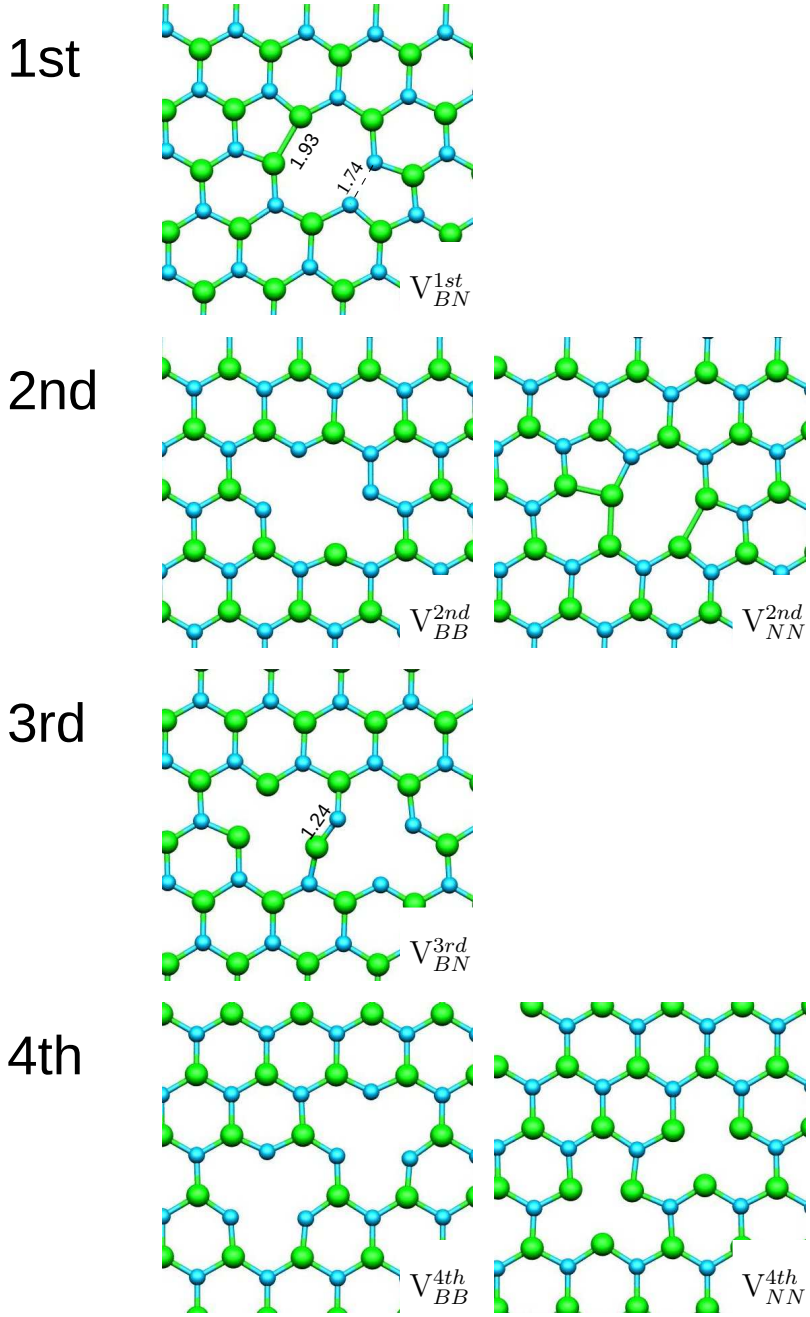

Figure 3.3: *Relaxed structure of different vacancy pairs in h-BN*

Nanotubes			
Chirality	Diameter (Å)	$E_f(V_B)$ (eV)	$E_f(V_N)$ (eV)
armchair tubes			
(4,4)	5.43	8.06	7.19
(6,6)	8.13	8.55	7.51
(8,8)	11.07	8.92	7.69
(10,10)	13.56	9.08	7.88
(12,12)	16.54	9.42	7.93
(16,16)	21.69	10.03	
zigzag tubes			
(8,0)	12.50	8.20	7.02
(14,0)	22.20	9.55	7.24
h-BN	∞	11.22	8.91

Table 3.1: *Vacancy formation energies in BN nanotubes as a function of the tube chirality*

cancy pairs in a plane considered are reported in table 3.2. Among them we found the most stable to be the first neighbour V_{BN}^{1st} complexe. In a h-BN sheet V_B and V_N have a combined formation energy of around 20 eV, but when on neighbouring sites this drops to 9.75 eV, *i.e.* they have a binding energy of around 10 eV. This shows that once a vacancy forms, the formation energy for a subsequent neighbouring vacancy is close to zero, thus the probability of forming a second neighbouring vacancy is higher than at any other site. A similar behaviour is found for BN nanotubes. In a (8,0) BN nanotube for example the formation energy of two separeted V_B and V_N is about 17 eV which becomes 9.2 eV when in neighboring sites. This strong driving force suggests that vacancies in layered BN systems will tend to appear as boron-nitrogen pairs. These first neighboring vacancy pairs induce the appearence of two pentagonal rings in the hexagonal lattice of the system related with the reconstruction of two weak homonuclear B-B and N-N bonds of a respective lenght of 1.93 and 1.74 Å (see V_{BN}^{1st} in Fig. 3.3). The boron-nitrogen alternance, chemically more favourable, could be conserved with a different bond reconstruction schema on which four member rings would appear. However it has already be shown that in BN systems the chemical frustration due to homonuclear bonds is more energetically favorable than the steric frustration introduced by lattice configurations that conserve the alternance

	E_f (eV)	E_b (eV)
V_B	11.22	
V_N	8.91	
V_{BN}^{1st}	9.75	10.38
V_{BB}^{2nd}	16.15	6.29
V_{NN}^{2nd}	13.96	3.86
V_{BN}^{3rd}	13.39	6.74
V_{BB}^{4th}	22.09	0.35
V_{NN}^{4th}	16.96	0.86

Table 3.2: *Formation energies (E_f) and binding energies (E_b) of different sets of vacancy pairs in a h-BN sheet.*

boron-nitrogen [61].

We obtain a strong binding energy also for homonuclear vacancies in second neighboring sites (V_{BB}^{2nd} and V_{NN}^{2nd}), although this effect is less strong then for first neigboring vacancies. Two B vacancies in second neighbouring sites have a binding energy of 6.29 eV. Interestingly the intermediate N atom moves to adopt the site of one of the missing B atoms, structurally equivalent to the stable divacancy in graphite (Fig. 3.3). The N-N repulsion is overcome due to the energy saving associated with reducing the total number of dangling bonds by two. A similar binding energy of two N vacancies is seen.

In the third neighbour configuration one of the undercoordinated boron atoms surrounding the nitrogen vacancy bonds with one of the nitrogen atoms surrounding the boron vacancy (V_{BN}^{3rd} in Fig. 3.3). The shared bond between the two vacancies has a lenght as short as 1.24 Å compared with the 1.45 Å in h-BN. This contraction indicates a clear triple bond rehybridisation which plays a stabilising effect on the structure. Indeed, this third neighbour methastable $\mathrm{V}_B - \mathrm{V}_N$ complex has a formation energy of only 13.39 eV that compared to the formation energy of the two separeted V_B and V_N monovacancies gives a binding energy of 6.74 eV. The ability to rehybridise BN bonds can be seen in the stability of small BN based molecules; both $\mathrm{H_2B = NH_2}$ and linear $\mathrm{HB \equiv NH}$ have been chemically isolated [75] (structural analogues to ethene $\mathrm{H_2C = CH_2}$ and ethyne $\mathrm{HC \equiv CH}$), which form the structural motif of the perfect lattice, and reconstructed V_{BN}^{3rd} defect core, respectively. A similar third neighbour effect in carbon structures has been demonstrated to exist in graphite and dia-

mond [26] and have brought to a new interpretation for the phase diagram of vacancies mobility in graphite.

3.2 HREM experiments

Recent improvement in transmission electron microscopy techniques have shown the possibility of a direct visualisation of single atomic defects in layered structures. Hashimoto and coworkers in their pioneer work [16] have clearly shown the appearence, in a TEM microscope, of bright spots on the nanohorn walls[2] that have been interpreted as the effect of atom sputtering under the microscope electron beam. HREM simulated images of single vacancy structures reproduce well the three fold symmetry of the bright spots observed. In the same work they clearly distinguish the appearence of a kink in the walls of a single walled carbon nanotube associated with the presence a dislocation line along the nanotube axis.

Similar defective structures have been theoretically expected to appear also in BN nanotubes [35, 39, 77] but no direct experimental observation have been reported for single walled nanotubes. Goldberg *et al.* have shown the first TEM experiments on morphological modification in multiwalled BN-NTs induced by electron irradion [78]; the study was conducted using an acceleration voltage of 300 keV. TEM experiments in single walled nanotubes are more challenging and they require lower acceleration voltage in order to limit irradiation damages and not completely degrade the tube during the acquisition time. In the following, we will present a TEM study on the time evolution of single walled boron nitride nanotubes under electron beam irradiation. We will identify the appearence of point defects and dislocation lines on the tube walls.

3.2.1 High resolution electron microscopy experimental set-up

The microscopy observations were carried out in a FEI Tecnai F30 equipped with field emission electron gun. The detection of single vacancies is a challenging task since the resolution and the sensitivity of high resolution electron microscopy images (HREM) can be improved by increasing the beam intensity, the acceleration voltage and the exposure time, but these

[2]Carbon nanohorns are structurally close to carbon nanotubes but due to their large curvature radius they can be locally more assimilated to single graphene planes [76].

parameters also affect the emission rate of atoms under irradiation. The experimental conditions have then to be set up in order to obtain a compromise between good images and a reasonable exposure time without destroying the tubes. The operating acceleration voltage has been set at 200 kV which combined with a spherical aberration coefficient of 1.2 mm gives a maximum contrast transfer function (CTF) at around 3.5 Ångstroem. In addition, the high coherency of the field emission gun allows contrast at higher frequency, and a hexagon-hexagon distance of 2.5 Å can also be distinguished with this equipment (see as example the upper left corner of Fig. 3.4.a). At the chosen electron dose and voltage, knock-on processes are restricted to a rate which enables several images to be taken before defect creation alters the tube topology.[3] We have then followed the evolution of the systems employing a multi-exposure procedure, taking an image each second or half-second. This allows us to correct the specimen drift and to reduce the image noise using an average image, obtained by aligning each frame on the basis of the previous one and summing the film each two or three frames. Furthermore, we have mostly imaged bundles of tubes instead of single isolated BN SWNTs, these latter being more sensitive to vibrations induced by the electron beam due to charge effects. Simulated electron microscopy images have succesively been obtained using the multi-slice simulation method included in the SIMULATEM package [79].

3.2.2 HREM images

In figure 3.4 we show three HREM images of a bundle of tubes taken after an irradiation time of $t = 0$ s, $t = 20$ s and $t = 60$ s. Figure 3.4.b shows clearly the appearance of single bright spots on the lower tube of the bundle, associated with a small decrease in the tube diameter. After a long irradiation time damages provoke the collapsing of the tube (Fig. 3.4.c). As already demonstrated in the case of carbon [16], bright spots can be interpreted as the signature of point defects in the lattice of the tubes. HREM image simulations for the DFT optimised structure of a B single vacancy (V_B, Fig. 3.5.a and a BN divacancy V_{BN}, Fig. 3.5.c) in a (14,0) BN nanotube can be seen in fig 3.5b,d. Within the experimental conditions, it is not possible to decipher the local point group symmetry of the individual defects.

[3]The knock-on cross section theory will be detailed in chapter 4 and total knock on cross section will be derived for carbon and boron nitride nanotubes as function of the electron beam energy.

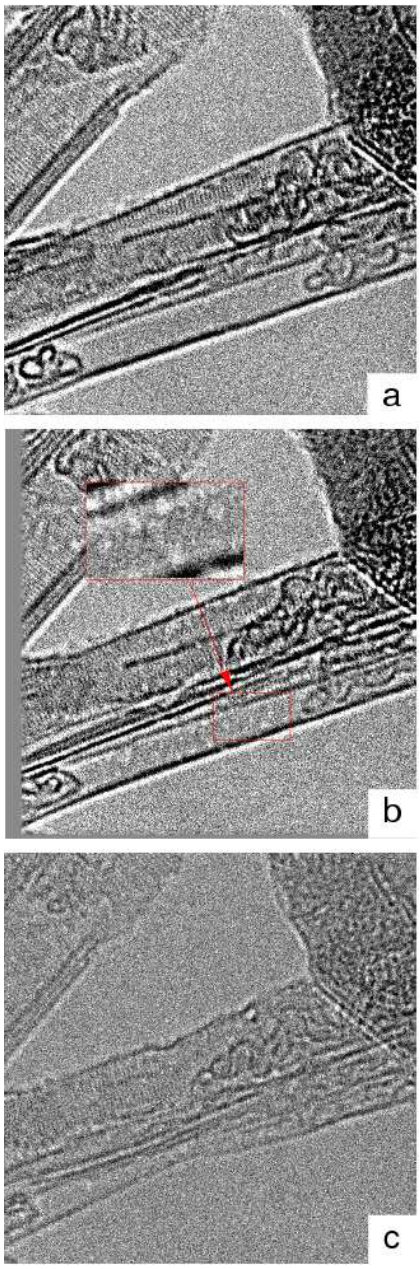

Figure 3.4: *Three HREM images of a bundle of boron nitride nanotubes taken after irradiation times of t=0 s (a) of t =20 s (b) and t=60 s (c). Image b shows the appearance of single bright spots on the lower tube of the bundle associated with a small decrease in the tube diameter. As already shown in the case of carbon, such bright spots can be interpreted as the signature of point defects such as single vacancies. Image c shows that after a long irradiation time the tube collapses.*

In fact, V_N, V_B and V_{BN} all appear as a rounded bright spot for a large set of defocus values and geometries. The only noticeable difference is the higher contrast of a BN divacancy relative to monovacancies. Compared to carbon nanotubes or nanosheets [16], the contrast of single vacancies in BN nanotubes is reduced, due to the strong structural relaxation induced by the curvature and the heteronuclear nature of the materials. Considering the low formation energies of vacancy pairs in first neighboring sites discussed in Sec. 3.1.3 we can affirm that both experimental and theoretical results agree that the observed individual defects are likely to be primarily BN divacancies.

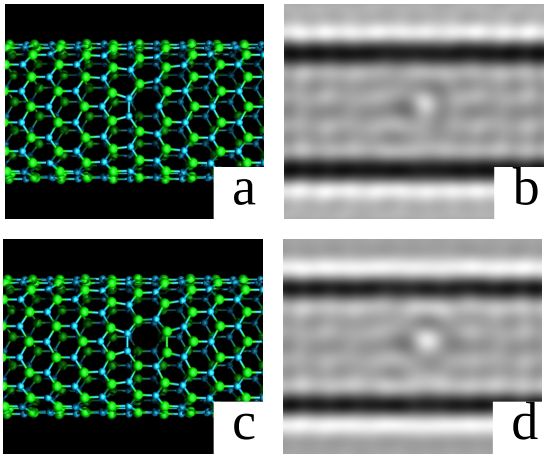

Figure 3.5: *Relaxed structures corresponding to single boron vacancy (a) and BN divacancy (c) for a (14,0) tube. Corresponding HREM simulated images (b, d).*

In figure 3.6.a,b we show two HREM images of a bundle of tubes taken after an irradiation time of $t = 0$ s and $t = 20$ s, the same conditions as the previous illustrated case. Starting from a perfect single walled BN tube, after irradiation a kink appears in the side walls associated with a local diameter reduction necessarily associated with a change of chirality. The change of chirality can be explained by a line of neighbouring vacancies running along the tube axis, with associated bond reconstruction (Fig 3.7.a). The terminating edge dislocation cores introduce five and seven fold member rings in the junction between the two parts of the tube (Fig. 3.7.c).

HREM image simulations are shown in figure 3.7.b,d for structures with a high number of vacancies, in order to create a long dislocation line. They reproduce well the kink structure characteristically observed under TEM irradiation (see Fig. 3.5.b).

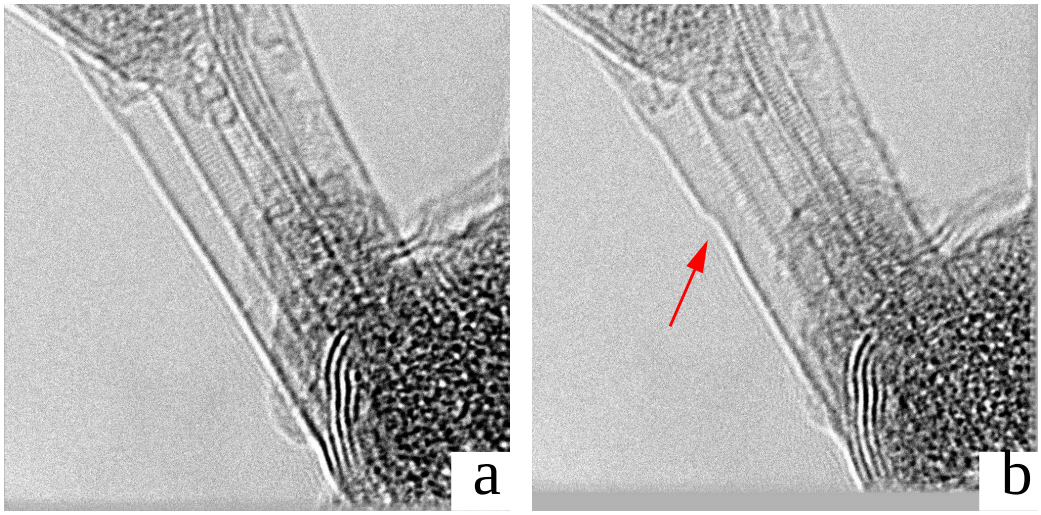

Figure 3.6: *Two HREM images of a bundle of boron nitride nanotubes taken after an irradiation time of $t = 0$ s and $t = 20$ s. In (b) the appearence of a kink on the tube wall is clearly shown.*

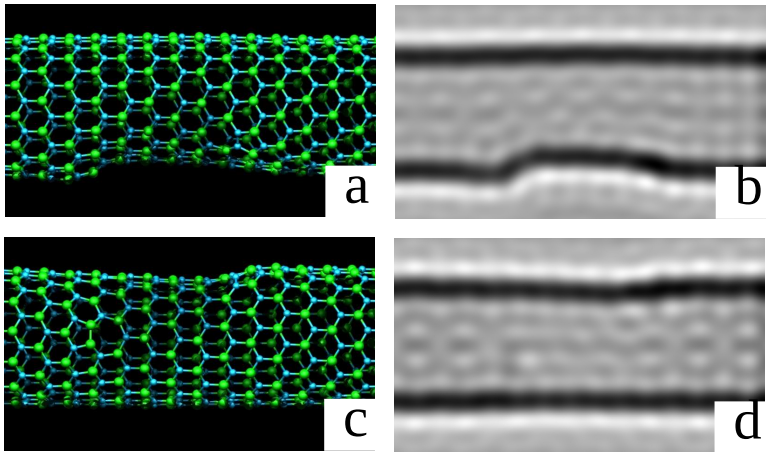

Figure 3.7: *Side view and a front view of the structure of a (14,0) nanotube with a dislocation line that reduce its diameter in the central part (a,c). In (c) it is possible to see the presence of a 5- and 7-fold member ring associated with the dislocation. Corresponding HREM simulated images in (b) and (d).*

3.3 A route from single vacancies to dislocation lines

In the previous section we have shown how defects generated by electron irradiation can be produced and imaged by transmission electron microscopy on single walled BN nanotubes. Defects are mainly generated by direct collisions with a sufficient energy transfer between the relativistic electrons of the beam and the atoms of the tube for sputtering the atoms from the tube lattice. In spite that this mechanism is well understood and can easily explain the creation of single vacancies on the tube walls, a more detailed discussion is needed for a correct interpretation of the appearence of more extended defective structures. In particular transmission electron microscopy images have shown that dislocation lines along the tube axis are a quite usual defective structure. There are potentially several ways to pass from a single vacancy to a dislocation line:

- re-organization and agglomeration of vacancies due to thermal vacancy migration;
- electron beam induced migration;
- preferential sites for vacancy formation.

In the following sections we will consider these different items. This analysis will give us the opportunity to treat problems of more general interest for the physics of defects in layered structures and nanotubes. In particular, we will discuss into details the phase diagram for migration of vacancies in h-BN and their thermal stability, the heating effect of the electron beam on the sample and the formation energy of vacancies forming a dislocation line.

3.4 Vacancy migration

The study of diffusion mechanism of point defects in h-BN and BN nanotubes is of fundamental interest due to the crucial role played by defects on electronic and mechanical properties of these systems. Migration of vacancies in graphite has been the subject of a large number of experimental [80, 81] and theoretical [82, 24, 25] studies, mostly motivated by the use of graphite as a neutron moderator in fission nuclear reactors. More recently

the interest on vacancy migration has been extended to carbon nanotubes [25]. This study has been motivated by recent developments in transmission electron microscopy techniques that have shown the possibility of monitoring *in situ* the evolution of defects at room temperature [16] and at more elevated temperatures [20].

A detailed description of migration paths and activation energy barriers is necessary for estimating vacancy diffusion coefficients and their temperature dependence. Knowledge of the total internal energy of the system is not sufficient to describe real thermal migration processes: since a defective crystal is a grand canonical ensemble a more appropriate thermodynamical function has to be considered for comparison with experimental conditions, as for example the Gibbs free energy. Temperature dependence of migration paths and activation barriers can then be taken into account, giving a more realistic picture of the migration processes.

Despite the structural similarity between carbon and boron nitride, the heteronuclear nature of boron nitride limits the transferability of what is known from carbon to this different compound. In spite of the large number of studies conducted on graphite [24, 25], up to now little is known about vacancy migration in layered BN systems. A theoretical study of thermal vacancy migration is h-BN is also motivated by the rising importance of h-BN as moderator and fuel coating in high temperature reactors.

In the following sections we will present our theoretical results on vacancy migration in hexagonal boron nitride sheets, considering single boron and nitrogen vacancies as well as divacancies. In paragraph 3.4.2 we will show different behavior for single boron and nitrogen vacancies, where intermediate metastable states appear in the migration path. We will describe then a complete phase diagram of migration processes (§ 3.4.4) which shows the importance of considering correct thermodynamical quantities in the estimation of migration barriers.

3.4.1 Methodology

Migration paths are derived using the Nudged Elastic Band technique (NEB), already described in paragraph 2.7. As already discussed, combining DFTB and NEB, we obtain a good compromise between computational time and accuracy in the description of phenomena occuring far from the equilibrium. NEB-DFTB calculations have been performed using the `deMon2k` code [56]

In order to correctly describe the migration path we have used a high

number of intermediate images in the NEB (from 20 to 50). After derivation of the minimum energy path, a more accurate value of the total energy for each point of the path was obtained by a single point density function theory calculation in the local density approximation (DFT-LDA) as implemented in the `AIMPRO` code [45].

Defective crystals are a great canonical ensemble. The correct quantity for comparison with experiment is not the total internal energy of the system but the Gibbs free energy:

$$G = U - TS + pV - \sum_i \mu_i N_i \tag{3.2}$$

where the total energy *U* of the system is the sum of the internal energy (U_{int}) and the vibrational energy (U_{vib}). The second term of the sum is the entropy S contribution to the free energy. The third term depends on pressure p and volume V and is commonly neglected, since usually the system is considered at constant volume and pressure. The last term depends on the number of particles N and their chemical potential μ and only has an influence when the number of particles changes.

For the calculation of vibrational energy and vibrational entropy terms we have considered a Boltzmann distribution of harmonic oscillators, which has been shown to give realistic results in the case of defect vibrational entropies [83, 84]. Vibrational energy can then be written as:

$$U_{vib} = \sum_{i=1}^{3N} \left\{ \frac{\hbar\omega_i}{exp(\hbar\omega_i/k_B T) - 1} + \frac{1}{2}\hbar\omega_i \right\} \tag{3.3}$$

where ω_i are the eigenfrequencies derived from the vibrational spectra of the defective structure, N is the number of atoms of the system and T is the absolute temperature. The entropy S can then successively be calculated according to the thermodynamical equation:

$$\left(\frac{\partial S}{\partial U}\right)_{V,N} = \frac{1}{\left(\frac{\partial U}{\partial S}\right)_{V,N}} = \frac{1}{T(U,V,N)} \tag{3.4}$$

on which the volume V and the number of particules N have been assumed to be constant. From Eqs. 3.3 and 3.4 the vibration entropy S_{vib} becomes:

$$S_{vib} = k_B \sum_{i=1}^{3N} \left\{ \frac{\hbar\omega_i}{k_B T} \left[exp\left(\frac{\hbar\omega_i}{k_B T}\right) - 1 \right]^{-1} - ln\left[1 - exp\left(\frac{-\hbar\omega_i}{k_B T}\right)\right] \right\} \quad (3.5)$$

In this work we have derived the eigenfrequencies by diagonalisation of the full dynamical matrix. The dynamical matrix is calculated numerically by means of finite differences of the forces. Since this task is extremely time consuming the use of standard DFT techniques is usually limited to a small cluster of atoms close to the vacancy, but this approach can reduce the accuracy of the derived thermodynamic quantities. The use of DFTB allows the construction of the Hessian matrix for the full system and it has been demonstrated to give results in a good agreement with DFT calculations [85].

3.4.2 Vacancy migration paths

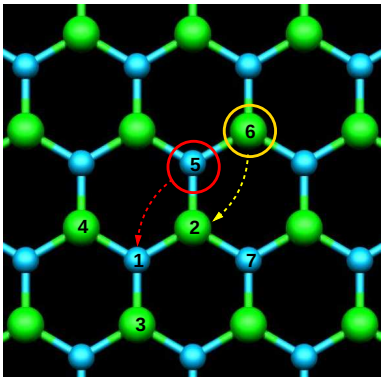

Figure 3.8: *Schematic numbering of atoms in a h-BN sheet. In a boron vacancy migration process the atom 5 moves to occupy the vacancy site left by atom 1 (red arrow). The same process occurs for a nitrogen vacancy migration (yellow arrow).*

The vacancy in graphite induces a Jahn-Teller distortion, forming a weak C-C bond between two of the vacancy neighbors [24]. Vacancy migration occurs through the displacement of one of the first neighboring atoms into the vacant site. The associated activation energy has been experimentally [80, 81] and theoretically [24, 25] estimated to be 1.4-1.8 eV. As already mentioned, vacancies in boron nitride show important differences due to the heteronuclear nature of boron nitride. Homonuclear B-B and N-N bonds are energetically unfavorable and both the single boron and nitrogen vacancies conserve the 3-fold D_{3h} symmetry around the missing atom without local reconstruction of dangling bonds.

In figure 3.8 we have numbered the atoms of a h-BN sheet in order to have an accurate identification in the text of atoms involved during the migration processes. We report in table 3.3 a summary of the zero kelvin

activation barriers for the different types of defects considered obtained by DFTB and DFT. The agreement between the two series of values validate the DFTB approximation adopted in the NEB procedure. Howerver in the following text and graphs we will refer to the more accurate results obtained by the successive DFT single point calculation.

	DFTB (eV)	DFT (eV)
B vacancy	3.3	2.6
N vacancy	6.1	5.8
BN divacancy: B moves	4.9	6.0
BN divacancy: N moves	3.0	4.5

Table 3.3: *Comparison of the zero kelvin activation barriers for different types of defects calculated by DFTB and DFT.*

We consider first a boron vacancy at site 1 of figure 3.8. The motion analogous to vacancy migration in graphite would be for a neighboring nitrogen atom (2, 3 or 4) to occupy the vacancy site 1. However, in boron nitride this results in a N-antisite defect with two homonuclear N-N bonds. Density functional calculations show that such a structure is not stable and spontaneously relaxes back to the initial boron vacancy. A similar result is obtained for the nitrogen vacancy; it is clear that the mechanism for vacancy migration in graphite cannot be extended to boron nitride.

The correct boron-nitrogen atom alternation can be conserved and a final configuration topologically equivalent to the initial one obtained if migration occurs through the displacement of a second neighbor atom to the vacancy. The mechanism is illustrated in figure 3.8 by the red arrow, where boron atom 5 moves to the empty site left by atom 1. Relaxed structures with the vacancy at sites 1 and 5 have been used as initial and final images in the NEB calculations, respectively.

Figure 3.9 shows that boron vacancy migration is a multistep process passing through intermediate metastable states. During the first step (Fig. 3.9.b) the bond between atoms 5 and 6 is broken, and the nitrogen atom 2 forms a homonuclear bond with atom 3. This process corresponds to a barrier of 2.6 eV. The system then falls into a metastable configuration where atom 5 bonds with atom 4 and a nitrogen-nitrogen bond is reconstructed (Fig. 3.9.c). This configuration, 1.38 eV higher than the stable one, introduces non-hexagonal rings into the BN-layer (a 4, a 5 and a 7 membered

ring). A new barrier of 0.72 eV occurs when the bond between nitrogen atoms 2 and 3 is broken (Fig.3.9.d). The path then repeats symmetrically (configuration of Fig. 3.9.e equivalent to that one of Fig. 3.9.c) until the new stable configuration is reached (Fig. 3.9.f).

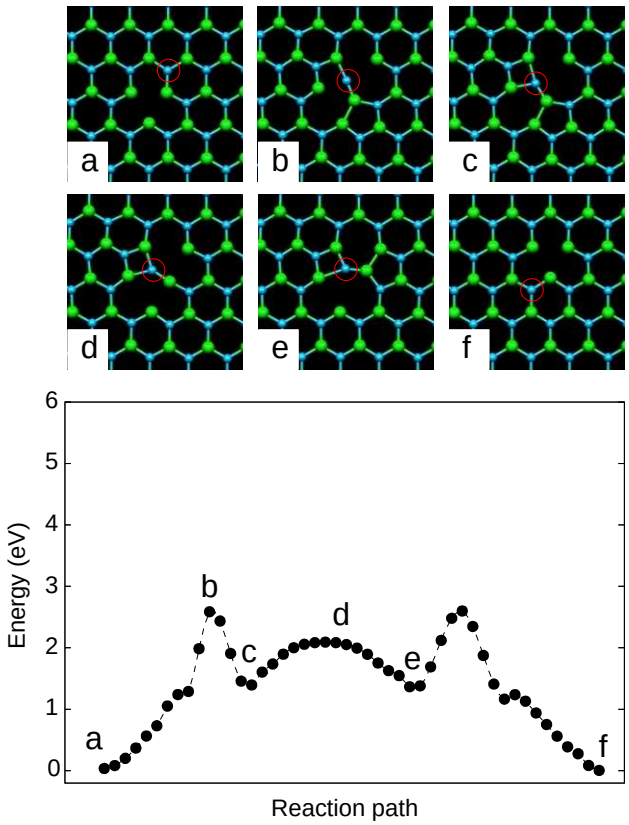

Figure 3.9: *Upper part: structural configuration along the reaction path for a boron vacancy migration. Lower part: energy evolution along the reaction path. The zero temperature activation energy is the energy associated with the saddle point configuration of picture b. Along the reaction path the system passes through the two equivalent metastable states of pictures c and d.*

Nitrogen vacancy migration follows a path equivalent to that illustrated for the boron vacancy, with structurally analogous intermediate metastable states (Fig. 3.10). Metastable states appear due to the reconstruction of a B-B bond; these are less energetically favorable than the corresponding states for the boron vacancy. Unlike the boron vacancy, the highest energy configuration does not correspond to the initial bond breaking (Fig. 3.10.b) moving into the first metastable state (Fig. 3.10.c), but instead to the barrier connecting the two metastable configurations.

The effective migration barrier corresponds to an energy of 5.8 eV, much higher than that of boron vacancies.

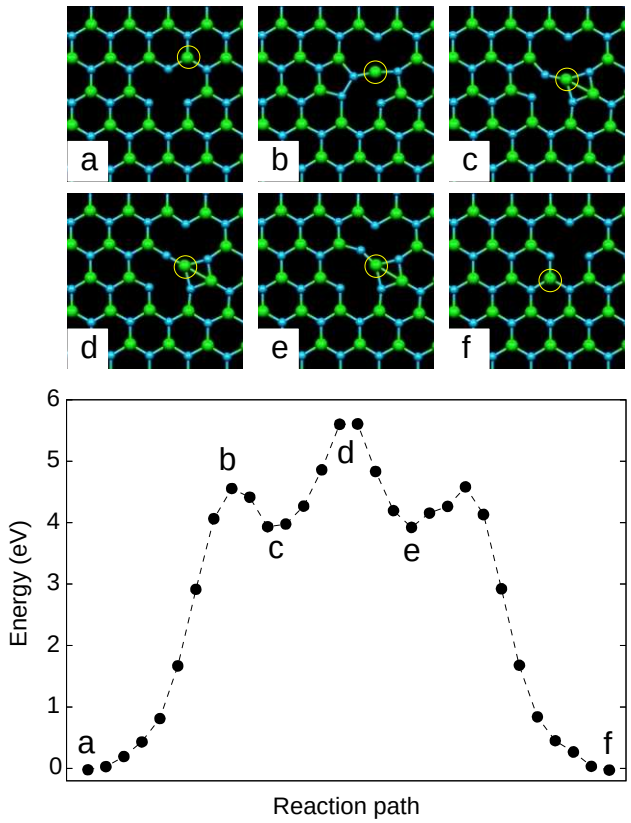

Figure 3.10: *Upper part: structural configuration along the reaction path for a nitrogen vacancy migration. Lower part: energy evolution along the reaction path.*

In section 3.1.3 we demonstrated the existence of a strong binding force between BN vacancy pairs. This interaction is maximized when vacancies exist in neighboring sites and tends to promote the appearance of divacancies under irradiation. In figure 3.11.a we show the structure around a divacancy site relaxed by DFT. Unlike the monovacancies, the defect undergoes B-B and N-N limited bond reconstruction, resulting in two pentagonal and one octagonal rings (see Fig. 3.3).

We have tested several possible migration paths for the divacancy, the most favorable corresponding to the minimum number of bond breaking processes along the path. The mechanism is illustrated by the yellow arrow in Fig. 3.11.a. In the final configuration, Fig. 3.11.b, atom 1 moves to the center of the divacancy, the homonuclear bond between atoms 2 and 3

is broken and both these two atoms bond with atom 1. A new pentagonal ring is then formed by reconstruction of the boron-boron bond between atoms 5 and 6. The final and initial structures, topologically equivalent, are related by a rotation of 30° perpendicular to the plane and a translation of 5.8 Å along a direction rotated by 30° with reference to the axis of the initial divacancy. An equivalent migration mechanism occurs when one of the two boron atoms of the second pentagon moves to the center of the divacancy and bonds with the two nitrogen atoms of the opposite pentagonal ring.

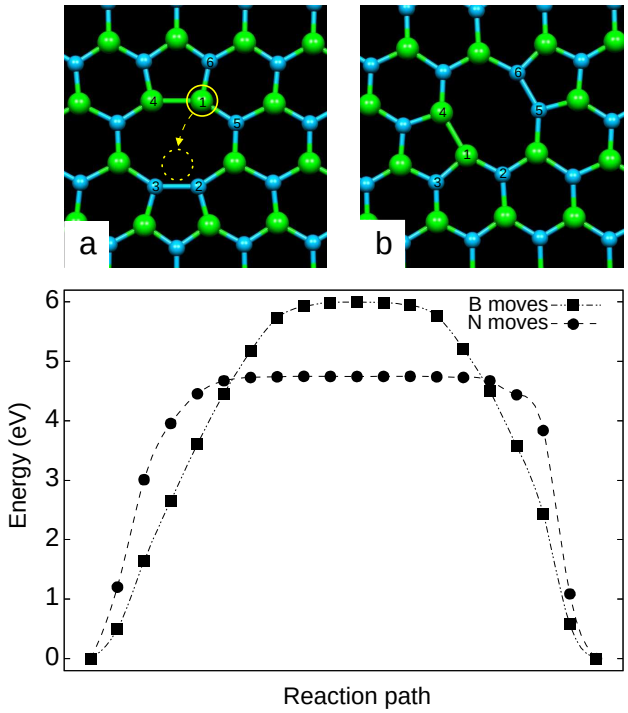

Figure 3.11: ***a*** *Relaxed structure of a BN divacancy. The yellow arrow represents divacancy migration via movement of the nitrogen atom 1.* ***b*** *final structure of the vacancy after migration.* ***Graph*** *energy evolution along the reaction path for divacancy motion involving a nitrogen (●) or a boron (■) atom.*

In figure 3.11 we show the energies of the minimum energy path for these two cases. Both curves exhibit a single saddle point, so unlike the monovacancies, divacancy migration is thus a single step process. The migration barrier obtained when moving the nitrogen atom is 4.5 eV, significantly lower than the 6.0 eV barrier obtained moving the boron atom. The energy difference is explained considering the bond breaking processes which occur during the migration. In both cases two heteronuclear B-N

bonds and one homonuclear bond are broken, but moving the nitrogen atom breaks the B-B homonuclear bond, whereas moving the boron atom breaks the energetically more strong N-N bond.

3.4.3 Activation barriers, Gibbs free energies

The energies reported above correspond to the 0 K temperature barriers, since the contribution of the entropic term and the vibrational energy to the Gibbs free energy were not taken into account. Gibbs free energies G have to be corrected calculating vibrational energy and the entropic term as given in Eqs. 3.3 and 3.5. Along the migration path nonequivalent structures have different vibrational spectra and consequently a different free energy temperature dependence. Considering explicitly the temperature dependence of the activation barriers ΔG gives a more physical picture of the vacancy migration phase diagram in boron nitride.

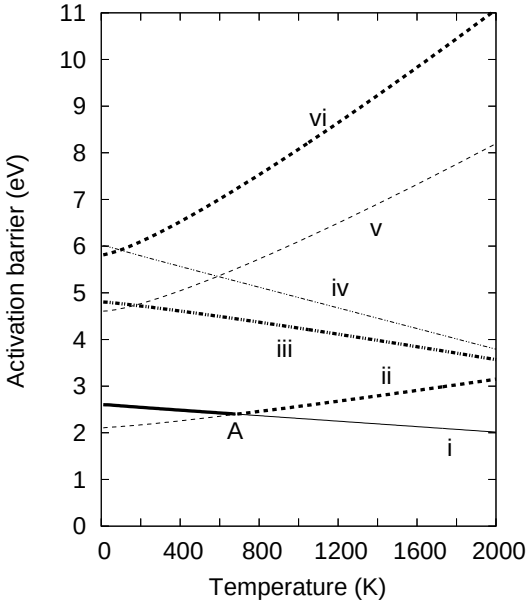

Figure 3.12: *Temperature dependence of the migration activation barrier for a boron vacancy (**i** for Fig. 3.9.b and **ii** for fig.3.9d), nitrogen vacancy (**v** for fig.3.10b and **vi** for fig.3.10d) and BN divacancy (**iii** moving the nitrogen atom and **iv** moving the boron atom). The bold lines represent the effective migration barriers for the different vacancies.*

In the case of a boron vacancy we observe an interesting effect. The free energy difference between the ground state (Fig.3.9.a) and the first saddle point (Fig.3.9.b) slightly decreases as a function of the temperature (Fig. 3.12 curve **i**) passing from 2.6 eV at 0 K to 2.25 eV at 1200 K. At the same time the entropy has a stabilizing effect on the ground state configuration in comparison with the second saddle point configuration (Fig.3.9.d) The difference of the free energy between these two states increases with temperature, passing from 2.1 eV at 0 K to 2.7 eV at 1200 K (Fig. 3.12 curve **ii**). Thus at 680 K (point A in figure 3.12) the curves **i** and **ii** cross and the second saddle point becomes the highest energy configuration along the

migration path. In this way we obtain a more complicated schema for the migration barrier as a function of the temperature: the activation energy decreases from 0 to 680 K reaching a minimum of 2.4 eV, then increases again once above 680 K.

In the case of the nitrogen vacancy, the free energy difference between the ground state and the two saddle points increases with temperature (Fig. 3.12 curve **v** for Fig.3.10.b and curve **vi** for Fig. 3.10.d). The activation barrier thus strongly increases with temperature from 5.8 eV at 0 K up to 8.6 at 1200 K. In contrast, the migration of divacancies becomes more favorable with increasing temperature. The difference in migration barriers to motion via boron (Fig.3.12 curve **iii**) or nitrogen (Fig.3.12 curve **iv**) atom displacement reduces, becoming negligible at elevated temperatures.

Explicitly including the temperature dependence of the activation barrier gives a more correct description of the phase diagram for vacancy migration. At 0 K nitrogen vacancies and BN divacancies only show a small difference in activation energies, but this difference strongly diverges with increasing temperature, resulting in a large difference in the migration probability as it will be discussed in the following section.

3.4.4 Diffusion coefficient

Vacancy mobility is driven by thermal stochastic excitations. In this context diffusivity D can be derived considering a simple Arrhenius formula

$$D = D_0 e^{-\frac{\Delta G(T)}{k_B T}} \tag{3.6}$$

where ΔG is the temperature dependent activation energy. The diffusion coefficient D_0 can be estimated by:

$$D_0 = \frac{d^2 \omega}{2} \tag{3.7}$$

where d is the distance between the initial and final position of the vacancy and ω is the migration attempt frequency, usually approximated by the Debye frequency of the system. In our systems the distance d is that between the centers of two adjacent hexagonal rings, 5.8 Å. For h-BN we have calculated by DFT-LDA the highest vibrational mode to lie at 1340 cm^{-1}, corresponding to a Debye frequency of $4.02 \times 10^{13} s^{-1}$.

The diffusion coefficients obtained for the migration processes described previously are plotted in figure 3.13. For the boron vacancy migra-

tion (curve **i** in Fig. 3.13) we have considered the highest saddle point at any temperature, point A represent the switch in the highest saddle point. Curve **ii** is the diffusion coefficient for a divacancy moving a nitrogen atom (corresponding to curve **iii** of figure 3.12). For all the range of temperatures considered in the graph the nitrogen diffusion coefficient is below 10^{-10} Å^2/s and so is not included here.

A rich phase diagram for vacancy migration can now be described. Up to 840 K all the diffusion coefficient are lower than 1 Å$^2/s$, and migration induced by thermal stochastic excitations can not occur within the characteristic time of TEM experiments and usual spot annealing conditions. Between 840 K and 1400 K boron vacancies diffusion coefficient are larger than 1 Å$^2/s$ and boron vacancies can be assumed to be mobile. The strong electrostatic interaction with single nitrogen vacancies will tend to trap mobile boron vacancies, promoting the formation of BN divacancy species. The probability of migration of divacancies is low up to a temperature of 1400 K, at which migration can occurs. The high migration barrier of N vacancies imply that migration cannot be thermally excited.

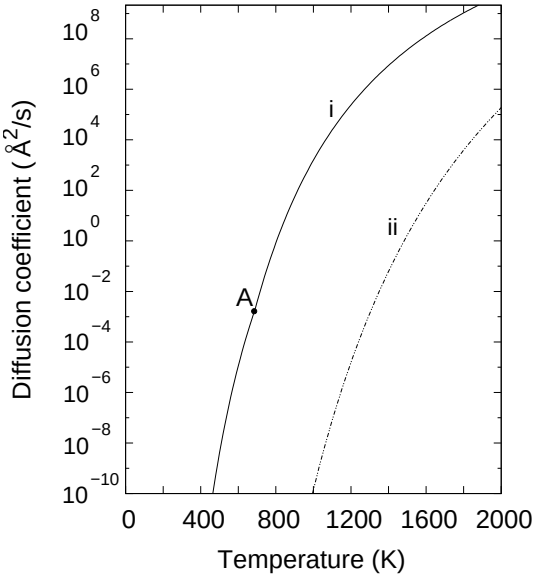

Figure 3.13: *Temperature dependence of diffusion coefficient for a boron vacancy (**i**) and for a BN divacancy (**ii**). The discontinuity at A corresponds to the switch in highest saddle point as shown in Figure 3.12. The nitrogen vacancy diffusion coefficient has values lower then 10^{-10} Å^2/s in all the temperature range considered in the graph.*

Thus through a spot annealing between 840 and 1400 K it may be possible to reduce the number of monovacancies in an hexagonal BN layer, transforming them in divacancies through a mutual annihilation process of single boron and nitrogen vacancies.

Similarly to vacancies other processes, e.g. Stone-Wales rotations, are of critical importance in plastic deformation processes. Once again if at first these processes could appear as similar for graphite and h-BN, they are certainly more complicated to generate in BN due to its hetero-nature.

Correspondingly, mechanical response and thermal treatment of damaged h-BN will be significantly different to that of graphite.

3.4.5 Vacancy migration in BN nanotubes

In Sec. 3.1.2 we saw that there is a qualitative structural difference between the monovacancy in h-BN and BN nanotubes: the curvature of the nanotube permit both for boron and nitrogen vacancies bond reconstruction between two atoms neighboring the vacancy, and this additional bond lie preferentially perpendicular to the tube axis. This effect has then a tube size dependences and decrease with the increasing of the tube radius.

In a similar way the reconstruction due to a weak Jahn-Teller distortion for vacancies in graphite [24] results much stronger in a single walled carbon nanotube due to curvature effects. Migration of single vacancies has been recently described on carbon nanotubes [25] showing an anisotropic behavior of the migration mechanism and an increasing of migration barrier compared to graphite. A critical diameter of 25 Å has been found above which the system behaves similar to graphite.

Migration in BN nanotubes should present a similar increase of migration barriers related with the bond reconstruction. The effect will be weaker for a nitrogen vacancy, for which a weak boron-boron bond reconstructs, than for a boron vacancy where a more energetically favorable nitrogen-nitrogen bond appears. However these additional homonuclear bonds are less strong than the equivalent additional carbon-carbon bond in carbon nanotubes. Therefore the increase of migration barrier due to curvature effect should be less prononced in boron nitride nanotubes than in carbon nanotubes and consequently the critical diameter should be smaller. We can then conclude that the described migration mechanisms of vacancies in hexagonal boron nitride can be extended to the case of BN nanotubes with few modifications even for the most narrow tubes.

3.5 Beam induced vacancy migration

In a transmission electron microscopy, inelastic collisions between the electrons of the beam and the electrons bonded to atoms leads to a significant energy transfer which is converted to a local heating of the sample [86, 87]. Direct phonon excitations have an extremely low cross section and this process has a minimal effect on the irradiation induced heating

of the sample. Thermal heating occurs then mostly through de-excitation of plasmons modes into phonons modes. Without entering into details of the different processes involved into inelastic scattering, we can consider more simply the energy transfered (E_T) each second to the sample which is successively converted into internal thermal energy. This quantity can be evaluated as:

$$E_T = I\langle E\rangle \frac{t}{\lambda} \tag{3.8}$$

where I is the incident beam current density, λ is average mean free path for all inelastic scattering and t is the sample thickness. The term $\langle E\rangle$ is the average energy loss (expressed in eV) per inelastic collision and it can be estimated as:

$$\langle E\rangle = \int EA(E)dE \Big/ \int A(E)dE \tag{3.9}$$

where $A(E)$ is the intensity of the energy loss spectrum at an energy E which can be experimentally obtained from a mesured EELS spectrum. The quantity t/λ represents the probability that one electron would transfer an average energy $\langle E\rangle$ into the irradiated zone. This quantity can be experimentally evaluated from:

$$\frac{t}{\lambda} = \log \frac{\int A(E)dE}{\int_{\text{zlp}} A(E)dE} \tag{3.10}$$

where in the logarithm it appears the ratio between the intensity of all whole energy loss spectrum and the intensity of the zero loss peak. From the works of Taverna et al. [88] on plasmons in single walled carbon nanotubes and Arenal et al. [34] on plasmons in BN nanotubes we have estimate t/λ equal to 0.02.

For calculating the effective temperature rising in the sample we have also to consider the effect of thermal dispersion into the energetic balance. Considering a total beam current I and a beam diameter d the equation relating heating and emission can be expressed by [87]:

$$I\langle E\rangle \frac{t}{\lambda} = \kappa S \frac{T - T_0}{L} + \pi \frac{d^2}{2} \sigma(\varepsilon T^4 - \varepsilon_0 T_0^4) \tag{3.11}$$

In this equation the final temperature of the sample is indicated as T. The first addendum of the second term represents the dispersion of heating due to linear conduction over a distance L in a material of thermal con-

ductivity κ, section S and with a thermostat temperature T_0. The second addendum considers the radiation of the sample where $\sigma = 5.67 \times 10^{-8}$ $\mathrm{W \cdot m^{-2} \cdot K^{-4}}$ is the Stefan's constant, ε is the emissivity of the specimen and ε_0 those of the environnement.

It has been demonstrated that carbon nanotubes have an exceptional thermal conductivity as high as $\kappa = 3500$ $\mathrm{W/(m \cdot K)}$ [89]. We can evaluate the effect of irradiation thermal heating considering an electron beam current I around 10 nA and a spot size diameter $d = 1$ nm. We chose a tube section $S = 1$ nm^2 and we consider the thermal conduction over the length of the scanned area L= 3 nm. The sample emissivity can be estimated in $\varepsilon = 0.98$ which correspond to the emissivity of graphite and the environnement emissivity is commonly set equal to $\varepsilon_0 = 0.5$ [87]. Integrating these experimental conditions into Eq. 3.11 we obtain that the electron beam produce a temperature rise of the order of magnitude of 10^{-3}K.

We saw in Sec. 3.4.4 that in h-BN (and by analogy in BN nanotubes) boron vacancies can migrate and eventually be trapped by a nitrogen vacancy forming a divacancy pair through a spot annealing at a temperature above 800 K. Divacancy becomes mobile at an even higher temperature, above 1200 K, and can cluster into bigger defective structures. Subsequently the limited thermal effect produced by electron irradiation can not be responsable for vacancy migration in the experiments conducted at room temperature. For concluding, in relation to the experiments presented in section 3.2, the bright spots (representing point defects) which can be seen in both TEM images (Figure 3.4.a,b) do not move over the 20 s between acquisitions, thus electron beam induced migration, if occurring at all, does not occur within the timescales required for vacancy line formation.

3.6 Preferential sites for vacancy creation

The analysis of the formation energy of divacancies conducted in section 3.1.3 can be extended by sequentially removing the least stable atom in the system. Without invoking vacancy migration, this leads to the formation of a vacancy line. The line reconstructs strong B-N bonds along its length, terminating in two edge dislocation cores. Removing an odd number of atoms, the tube relaxes in the same way as for a monovacancy (Fig. 3.14.a,c,e), reconstructing a homonuclear bond and moving the doubly coordinated atom outward. This is equivalent to the end dislocation core

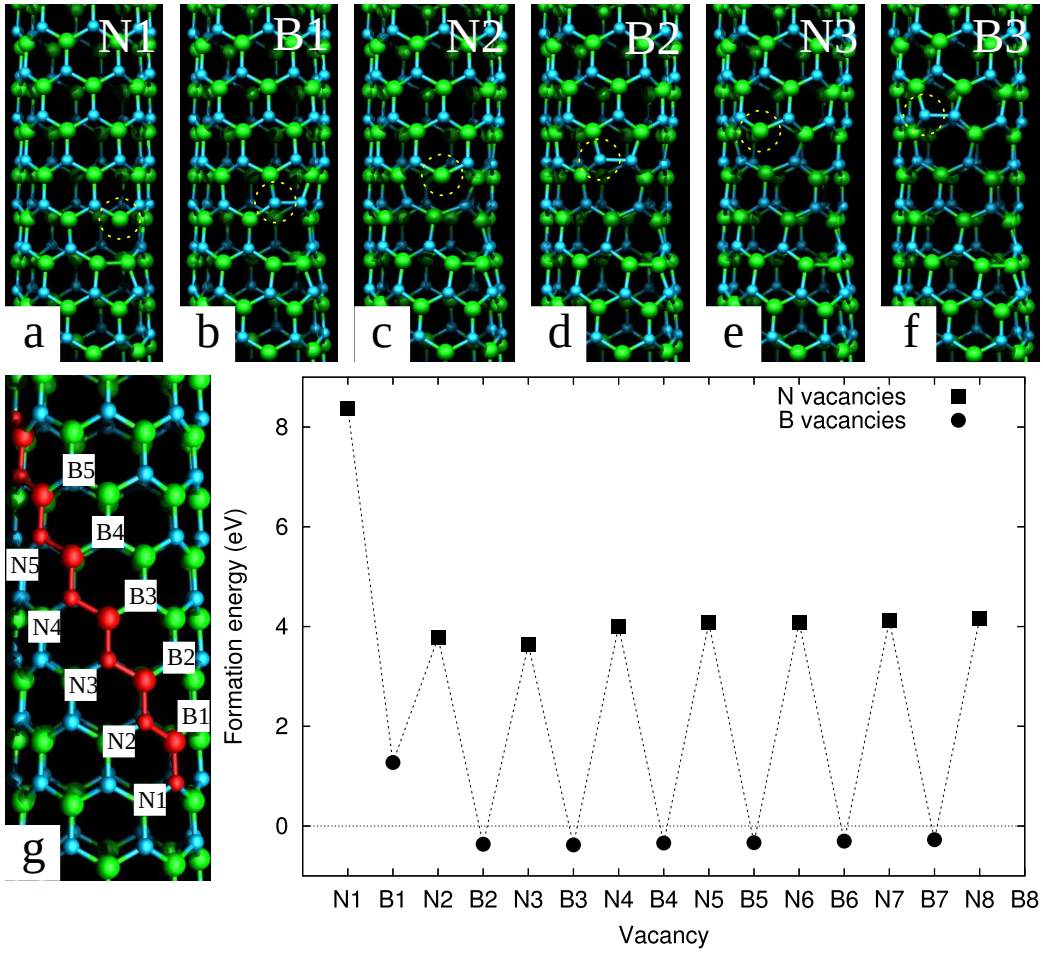

Figure 3.14: *a-f) Relaxed structures obtained by sequential removal of atoms along a dislocation line. The red line in (g) represents the most energetically favorable dislocation path. The graph shows formation energies of single vacancies on the path of the dislocation line. The formation energies are reduced drastically compared to those of isolated vacancies; indead vacancy formation becomes exothermic for odd-alternate removal after N2.*

lying in the shuffle plane. Each time an even number of atoms is removed, at the ends of the dislocation two pentagonal rings appear, one with a N-N bond, the other one with a B-B bond, i.e. the terminating dislocation cores both lie in the glide plane (Fig 3.14.b,d,f). Testing different orientations for the dislocation line we find that in a zig-zag tube the energetically most favorable configuration is for atoms to be removed along a sinusoidal line rolling around the tube (red line of atoms in Fig. 3.14.a). In the middle section the diameter decreases with a change of chirality; in the case considered we pass from a (8,0) tube to a (7,0).

In the graph of figure 3.14 we show the evolution of the formation energies of a vacancy line, starting by removing a nitrogen atom (Fig. 3.14.a). The graph shows that after having expelled a first BN unit the energies of formation of the next nitrogen vacancies are almost constant to a value of 4 eV, less than half that of an isolated nitrogen vacancy. Remarkably, for the boron vacancies we found an almost constant negative value equal to -0.2 eV. That suggests that once a nitrogen atom is removed along the dislocation line, the next boron atom is spontaneously ejected. The same effect is seen if the line begins with a B vacancy, *i.e.* the atoms are always ejected in pairs independent of how the line commences.

The strong decrease of the formation energy shown in our calculations strongly supports the idea of preferential sites for vacancy formation under electron irradiation. The appearance of a long dislocation line can be interpreted as a "laddering" mechanism that expands a single vacancy to an extended defective structure.[4] A similar decreasing on the formation energies of vacancies forming a dislocation line have been reported also for single walled carbon nanotubes [92, 93]. On this basis dislocation lines should appear also on carbon nanotubes by a similar "laddering" mechanism. However formation energies are only indirectly related to emission probabilities. Thus, in chapters 4 and 5 we will derive the total knock on cross section for atoms emitted during the first steps of the dislocation propagation process in a carbon nanotubes. Results will confirm the validity of the hypothesis of a laddering mechanism here formulated.

[4]Niwase has firstly proposed a similar process for explaining the generation of dislocation dipoles in irradiated graphite [90, 91].

3.7 Defects electronic structure

We turn now to the electronic structure of the defective systems presented along all this chapter. In Sec. 2.5.3 we saw that hexagonal BN has extremely flat bands throughout k-space and thus, unlike carbon, the calculated band gap of BN nanotubes remains almost fixed at the planar hexagonal BN value of ∼4.7 eV, with a small reduction as the nanotube diameter reduces [32, 33]. The intrinsic defects studied here introduce additional states into the gap. Single vacancies introduce half filled shallow acceptor states and thus may be expected to act as electron acceptors (tube or bulk, see Fig. 3.15). The main difference in vacancy states between the tube and the bulk is for the boron vacancy level at -1.2 eV: the doubly degenerate state of the plane loses its degeneracy in the tube owing to the breaking of symmetry related to the N-N bond reconstruction described above. This degeneracy splitting decreases with increasing tube radius, demonstrating again that the bond reconstruction depends on the local curvature.

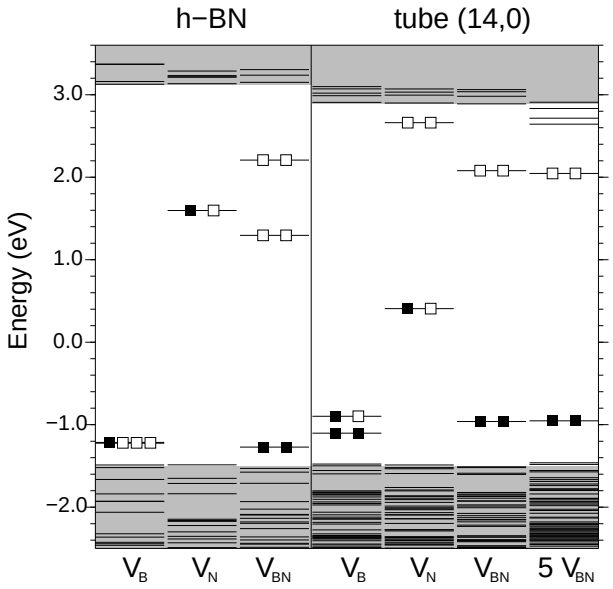

Figure 3.15: *Electronic structure of a h-BN sheet and of a BN zigzag tube in the presence of a boron (V_B) and nitrogen (V_N) single vacancies, of a boron-nitrogen vacancy pair (V_{BN}) and of a dislocation line formed by five divacancies (5 V_{BN}). The gray filled regions represent the valence and conduction bands of the perfect systems. Filled square indicate electrons, and open squares indicate holes.*

The electronic structure of the neutral divacancy is different (Fig. 3.15) with no half filled shallow state available for doping. Nonetheless, the neutral divacancy creates one discrete empty level in the band gap (two for the *h*-BN), flat throughout k-space and independent of tube diameter. Since we believe the dominant intrinsic point defect species in our sample to be divacancies, this demonstrates that the possibility of electrical doping BN SWNTs with vacancies via irradiation is unlikely. However,

the optical properties and conductivity may be altered by the presence of divacancies, and these levels should be readily detectable via optical spectroscopy.

The BN divacancy is actually an intimate vacancy pair example of a Schottky defect pair, *i.e.* a pair of oppositely charged defect centres. Although in general this pair of charged defects may be spatially distributed as long as their total net concentrations are the same, in practise there is strong electrostatic interaction between the two oppositely charged centres which will be maximised when they form in neighbouring sites. This effect is augmented in mixed ionic-covalent materials such as BN where an intimate vacancy pair has less dangling bonds than its separated vacancy pair counterpart. Coherent interaction of vacancies may be weak in the case of the bulk material, but may play an important role in irradiated nanostructures where a high defect density is obtained and there is a high local energy transfer during electron collision. We suggest that this is why we see intimate divacancy formation in our system, and indeed this may also happend in other ionic materials under irradiation damage.

At this point, we can mention that electron paramagnetic resonance (EPR) experiments have already evidence paramagnetic centres on γ rays irradiated h-BN [94] interpreted as the effect of single nitrogen vacancies. More recently similar paramagnetic defects have been reported on multi walled boron nitride nanotubes at an extremely low concentration, certainly less than one per tube and with no difference with the case of the bulk BN [74]. Nevertheless BN divacancies are non paramagnetic and might have been undetected in these previous experiments. Electrically and EPR active electronic levels associated with the two monovacancy species can also be remove through thermal treatements. Indeed we saw in Sec. 3.4.4 that through a spot annealing between 840 and 1400 K it is possible to reduce the number of monovacancies in an hexagonal BN layer, transforming them in divacancies through a mutual annihilation process of single boron and nitrogen vacancies.

The extended defects have a band structure very similar to that of the divacancy. As previously discussed, a dislocation line induces a change in the chirality of the tube, but since the electronic structure of BN nanotubes are not so sensitive to changes of the chirality, that aspect just reduces slightly the band gap but it keeps practically unchanged the band structure. Much more significant is the fact that at the two ends of the dislocation line the presence of five fold member rings induces two homonuclear bonds, giving rise to the empty state in the gap. This explains the

fundamental electronic similarity between a BN divacancy and a long dislocation line as shown in Fig. 3.15, and suggests that the additional empty states are spatially located at the two ends of the dislocation.

Although in principle we have an extremely complex system (multiple nanotubes with a range of diameters and chiralities, and a mixture of point and line defects), remarkably our experimental and theoretical study suggests that these complexity essentially reduce to a single simple, uniform electronic system; namely nanotubes with wide, flat bands separated by $\sim$4.4 eV [5], with one empty intrinsic defect level in the gap due to homopolar B-B and N-N bonds associated with divacancies and edge dislocation cores. This electronic simplicity makes BN SWNTs almost unique as a nanomaterial and suggests they may have an extremely bright future in fields such as photonics and optoelectronics.

[5]DFT-LDA calculations give a underestimated band gap of 4.4 eV. We remind here that higher level calculations give a band gap of 6.2 eV [32, 33] whereas it has been experimentally estimated in 5.8 eV [34].

CHAPTER 4

ELECTRON KNOCK-ON CROSS SECTION OF CARBON AND BORON NITRIDE NANOTUBES

ELECTRON bombardment techniques present three main advantages due to the low energy transmitted between the incident electron and the knocked atom. Firstly the transfer of energy and the irradiation dose can be so low that in a first approximation only individual defects are generated. Secondly the energy of the incident electron can be finely tuned around the threshold value where defects can just be created. Finally, electron beams in a TEM can be focused to form a nanometric probe, allowing control of the irradiated area with high spatial resolution [95]. Compared to other irradiation methods, electron irradiation presents the additional advantage that defect production can be easily observed and controlled in situ.

In this context, a correct derivation of the sputtering cross section and subsequently of the emission probability can bring important new insights for the design and interpretation of future experiments. Total knock-on cross sections for carbon atoms in nanosystems have already been derived under the hypothesis that atoms lie in an isotropic potential well [14]. However, the strong anisotropy of nanotubular systems requires us to go beyond this simple approximation. In their work Crespi and coworkers [96] reported several values of the escape threshold energy as a function of the direction of the kinetic energy of the escaping carbon atom. A threshold energy at around 17 eV was estimated for the radial escaping direction while energies ca. 40 eV were obtained for tangential ejection. Nevertheless, these calculations, based on tight-binding molecular-dynamic techniques were only performed for a limited number of angular directions and the knock-on cross section was then only estimated on the basis of an isotropic potential well optained at different atom positions around the

tube circumference. They concluded that for 800 keV electrons, knock-on displacements are 2-3 times more common for carbon atoms located on the front and back side of the tube than for carbon atoms located at the walls side.

More recently, Smith and Luzzi [97], taking into account a more complex scattering geometry, have shown that the threshold energy of the incident electron required to generate a knock-on carbon atom depends on the position of the carbon atom around the nanotube circumference. They derive a minimum incident energy of 86 keV required to remove carbon atoms from the tube section perpendicular to the electron beam. Higher energies exceeding 139 keV were estimated in order to generate knock-on carbon atoms from the tube wall section parallel to the beam. Nevertheless, the displacement energies were strongly approximated in their calculations and no local emission probabilities were calculated.

Despite the large interest shown in recent years for nanotube electron irradiation a complete description of the sputtering cross section is still missing. In the present chapter we will derive the total knock-on cross section as a function of the atom position along the tube circumference. The knock-on cross section obtained for different electron beam energies will be presented for carbon and boron nitride nanotubes. The chapter is divided into three sections. After this short introduction we illustrate in section 4.1 the theory of the knock-on process and of the scattering geometry. In section 4.2 we derive through extended molecular dynamics simulations the anisotropy of the emission energy threshold in a graphitic layer, in a h-BN layer and in a C_{60}. Finally in section 4.3 we report the total knock on cross section for carbon and boron nitride single walled nanotubes. Investigating the increase of the cross sections for atoms located at the neighboring of defective sites, we will provide a strong proof of the laddering mechanism proposed in the previous chapter for the formation of dislocation lines.

One further objective of a derivation of electron knock-on cross sections is to be able to use them in the field of electron microscopy. Thus, in the next chapter, we will illustrate how on the basis of the derived cross sections it is possible to obtain an extremely fine control of the irradiation conditions of single walled nanotubes.

4.1 Theory of the knock-on cross section

Due to the delocalization of excitations in metals or small gap semiconductors, deexcitations are not translated into single atom energy transfer, and radiolysis cannot occur. Thus since pure carbon nanotubes are metals or small gap semiconductors we can assume that under irradiation, defects appear mostly through direct knock-on collisions. In section 3.5 we also discussed how irradiation induced thermal effects are limited which shows that atom emission can not occur through thermal evaporation.

Under irradiation, atom emission occurs through direct interaction of the electrons of the beam with atom nuclei. The theoretical cross section for Coulomb scattering between a relativistic electron and a nucleus have been derived by Mott [98, 99] as a solution of the Dirac equation[1]. McKinley and Feshbach expanded the original Mott series in a power series [101] obtaining an approximate formula accurate up to the middle Z elements:

$$\sigma(\theta) = \sigma_R[1 - \beta^2 \sin^2 \theta/2 + \pi \frac{Ze^2}{\hbar c} \beta \sin \theta/2(1 - \sin \theta/2)] \tag{4.1}$$

where $\beta = v/c$, θ is the electron scattering angle and σ_R is the classical Rutherford scattering cross section:

$$\sigma_R = \left(\frac{Ze^2}{4\pi\varepsilon_0 2m_0c^2} \right)^2 \frac{1-\beta^2}{\beta^4} \csc^4 \theta/2 \tag{4.2}$$

Under the approximation of pure elastic collisions the maximum energy transfer T_{max}, corresponding to a scattering angle $\theta = \pi$, can be written as:

$$T_{max} = \frac{2ME(E + 2mc^2)}{(M + m)^2c^2 + 2ME} \tag{4.3}$$

where m is the electron mass, M the atom mass and E the energy of the incident electron. The angular dependence on the scattering angle θ of the transferred energy to the atom is then expressed as:

$$T(\theta) = T_{max} \sin^2(\theta/2) \tag{4.4}$$

Considering this notation equation 4.1 can then be rewritten, after a few algebraic steps, as a function of the emission energy T:

[1] For an exaustive review on electron scattering without atomic or nuclear excitations see Motz, Olsen and Koch [100].

$$\sigma(T) = \left(\frac{Ze^2}{4\pi\varepsilon_0 2m_0c^2}\frac{T_{max}}{T}\right)^2 \frac{1-\beta^2}{\beta^4}\left[1-\beta^2\frac{T}{T_{max}} + \pi\frac{Ze^2}{\hbar c}\beta\left(\sqrt{\frac{T}{T_{max}}}-\frac{T}{T_{max}}\right)\right] \tag{4.5}$$

In a monoatomic gas all the energy transferred from the electron to the atom is converted into kinetic energy. It is rather similar for an atom in a crystalline system if the transferred energy is much higher than the bonding energy of the atom. But if the transferred energy is of the same order of magnitude as the bonding energy, the interaction between the knocked-atom and its neighbors should be explicitly taken into account. Then, a simple model is usually assumed whereby damage can occur if the transfer of energy between the electron and the atom is larger than an emitting energy threshold E_d. For a transferred energy below the emitting energy threshold, the energy absorbed by the atom is converted into vibrational energy of the lattice.

To interpret experimental irradiation, the important quantity to consider is the total displacement cross section. It can be obtained by integrating the cross section of equation 4.5 inside the energy domain S over which emission condition are satisfied:

$$\sigma_d = \int_{S(T>E_d)} \sigma(T)\frac{4\pi}{T_{max}}dT \tag{4.6}$$

Despite the fact that crystalline solids usually have preferential directions for atom emission, E_d has been considered in many cases as an isotropic function. Under this hypothesis Seitz and Koehler [102] have derived the following formula for the emission cross section:

$$\sigma_d = 4\pi\left(\frac{Ze^2}{4\pi\varepsilon_0 2m_0c^2}\right)^2 \frac{1-\beta^2}{\beta^4}\left\{\frac{T_m}{E_d}-1-\beta^2\ln\left(\frac{T_m}{E_d}\right) + \pi\frac{Ze^2}{\hbar c}\beta\left[2\left(\frac{T_m}{E_d}\right)^{1/2}-\ln\left(\frac{T_m}{E_d}\right)-2\right]\right\} \tag{4.7}$$

Equation 4.7 can be useful to evaluate the total knock-on cross section [14, 96]. Nevertheless, this approximation is not valid for strongly

anisotropic systems where an angular dependence of the emission energy threshold occurs. In this case it is necessary to explicitly consider the emission energy threshold as a function of the emission angle and to integrate numerically equation 4.6 after having derived the correct integration energy domain S.

In figure 4.1.a the scattering geometry during the irradiation process is represented for a layered material such as a graphene sheet. We consider an atom sitting in the center of the referential. The layer of material lies in the XY plane. $\vec{e}$, the incidence direction of the electron, lies within the XZ plane at an angle α to Z, defined as the normal to the layer of material. It is then possible to describe the emission energy threshold for an atom emitted along an arbitrary direction $\vec{v}$ as a function of $E_d(\delta, \gamma)$, whose direction is defined in polar coordinates in terms of the polar angle δ and azimuthal angle γ.

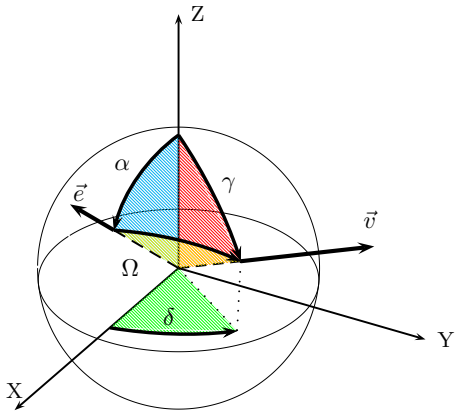

Figure 4.1: *Schematic representation of the irradiation geometry for a layered structure lying in the XY plane. The target atom sits at the center of the referential. $\vec{v}$ is atom emission direction, $\vec{e}$ is the incidence direction of the electron lying in the XZ plane.*

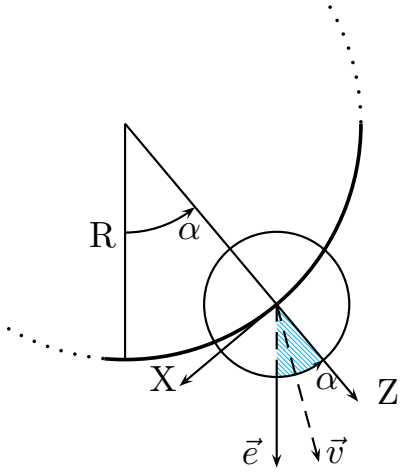

Figure 4.2: *Schematic representation of the irradiation geometry for a carbon nanotube, radius R, projected onto the XZ plane. The nanotube has its axis along Y, perpendicular to the incident electron beam. The projection of $\vec{v}$ is represented as a dashed vector in this figure, although we note that in the general geometry assumed in our calculation the direction of the emitted atom $\vec{v}$ is not confined to the XZ plane.*

We call Ω the emission angle defined by the angle between the electron incidence direction $\vec{e}$ and the atom emission vector $\vec{v}$. We can then rewrite equation 4.4 as a function of the emission angle Ω instead of the scattering angle θ, obtaining

$$T = T_{max} \cos^2(\Omega) \tag{4.8}$$

The total knock-on cross section σ_d is then obtained by integrating equation 4.5 within the energy domain S for which the emission conditions are satisfied, *i.e.*

$$T_{max} \cos^2(\Omega) \geq E_d(\delta, \gamma) \tag{4.9}$$

Transmission electron microscopy experiments are usually performed with nanotubes deposited onto a lacey carbon grid placed perpendicular to the TEM axis. Electron irradiation is then primarily performed in a non-tilted case where the tube axis lies perpendicular to the direction of the electron beam. In this configuration the position of the atoms around the tube circumference can be identified using the angle α defined by the direction of incidence of the electron and the local normal Z to the tube wall (see figure 4.2). If the tube diameter is large enough the structure can locally be considered as equivalent to a single graphene sheet.

As described earlier with the irradiation geometry, the emission energy threshold function $E_d(\delta, \gamma)$ shows a dependence on the polar angle δ and the azimuthal angle γ. Nevertheless, this dependence disappears during the calculation of equation 4.6 since these two angles define the integration domain, and the total knock-on cross section σ_d only depends on the angle α and the value of the incident electron energy E. We can then define a function $\sigma_d(\alpha, E)$ that gives the total knock-on cross section for each atom of the nanotube as a function of the incident electron energy and its angular position α around the tube circumference.

4.2 Emission energy threshold anisotropy

4.2.1 Computational method

The characteristic time of interaction of a relativistic electron with a nucleus is approximatively 10^{-21} s several orders of magnitude lower than the time of emission of the atom (10^{-13} s). The interaction of the elec-

tron with the atom can thus be reasonably considered as a punctual event. Under this hypothesis, the ejection mechanism can be obtained through the time evolution of the total system after an initial energy T has been transferred to the knocked atom. The ejection is achieved when the initial energy is sufficient to extract the atom from the plane. To map this emission energy threshold including the local anisotropy $E_d(\delta, \gamma)$, we have adopted a molecular dynamics approach in a canonical ensemble. Energetics and forces have been computed within the framework of the density functional tight binding theory (DFTB) as implemented in the deMon2K code [56]. DFTB technique is an ideal tool for these extended molecular dynamics calculations, since phenomena far from equilibrium can be described with the accuracy of a quantum method while the benefit of the reduced computational cost of TB-based techniques is kept. This approach has been used by Krasheninnikov et al. [93] and by Loponen et al. [103] to calculate the radial emission of atoms in carbon nanotubes and nitrogen doped carbon nanotubes. The radial emission condition gives the minimum emission energy threshold but in our calculation the whole emission energy threshold function is needed.

We first derive speeds and positions of all the atoms, equilibrating the system by molecular dynamics at a temperature of 300 K. In a second step we simulate the knock-on process changing progressively the momentum of one of the atoms. For a fixed emission direction defined by the angles δ and γ we perform a series of molecular dynamics simulations varying the initial speed of the scattered atom in steps of 0.002 Å/fs until we reach the speed at which the atom is emitted. The characteristic time for an atom to escape from the system is few tens of femtoseconds. Molecular dynamic simulations are performed for a total time of 150 fs. When the final position of the scattered atom is more than 5 Å far from its initial equilibrium position, we consider that the atom is free standing and that the initial momentum is above the emission threshold. We have followed this procedure for a carbon atom in a graphene plane, as well as for boron and nitrogen atoms in a h-BN layer. Calculations have been performed using periodic boundaries conditions in a 7×7 supercell; test calculations with larger supercells give similar results for the emission energy threshold. In order to obtain a map of the emission energy threshold $E_d(\delta, \gamma)$, the total procedure is then repeated for a large set of angles δ and γ describing a total of 526 nonequivalent emission directions. A finer angular mesh is then obtained by a linear interpolation of the DFTB calculated energies. Finally, this mesh is used in the numerical integration of the total cross section to

obtain the $\sigma_d(\alpha, E)$ which are discussed in section 4.3.

4.2.2 Carbon nanotubes

The map of anisotropy of the emission energy threshold, $E_d(\delta, \gamma)$, for a carbon atom in a graphitic layer is given in figure 4.3. Table 4.1 gives numerical values for specific angles. E_d shows little significant variance except for emission angles close to the plane.

The minimum value of E_d is 23 eV, for emission orthogonal to the plane ($\gamma = 0$). For initial momenta imparted within the graphene plane, id est $\gamma = 90°$, E_d shows a strong dependence on the angle δ. Initial nucleus momentum towards a hexagon centre ($\gamma = 0$, $\delta = 60$) gives E_d of 43 eV. However initial momentum in the direction of a nearest neighbor atom ($\gamma = 0$, $\delta = 0$) induces a large distortion of the lattice during the ejection process and thus high kinetic energies of the knocked atom, E_d up to 780 eV, are necessary for emission.

As discussed in section 4.1, irradiation defects can be produced when the transferred energy of an electron collision is larger than the displacement energy of an atom, i.e. T_{max} must be greater than $\min[E_d(\delta, \gamma)]$ for knock-on processes to occur. The equation 4.3, relating the T_{max} and the velocity of the incident electron can then be used, after inversion, to estimate the minimum electron energy needed to sputter an atom. In the case of a carbon atom in a graphene plane, we found by DFTB that $\min[E_d(\delta, \gamma)] = 23$ eV implies an electron beam energy threshold of 113 keV.

Smith and and Luzzi [97] have experimentally demonstrated by changing the accelerating voltage on a TEM that the electron energy threshold for damaging single walled carbon nanotubes lies between 80 and 100 keV. More accurate values are not available in the literature, but 100 keV seems to be nonetheless regarded as the upper limit by other authors [21]. Thus, the present DFTB calculations appear to overestimate the electron energy threshold by around 10-20 percent, which corresponds to an overestimation of the atom emission energy threshold of around 2-4 eV. As has been demonstrated by Krasheninnikov et al. [93] curvature and chirality can reduce the emission energy threshold by a few electron volts. For a tube diameter of 10 Å the threshold energy is 20.5 eV for an armchair tube and 18 eV for a zigzag tube. These energies increase with increasing diameter, tending asynthotically to the limit of 23 eV for a graphene plane. Another possible cause of the overestimation of the theoretical emission energy threshold energies comes from considering the atom sputtering mecha-

	γ (deg)	δ (deg)	E_d (eV)	E_{beam} (keV)
graphene: perfect	0	0	23	113
	90	0	780	
	90	60	43	
graphene: monovacancy	0	0	15	74
graphene: divacancy	0	0	19	95
BN sheet: B atom	0	0	15	74
	90	0	90	
	90	60	29	
BN sheet: N atom	0	0	14	84
	90	0	234	
	90	60	27	
C_{60}	0	0	20	103

Table 4.1: *Calculated emission energy threshold for a carbon atom in a perfect a defective graphene sheet, and for a boron and nitrogen atom in a h-BN sheet, as a function of different sets of the spherical angles γ and δ. The last column is the correspondent minimum electron beam energy (E_{beam}) at which defects starts to occur.*

nism as a pure knock-on process without any beam-induced electronic excitations. Their effect, as for radiolytic phenomena, is to reduce the bonding energy between the knocked atom and the lattice, in turn reducing the kinetic energy necessary for atom emission. However molecular dynamics simulations based on DFT consider the ground state electronic wave function and are not able to reproduce any coupling between the dynamical matrix and electronic excitations. A corrective term could be derived from a precise experimental measurement of the electron energy at which irradiation induced defects start to appear. However it is preferable to consider slightly overestimated values for the emission energy threshold derived from pure DFT based molecular dynamics simulation instead of adding any corrective term derived from the available experimental values which are only known with low accuracy.

4.2.3 BN nanotubes

Similarly to the case of a graphene sheet, we have derived $E_d(\gamma, \delta)$ for a boron and a nitrogen atom in a *h*-BN plane. The global trend of E_d is comparable with the results obtained for graphene. Table 4.1 gives E_d for

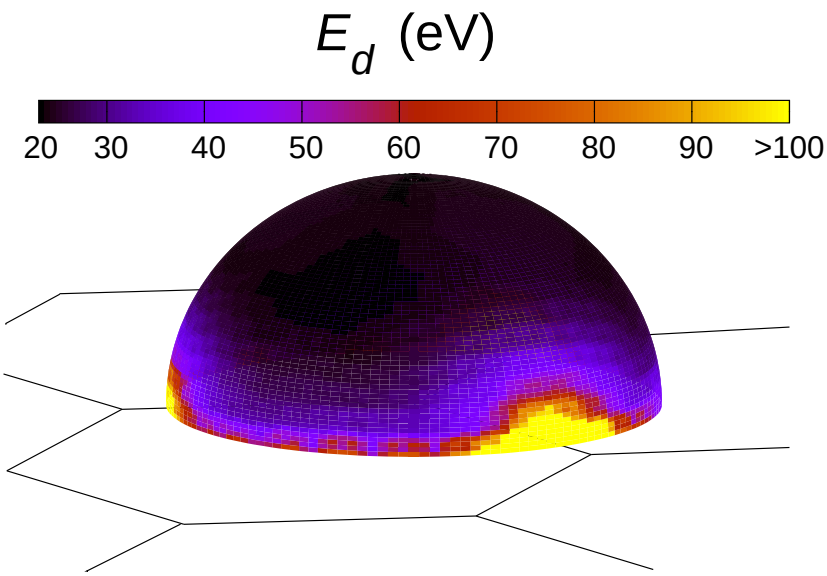

Figure 4.3: *Three dimensional representation of the map of the emission threshold function $E_d(\delta, \gamma)$ for a carbon atom in a graphitic layer as a function of the spherical coordinates δ and γ. The color scale indicates the emission energy values from 20 eV to more than 100 eV. The sphere indicates the emission direction for the ejected carbon atom. The sphere is centered on the initial position of the targeted C atom.*

different values of the angles γ and δ. There is a small difference, less than 1 eV, between the most favorable emission energy $E_d(0, 0)$ for boron and nitrogen. This corresponds to the small difference in formation energy for the vacancies which has been discussed in section 3.1.2: boron and nitrogen vacancies in planar *h*-BN have formation energies of 11.22 eV and 8.91 eV respectively.

However the atomic mass dependence of the transmitted energy (see equation 4.3) results in a different threshold for the electron beam energy at which atom emission occurs. A beam energy of 74 keV corresponds to a maximum energy transfer of 15 eV for a boron atom and the emission conditions are satisfied. However for the same beam energy the maximum energy transferred to a nitrogen atom is only 11.6 eV, lower than the minimum emission energy threshold. Emission conditions for nitrogen are only satisfied by increasing the incident electron energy to 84 keV. Thus for beam energies between 74 keV and 84 keV emission conditions are only satisfied for boron atoms, whereas above 84 keV nitrogen atoms can also be sputtered. No accurate experimental data are available on electron irradiation in *h*-BN based systems but as for the case of carbon we can

suppose that our values for the atom emission energy thresholds in boron nitride are slightly overestimated due the curvature and induced electron excitation effects. This second effect should be stronger in *h*-BN than in carbon due to the partial ionic character of the BN bonding and the wide band gap of this material, which results in stronger localization of electron excitations [32].

It is important to bear in mind that these results have been obtained for perfect graphene and hexagonal BN sheets, however after some irradiation a certain number of single vacancies will be present in the system. For vacancies in both graphite and *h*-BN the first neighboring atoms have a lower bond order; the vacancy in graphite induces a Jahn-Teller distortion forming a weak C-C bond between two of the vacancy neighbors whereas in BN-sheets there is no local reconstruction of dangling bonds. During sputtering of an atom neighbouring a vacancy, two bonds break instead of three for a fully coordinated atom. The case of a carbon nanotube has been treated in the works of Crespi et al. [96] and Krashenninikov et al. [93], where the minimum of E_d for an (8,8) armchair nanotube was shown to drop from 20 eV to 14 eV. In the case of boron nitride nanotubes we expect a similar lowering of the minimum electron beam energy at which atoms are sputtered, related to the reduced formation energy of vacancies neighboring a pre-existing vacancy (§ 3.1.3). In this context we can suppose that irradiating a BN nanotube with a beam energy between 74 and 84 keV will first generate a boron vacancy, but once these primary defects are created, nitrogen atoms on neighboring sites can also be emitted.

4.2.4 C_{60}, peapods, nanotube caps

Carbon nanotubes filled with fullerenes, system commonly called peapods, have been firstly synthesized by Smith & Luzzi [104, 105] and are now a new emerging material within carbon nanostructures. It has been shown that under transmission electron microscopy fullerenes are more sensitive to irradiation effects than the tubes in which they are encapsulated. Under certain irradiation conditions the resulting structures of a carbon peapod consiste of corrugated tubular like structures nested inside the original SWNT [106]. Combining electron irradiation with thermal heating promote the appearence of an encapsulated well crystallised structure and tend then to transform the peapod in a double walled nanotube. More recently Mickelson et al. [107] have encapsulated C_{60} molecules inside multi walled BN nanotubes (C_{60}@BN-NT). Under electron irradiation

carbon fullerenes can coalesce into a single walled carbon nanotube [108]. The obtained structure consist in an hetero nanotube where the external tubes are BN nanotubes and the most internal one a carbon tube. In particular cases on which the internal carbon tube would be conductor the obtained structure results to be a metallic-semiconductic coaxial tube.

In this context the knowledge of the emission energy threshold for an atom in a C_{60} fullerene acquire a particular importance. We obtained for a quasi radial emission direction a minimum emission energy threshold of 20 eV, two electronvolts lower then the emission energy threashold for a carbon atom in a graphene plane. Subsequently, if carbon atom in a single walled carbon nanotube starts to be ejected at an electron beam energy of 113 keV, an energy of only 103 keV is sufficient for sputtering atoms from a C_{60} fullerene.[2] These results show that under electron irradiation of carbon peapods it exists an energy domain at which only the fullerenes inside the tube are damaged, the tube walls lattice not beeing affected by the electron beam. This energy window represent an optimal experimental condition for producing double walled nanotubes from carbon peapods.

In a C_{60} all the carbon atoms are equivalent, beeing at the apex between one pentagonal cycle and two hexagonal cycles. Atoms adjacent to a pentagonal ring in carbon nanotube caps are in a similar local environnement. Consequently the emission energy tresholds at nanotube caps are equivalent to the one obtained for fullerenes. Also in this case irradiation in the energy window between 103 keV and 113 keV would damage the tube caps leaving the tube walls untouched. Up to now opening carbon nanotube caps have been obtained through chemical attacks. We propose an alternative way which use electron irradiation performed at the previously defined electron beam energy domain.

For BN nanotubes we saw that boron atoms are ejected at a a beam energy of 74 keV and nitrogen atoms at an energy of 84 keV. Therefore for C_{60}@BN-NT peapods it does't exist a particular energy range at which fullerenes can just be damaged. Experiments of Zettl [108] have been conducted on large multiwalled BN nanotubes filled with fullerenes which is a system less sensitive to irradiation effects than eventual filled single walled BN-NTs filled. To obtain double walled C-BN coaxial tubes from

[2] As discussed before emission energy thresholds are slightly overestimated since DFT based simulations do not take into account beam-induced electronic excitations. These effects are more important in fullerenes than in carbon nanotubes due to higher excitonic effects and this will lead to a subsequent higher over estimation of the energy at which defects start to occur.

electron irradiation of preexisting hetero peapods represent then a more difficult task.

4.3 Total knock-on cross-sections

4.3.1 Carbon nanotubes

In the previous section we mapped the emission energy threshold for a carbon atom in a graphene layer. These results can be used to evaluate the cross section in the case of carbon nanotubes. The energy domain of integration S of the knock-on cross section $\sigma(T)$ in equation 4.6 has to be derived as a function of the angle α defining the position of the atom around the tube circumference. In the case of a non-tilted nanotube imaged within a TEM, key angles are those corresponding to atoms located in tube region perpendicular (α=0°) and parallel (α=90°) to the incoming electron beam. We refer to these general orientations hereafter as the tube base (indicating equally to the top and bottom tube surface) and tube sides respectively.

The total knock-on cross section σ_d for a carbon atom in a single walled nanotube is plotted in figure 4.4 as a function of the polar angle α for different values of the incident electron energy in the range 100 keV to 1 MeV. The small high frequency fluctuations on the curves is due to numerical noise introduced by the reduced sampling in the integration routine.

Since $min(E_d) = 23$ eV, tubes are theoretically predicted to be stable under electron irradiation with beam energies below 113 keV. Between 120 keV and 150 keV, atoms from the tube base can be emitted. For example at 130 keV, α values in the ranges $-80° \rightarrow +80°$ and $100° \rightarrow +260°$ have non-zero cross sections. For an energy of 150 keV, there are no more forbidden area for the knock-on process and all the atoms of the tube can be emitted. The maximum cross section is 3.5 barn corresponding to $\alpha = 22°$ and to the three other symmetrically equivalent positions. At this energy, atoms in the tube base have higher sputtering probability than those in the tube walls where cross sections are still around one barn. This difference decreases with increasing incident electron energy, and for energies of a few hundred keV emission is largely homogeneous around the tube circumference. For example, at 300 keV the cross section varies between 5.5 barn at $\alpha = 54°$ and 8.5 barn at $\alpha = 0°$. At higher irradiation energies, atom emission from the tube walls becomes more favorable: at 1 MeV the total cross section is 13.3 barn for $\alpha = 0°$, 12.6 barn for $\alpha = 22°$ and 16.5

barn for $\alpha = 90°$. This may initially appear counter-intuitive, since side walls are usually regarded as low probability sites for knock-on processes, even with high incident electron energy[96]. We will discuss this point in more detail in section 4.3.4.

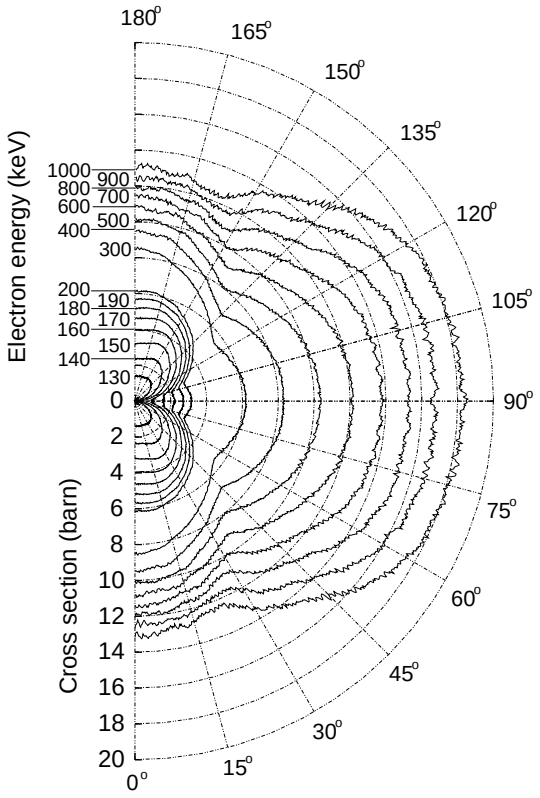

Figure 4.4: *Total knock-on cross section for carbon atoms in a single walled carbon nanotube as a function of their position α around the tube circumference. Angles $\alpha = 0°$ and $\alpha = 90°$ refer respectively to carbon atoms in the tube base and in the tube side. The electron beam is entering vertically from the top of the figure. Total cross section for the full tube ($0° < \alpha < 360°$) can be obtained by symmetrization of the plot. The curves are plotted for incident electron energies between 130 keV and 1 MeV representative of the voltages used in TEM.*

In a previous work [15] the total knock-on cross section for an electron beam energy of 300 keV was theoretically estimated to be 30 barns, within the approximation of an isotropic emission energy threshold equal to 15 eV. Crespi and coworkers [96] applying a similar hypothesis also mention cross sections from 10 to 50 bars. These values are generally higher that those we obtain here, and the difference shows the importance of explicitly considering the anisotropy of the function E_d. Several knock-on cross sections have been reported experimentally for carbon nanotubes and nanohorns. In both the paper of Hashimoto et al. [16] and Yuzvinsky et al. [21] a cross section of 160 barn is reported, derived by a rough estimation of the quantity of sputtered material as a function of the irradiation time. Hashimoto et al. observed defect density obtained by a limited dose irradiation at 120 keV. Yuzvinsky et al. investigated nanotube diameter shrinkage under higher irradiation doses at 100 keV; they derive then an extremely low value for the average emission energy threshold, estimated at 5.5 eV.

The small theoretical overestimation of the emission energy threshold

E_d for a flat graphene plane compared to a locally curved one, previously discussed in section 4.2.2, cannot account for this difference in the total knock-on cross section. Indeed tests we conducted by arbitrarily shifting the function E_d by 2-4 eV caused a variation in the corresponding total knock-on cross section of just a few barns. The large difference between experimental and theoretical cross sections primarily comes from the difficulty of precisely estimating experimentally the loss of matter after a certain irradiation time from which cross sections can successively be derived. Furthermore the cross section measured via the carbon sputtering rate will be overestimated because after the creation of primary vacancies, any further sputtering events have a larger probability of occurring for atoms neighbouring these pre-existing vacancies. This behaviour will be discussed more in details during the next section (§ 4.3.2).

Our calculated cross-sections for knock-on processes are primarily useful to estimate the amount of vacancies for low irradiation intensities, or to estimate the average dose for a first vacancy to be created. Dynamics involving larger changes of the tube structure such as tube collapses cannot be simply understood by the knowledge of the knock-on cross section for a perfect tubular system.

Once atoms are removed from their position in the lattice they can be ejected from the tube or emitted inside the tube cavity; the relative probability of these two events depends on the location of the atoms around the tube. Since cascade effects are limited to high accelerating voltages [14], at normal TEM operating voltages atoms emitted into the tube are trapped inside the tube cavity. Banhart and coworkers have discussen in one of their recent works [15] how atoms trapped inside the tube can diffuse along the tube axis and eventually nucleate in amorphous agglomeration. During the diffusion process atoms can also recombine with existing vacancies, reducing the total number of defective sites in the system. Experimental determinations of knock-on cross sections will also be altered by this effect, related to the complex dynamics of the sputtering processes.

4.3.2 Defective carbon nanotubes

In section 3.2 we have shown that under electron irradiation kinks could be produced in single walled BN nanotubes. This effect has been interpreted as the appearence of dislocations by sequential removal of a series of adjacent atoms (§ 3.6). Similar defective structures have also been observed in single walled carbon nanotubes [16]. In analogy with the BN

case, several authors have proposed a laddering mechanism on the basis of lower vacancy formation energies at atom sites neighboring a preexisting vacancy or located at the edges of a dislocation line [92, 109, 110]. However, we would like to underline once more that vacancy formation energies are only indirectly related to emission probabilities of atoms. To obtain a better justification on the existence of a similar laddering mechanism, we have derived the total knock on cross section for atoms emitted during the first steps of the dislocation propagation process.

Once a first vacancy is generated a pentagonal ring appears with the reconstruction of a C-C bond between two vacancy neighbors. The third neighboring atom remains with one dangling bond and shifts slightly radially outwards. The emission energy threshold of this atom is $\min[E_d(\delta, \gamma)] = 15$ eV. The minimum electron beam energy at which the atom can be sputtered is 74 keV, nearly 30 keV lower than for a perfect carbon nanotube (table 4.1). For higher electron beam energies we find that for this lower coordinated atom knock-on cross sections are almost one order of magnitude higher than for an atom in a perfect tube (Figure 4.5). Considering an electron beam energy of 130 keV on tube regions perpendicular to the electron beam a maximum cross section of 13.4 barn is obtained while a perfect graphitic environment shows only cross sections of about 1.4 barn. The asymmetry between the upper and lower part of the tube in figure 4.5 is due to the outward movement of the doubly coordinated atom, which makes emission into the tube cavity more difficult.[3]

After the removal of one atom close to a preexisting vacancy, the nanotube relaxes with the formation of a large divacancy and the creation of two neighbouring pentagonal rings. The cross section map reported in figure 4.6 corresponds to the emission of one of the atoms neighboring a divacancy. The emission energy threashold is 19 eV which means that atoms start to be ejected at an electron beam energy equal to 95 keV. For a beam electron energy of 130 keV a maximal cross section of 5.2 barn is found in the tube sections normal to the beam incident direction, showing a partial stabilization of the atom compared to the previous case. With further knock-on events, odd and even numbers of vacancies are sequentially obtained and form a dislocation line. For odd numbers of vacancies

[3]The asymmetry of this defective structure modify the angular dependence of the total knock-on cross section in function of the orientation of the vacancy axis with respect to the tube axis. Nanotubes with different chiralities, on which the vacancy symmetry plain is oriented in different directions, would have slightly different maps of the total cross section.

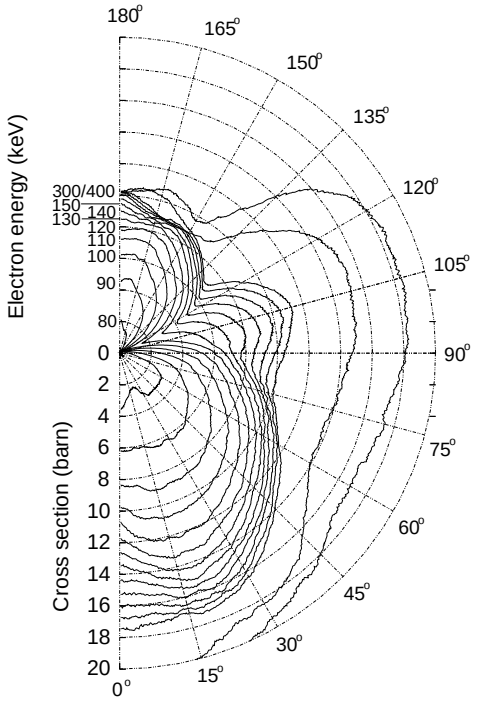

Figure 4.5: *Total knock-on cross section for a double coordinated atom neighboring a monovacancy as function of its position α around the tube circumference.*

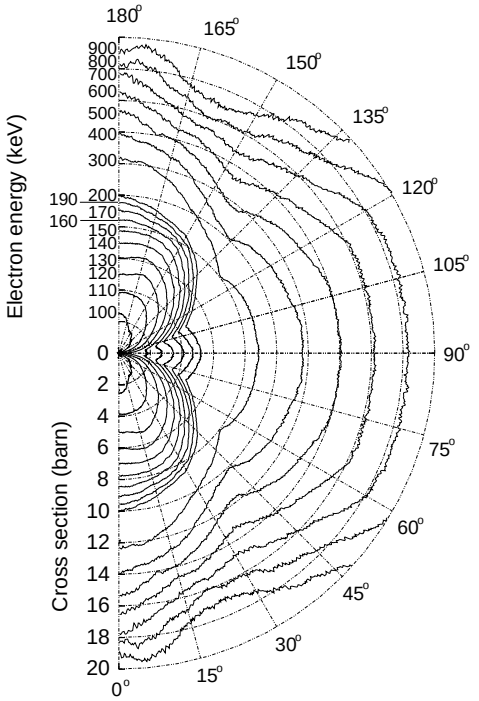

Figure 4.6: *Total knock-on cross section for a carbon atom neighboring a divacancy as a function of its position α around the tube circumference.*

the tube relaxes similarly to the monovacancy case, with the appearance of a pentagonal ring and a doubly coordinated atom. This is equivalent to the end of the dislocation core lying in the shuffle plane. Analogously the removal of an even number of atoms gives a structure with ends topologically equivalent to a divacancy, *i.e.* two pentagonal rings at the ends of the dislocation line. In this case both dislocation cores lie in the glide plane. Due to these morphological similarities we expect the emission knock-on cross section for the odd and even cases to correspond to values close to those obtained for the monovacancy and divacancy respectively. The high emission probabilities for atoms at the two ends of a dislocation compared to atoms in a perfect graphitic environment support the existence of preferential sites for atomic emission that provoke the propagation of dislocation lines under electron irradiation through a laddering mechanism.

We have found a direct experimental confirmation of this model in one of the TEM movies presented in a very recent work of Suenaga and cowor-

kers (Ref. [17], supporting materials movie S4). The movie shows an initial short dislocation which ends at the two kinks on the tubes side walls. During the acquisition time the two kinks moves far from each others with a related tube diameter reduction. This behaviour can be explained by the successive ejection under electron irradiation of atoms at the two dislocation edges which makes the dislocation propagate along the tube axis. In chapter 5 it will be shown

4.3.3 BN nanotubes

Figures 4.7 and 4.8 represent the total knock-on cross sections respectively for a boron and a nitrogen atom in a single walled BN nanotube as a function of their position α for different incident electron energies between 80 keV and 500 keV. In both cases the overall behaviour is similar to that for carbon.

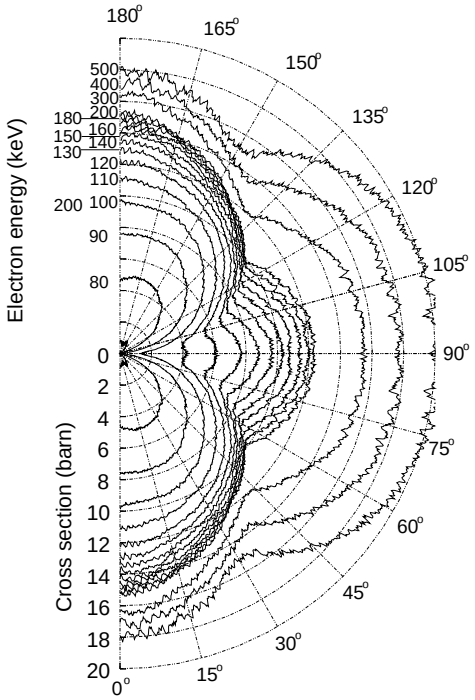

Figure 4.7: *Total knock-on cross section for boron atoms in a single walled BN nanotube as function of their position α around the tube circumference.*

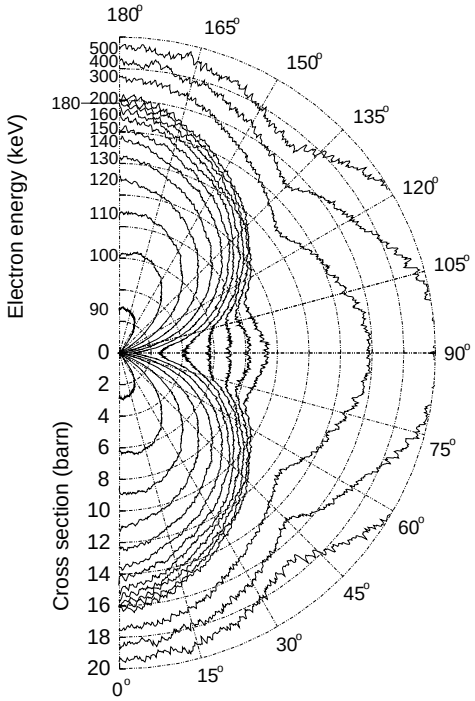

Figure 4.8: *Total knock-on cross section for nitrogen atoms in a single walled BN nanotube as a function of their position α around the tube circumference.*

As previously discussed (§4.2.3), at beam energies below 74 keV perfect BN nanotubes are not damaged by electron irradiation, and between 74 keV and 84 keV only primary boron vacancies can be generated. Between 84 and 140 keV the total knock-on cross section of a boron atom is always higher than that of nitrogen. For example at an irradiation energy of 100 keV the total cross section at $\alpha = 0°$ is 11.1 barn for a boron atom and 8.9 barn for a nitrogen atom; at $\alpha = 90°$ it is 4.1 barn for a boron atom whereas nitrogen atoms cannot be emitted for $72° < \alpha < 109°$.

Between 140 and 300 keV two regimes appear: on the tube base nitrogen sputtering becomes more favorable, while at the walls the total knock-on cross section is still higher for boron atoms. For example, at 190 keV, the boron knock-on cross section is higher than that of nitrogen for angles $56° < \alpha < 124°$. Above 300 keV nitrogen sputtering is the most probable event for all atoms around the tube circumference. We note that, as for carbon, at high incident electron energy the preferential site for boron and nitrogen atom ejection becomes the tube walls, $\alpha = 90°$, whereas at low irradiation energies it was the tube base, $\alpha = 0°$.

The knock on cross section for defective BN nanotubes has not yet been investigated which, as for the case of carbon tubes, would give a more complete vision of the effect of electron irradiation

4.3.4 Discussion on the knock-on cross section anysotropy

In the previous sections we have shown how for carbon and BN nanotubes the location of preferential sites for atom emission depends on the electron beam energy. Two regimes have been described: for low energies, atoms in tube sections perpendicular to the incident beam have the highest emission probability, while at high energy the cross section is maximum in sections parallel to the incident beam. To explain this behaviour we must consider the competition between the total integration domain S and the dependence on the transmitted energy T of the cross section $\sigma(T)$. We can clarify this point by examining in detail the solution of integral 4.6 in a simplified irradiation geometry. We consider here a simple two dimensional case confining the atom emission direction Ω to lie in the XZ plane defined by the normal to the graphene sheet and the electron incidence direction (see figure 4.1).

Figure 4.9 shows this geometry for two different zones of tube, perpendicular to the electron beam ($\alpha = 0°$) in the upper figure and parallel to the beam ($\alpha = 90°$) in the lower. The three curves represent as a func-

Ω	T (eV)	E_d (eV)		$\sigma(T)$ (barn)
		$\alpha = 0°$	$\alpha = 90°$	
$0°$	136	23	780	0.08
$30°$	102	24	30	0.27
$60°$	34	30	24	4.50
$75°$	9	69	24	71.82
$90°$	0	780	23	∞

Table 4.2: *Transmitted energy T, emission energy threshold E_d and cross section $\sigma(T)$ for different values of the emission angle Ω. The energy of the electron beam is 500 keV.*

tion of the emission angle Ω, the transmitted energy T (dashed line), the emission energy threshold E_d (dotted line) and the cross section $\sigma(T)$ (solid line). They have been calculated for an incident electron energy of 500 keV. In table 4.2 we report the values of these three curves corresponding to different choices of the angle Ω.

As one can see in the dashed curves, a maximum energy transfer T_{max} of 136 eV is obtained at $\Omega = 0°$ (i.e. when the atom is emitted parallel to the incoming electron beam) for an incident electron energy of 500 keV. Increasing Ω decreases the transferred energy (equation 4.4), becoming 0 for $\Omega = 90°$ (atom emission perpendicular to the incoming electron beam).

The E_d curves show two different behaviors. For $\alpha = 0°$ the emission energy threshold has a minimum of 23 eV for $\Omega = 0°$. E_d increases with Ω, almost diverging at $\Omega = 90°$. This can be understood since in this configuration the plane is perpendicular to the incoming beam and at high $\Omega = 90°$ atom emission is occurring parallel to the plane, an arrangement highly unfavourable for emission.

The situation is different for the E_d curve when $\alpha = 90°$ (sheet parallel to the incoming electron beam). The function E_d is then rotated by $90°$ compared to the $\alpha = 0°$ case. Thus E_d reaches its maximum at $\Omega = 0°$ (atoms emitted parallel to the sheet and incoming electron beam) and has a minimum equal to 23 eV for $\Omega = 90°$ (atoms emitted orthogonal to the sheet and incoming electron beam). The knock-on cross section $\sigma(T)$ has been represented on figure 4.9 using a logarithmic scale. Independently from the plane orientation this function has a strong dependence on Ω. It increases monotonically from a minimum of 0.08 barn at $\Omega = 0°$ and diverges at $\Omega = 90°$.

In figure 4.9 we have shaded the values of Ω for which the atom emis-

sion condition $T \geq E_d$ is satisfied. Due to the high symmetry values of α chosen, the integration regions are symmetric with respect to the electron incidence direction. For $\alpha = 0°$ the emission region is defined as $|\Omega| \leq 61°$. Inside this region the cross section σ varies between 0.08 barn for $\Omega_{min} = 0°$ and 5.08 barn at $\Omega_{max} = 61°$. For $\alpha = 90°$, a higher value for $\Omega_{max} = 65.5°$ is found, while at low angles there is now a forbidden zone within $|\Omega| \leq 8.5°$. In this case, σ is 10.0 barn at Ω_{max} and only 0.09 barn at Ω_{min}.

Comparing the two situations ($\alpha = 0°$ and $\alpha = 90°$), the difference in total allowed emission angles Ω is small ($\Delta\Omega$ is 122° and 114° respectively), showing larger geometrical possibilities for knock-on events in the case $\alpha = 0°$. At first sight this would appear to be in contradication with the previous finding where it was shown that the total cross section is highest in tube sections parallel to the beam ($\alpha = 90°$) at 500 keV. However the explanation is that the $\alpha = 90°$ geometry allows knock-on cross sections with larger values of Ω (i.e. atom emission at angles further from the incident electron beam direction). It is precisely for such larger Ω values that the cross section rapidly increases (we remind the reader that cross section is plotted on a logarithmic scale in Figure 4.9). In fact, although the energy threshold required to knock out atoms at low Ω values may be lower, such events have such small cross section that they do not contribute much to the total collision cross-section when larger Ω values are also involved. This is the origin of the highest cross section for tube sections parallel to the incoming electron beam for high beam energies.

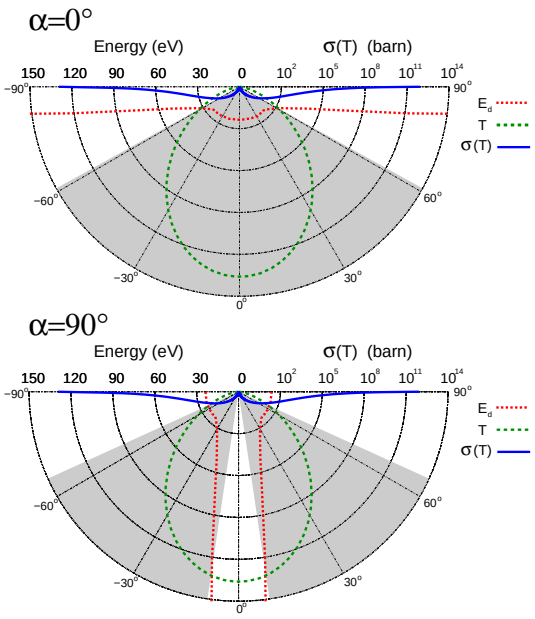

Figure 4.9: *Transmitted energy T, emission energy threshold E_d and cross section $\sigma(T)$ as a function of the emission angle Ω. The energy of the electron beam is 500 keV for both orientations $\alpha = 0°$ (tube section perpendicular to the electron beam) and $\alpha = 90°$ (tube section parallel to the electron beam).*

CHAPTER 5

NANOTUBE ENGINEERING USING A STEM

WE HAVE SEEN how irradiation is an important side effect of analytical experimental techniques using fast electrons as transmission electron microscopy does. Compared to non-spatially resolved analytical techniques, electron microscopy allows the observation of individual nanotubes at the cost of a consequent high irradiation density. In chapter 3 we have shown the possibility to image defective structures in BN-SWNT generated by the in-situ irradiation of the microscope electron beam itself and similar results have been previously reported by Hashimoto *et al.* on carbon nanotubes [16]. These experiments were conducted using a standard TEM experimental set-up, in these microscopy techniques samples are homogeneously irradiated and defects appear randomly all over the illuminated zone. This eventually leads during observation to extended wavy morphologies up to a complete tube amorphisation[19].

It has been recently demonstrated that the crystallinity of the tube can be preserved through thermal treatments during the TEM observation. Yuzvinsky and coworkers [21] combined electron irradiation with resistive heating, successfully demonstrating homogeneous shrinking of carbon nanotubes. Under similar experimental conditions Huang and coworkers [22, 23] have shown important plastic deformations of carbon nanotubes subjected to tensile strain. Authors propose that thermal treatments promote vacancy migration and their successive nucleation into dislocation lines, in aggreament with reported theoretical results [24, 25, 26].

Compared to other irradiation methods, the easily accessible focussing properties of electrons makes electron microscopy a technique which allows irradiation at an extremely high spatial resolution. Subsequently physical properties can be locally modified on limited sections of the tubes. Li and Banhart [27] have demonstrated for example that the use of focused probes on multiwalled carbon nanotubes (MWNT) can bend the tubes or

locally produce carbon onions from the tubes walls. Yuzwinsky and coworkers [28] have demonstrated that MWNT tubes can be cut with a SEM at a degraded vacuum even at low electron voltage.

Modification, in a controlled manner, of single walled nanotubes with electron beams represents a much more challenging task since smaller electron probes and narrower irradiation conditions are required. In this chapter we present a fundamental improvement in the irradiation techniques used, optimising irradiation conditions on the basis of knock on cross sections derived in chapter 4. We show that dislocations of a few nanometers in length, corresponding to the removal of few tens of atoms, can be obtained with nanometrical accuracy using subnanometrical focused probes in a dedicated scanning transmission electron microscope (STEM). Experimental shaping of single walled carbon and boron nitride nanotubes are then obtained demonstrating that chiralities of the tube can be locally changed with nanometrical control.

5.1 Irradiating carbon nanotubes

In the previous chapter we have derived total knock-on cross section as a function of the electron beam incidence energy and the position of the atoms along the tube circumference for atoms in a perfect carbon nanotube (§ 4.3.1) and in a perfect boron nitride nanotube (§ 4.3.2). Extending the calculations to atoms neighboring a monovacancy and a divacancy in a carbon nanotube we have proven the existence of a laddering mechanism which promotes under electron irradiation the appearence of dislocation lines instead of a random distribution of point defects (§ 4.3.3).

We saw also that experiments locate this energy threshold between 80 keV and 100 keV [97] whereas our theoretical estimation of the electron beam energy damaging theshold of 113 keV (§ 4.2.2). The overestimation of our theoretical value has been attributed to not taking into account electronic excitations effects in the molecular dynamics symulations. The derived electron beam energy dependence of the calculated knock-on cross section results then affected by a shift of about 20 keV. For comparing calculated knock-on cross section and experiments this energy shift can reasonably be supposed as rigid. We should then compare experiments conducted at a beam energy of 100 keV, around ~ 20 keV above the lower energy limit at which defects start to occur, with the respective knock-on cross cross section calculated at 130 keV.

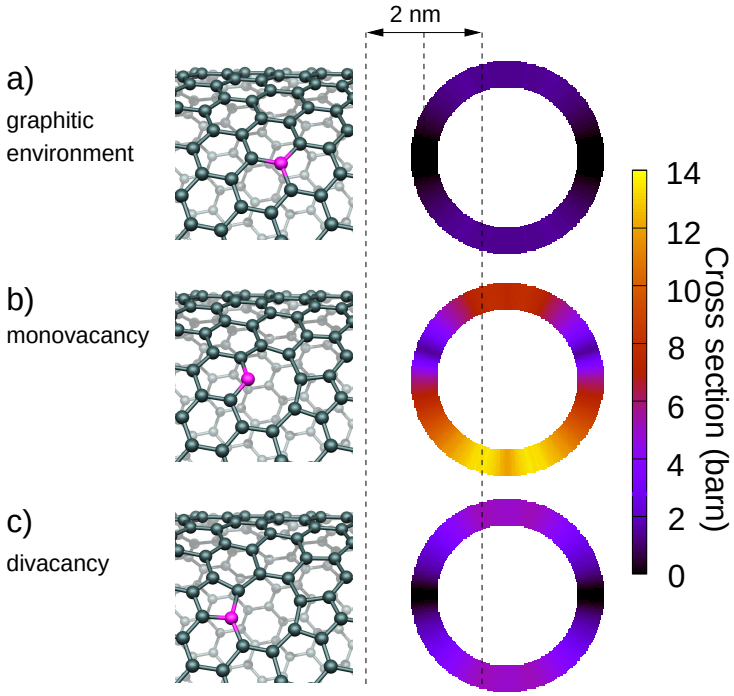

Figure 5.1: *Right part of the figure: total knock-on cross section as a function of the position on a tube section of an atom in a perfect graphitic environment (a), of a double coordinated atom neighboring a monovacancy (b) of an atom neighboring a divacancy (c). The beam incidence direction is aligned along the figure's vertical axis. The two vertical dashed lines represent the irradiated zone used to obtain experimental tube shaping. Left section: structures of the targeted nanotubes. Emitted atoms are marked in magenta.*

While knock-on calculations were performed for a wide range of incoming electron energies (§§ 4.3.1, 4.3.2), in figure 5.1 we summarise the results obtained for an electron beam energy 20 keV above the threshold energy at which defects can be generated. Indeed, experimental tube shaping has been done at the corresponding energy. Figure 5.1 shows the knock-on process for, respectively, an atom in a perfect graphitic environment (a), a doubly coordinated atom neighboring a monovacancy (b) and an atom neighbouring a divacancy (c). The right side graphs represent the transversal section of the nanotube where the color scale refers to the total knock on cross section. For a perfect carbon nanotube (Figure 5.1.a) a strong angular dependence on the emission probability is obtained. The cross section decreases with increasing angle between the beam incidence direction and the normal to the tube, and a forbidden emission region appears corresponding to the side walls of the tube.

Experimental conditions for single walled carbon nanotube irradiation have been optimized on the basis of the calculated total knock-on cross sections in order to obtain tube shaping capability. In figure 5.2 such a shaping of a single walled carbon nanotube is obtained by successive cycles of local electron irradiation. Five extended kinks have been obtained sequentially, on alternating sides of the tube. To reach such controlled irradiation, we select illuminated area, electron beam current density and electron beam energy in order to have a low atom ejection rate during the exposure time. Irradiation cycles were performed using an electron beam energy of 100 keV (roughly 20 keV above threshold voltage [97]), an electron current of ~ 140 pA and exposure times of 60 s. The beam convergence half-angle has been set to about 7.5 mrad which corresponds to an electron probe diameter of 0.8 nm. Five irradiation cycles were performed, choosing sequential irradiation zones on alternating sides of the tube at about 4 nm spacing along the tube axis. The high mechanical sample stability of the STEM microscope guarantees that during the irradiation time the irradiated area does not change due to sample drift. The scanned regions, represented in figure 5.2 by the dashed rectangles, are limited to a 2×3 nm^2 area and just partially illuminate the external section of the tube walls. As shown in figure 5.1, atoms located on these sectors of the tube have the lowest total knock-on cross section and therefore a better control of the irradiation process can be obtained using longer exposure times.

On the basis of the experimental irradiation conditions and the calculated cross sections we can calculate the total number of primary single vacancies that can be generated during the exposure time. Transmission

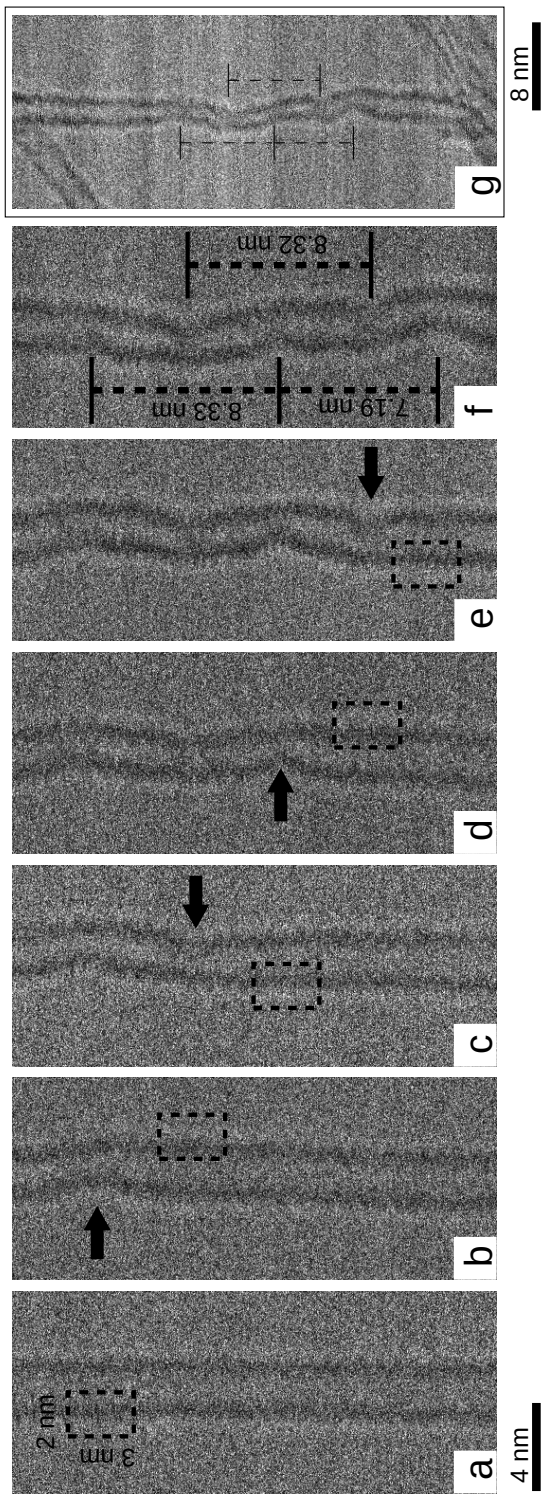

Figure 5.2: *Local electron irradiation of a single walled carbon nanotube. Irradiation zones of* 2×3 nm^2 *are represented by the dashed rectangles. (a) Original tube with a diameter of 2.4 nm and an apparent perfect crystallinity. (b) After the first irradiation cycle the tube shows a kink associated with a slight bending (black arrow) in direct correspondence with the chosen, irradiated zone. (c-f) Similar defective structures appear after each irradiation cycle as noted with arrows. (g) Final structure observed at a lower magnification demonstrating that the non irradiated zones at the two extreme parts of the tubes remain unaltered.*

electron microscopy experiments are usually performed with nanotubes deposited onto a lacey carbon grid placed perpendicular to the TEM axis. Electron irradiation is then primarily performed in a non-tilted geometry where the tube axis lies perpendicular to the direction of the electron beam (see Fig. 5.3). In this configuration the position of the atoms around the tube circumference can be identified using the angle α defined by the direction of incidence of the electron and the local normal to the tube wall. The number of events N which occurs at a position α on the tube for an irradiation time t can be obtained by:

$$N = jRLt \int_{\alpha_1}^{\alpha_2} \sigma(\alpha)\rho|\cos(\alpha)|\mathrm{d}\alpha \tag{5.1}$$

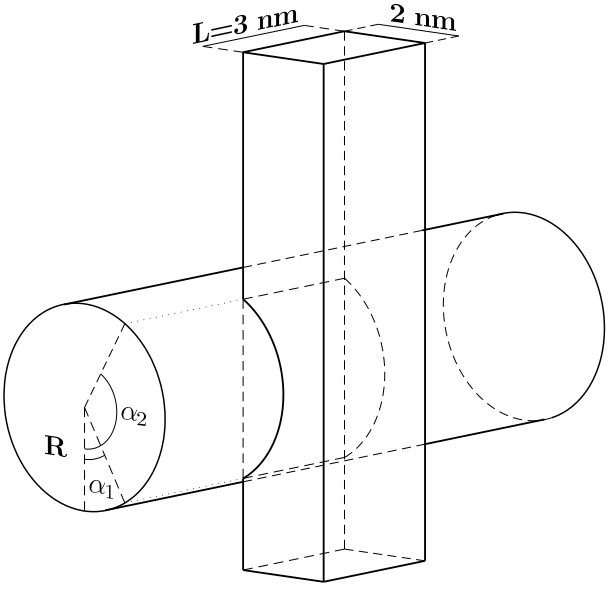

Figure 5.3: *Schematic representation of the irradiation geometry of a nanotube. The electron beam incidence direction is orthogonal to the tube axis.*

where ρ is the atom density of a graphene plane, j is current density, R is tube radius and L the illuminated length along the tube axis. α_2. ρ represents then the atom surface density. The intersection between the electron beam irradiation zone and the nanotube is defined the two integration limit polar angles α_1 and The term $|\cos(\alpha)|$ is the scalar product between the incidence direction vector and the normal to the tube surface. Considering our experimental set-up the operating current density in the microscope is about $150 \cdot 10^{28}$ $e^-/(s{\cdot}m^2)$. We consider an atom surface density of 9.68 Atom/nm^2 for a graphene plane and an effective illumination area defined by an illuminated lenght L = 3 nm and the two polar angles $\alpha_1 = 60°$ and $\alpha_2 = 120°$. Under these experimental conditions a total number of 2.74 vacancies are generated during an exposition time $t = 60$ s.

These primary vacancies act as seeds for subsequent atom removal and

finally for the creation of dislocation lines. Combining the higher knock-on cross sections for additional vacancies created adjacent to the first vacancy sites with the low concentration of primary vacancies, an overall emission of a few tens of atoms from the tube is estimated during each irradiation event.

After having irradiated a limited zone of the sample the imaging process does not provoke relevant irradiation damages in the specimen. Images are recorded while scanning in a time of 1 s a 20×20 nm^2 area. Magnification is chosen in such a way that the tube occupies less then $1/10$ of the image. On the other hand, the irradiation cycles practiced to remove atoms are obtained by scanning 2×3 nm^2 regions for a time of 30 s (where half of this region illuminate the tube). In this case, the tube receives an electron dose which is 150 times the dose of the imaging process. In the imaging process all the tube circumference is illuminated thus the integration limits in Eq. 5.1 have to be $\alpha_1 = 0°$ and $\alpha_2 = 180°$. Repeating the integration with these new experimental conditions we find that around 0.125 primary vacancies are statistically generated during the imaging process in the perfect tube which is neglectable compared to the emission during the irradiation cycles. We remember also that thermal vacancy migration or spontaneous emission of atoms is unlikely at room temperature for C [93, 26] and BN systems (§§ 3.4, 3.5). These are the reason why the tube shaping is stable and why kinks are only obtained in the regions where the electron irradiation conditions were optimized for.

5.1.1 Structures and image simulations

The introduction of a dislocation line produces a shortening of the tube whose length corresponds in a first approximation to the component of the Burger's vector along the tube axis. The bending of the tube visible in the microscopy images is then associated with shrinkage of one of the tube sides, and its magnitude depends on the orientation of the dislocation. We have studied through DFTB simulations the orientation effect of different dislocation lines in a chiral carbon nanotubes. A (20,5) single walled carbon nanotube with a tube diameter of 1.8 nm has been considered. In order to allow the bending of the tube, calculations have been performed in a cluster mode using models containing up to 1800 atoms. Dangling bonds at open caps have been saturated by addition of hydrogen atoms. Microscopy simulated images have successively been obtained from the optimised structures using the multi-slice simulation method included in

the `TEMSIM` packages [42].

In figure 5.4.a the removal of twelve atoms along a direction of 10.95° with respect to the tube axis does not produce any visible bending of the tube (Fig. 5.4.b) but two separated kinks are clearly visible in the left wall. When two dislocation lines are present in the tube, with a separation of several nanometers along the tube axis, the result is quite similar. No substantial bending of the tube is obtained and the dislocations are only visible though extended defects on the right and left part of the tube (Fig. 5.4.c,d). Removing the same number of atoms along a different direction of 79.05 °, closer to the normal of the tube axis, gives a larger shortening of one side of the tube, which corresponds after relaxation to a bending of the tubular structure (Fig. 5.4.e). The simulated microscope images with one or two dislocation lines (Fig. 5.4.d,f) reproduce well the behavior observed in the experimentally irradiated nanotubes (Fig. 5.2.b,c). A pentagon-heptagon defect pair with symmetry axis non-parallel to the tube axis changes the tube chirality from (*m*,*n*) to $(m \pm 1, n \mp 1)$. For particular pairs of the Hamada indices *m*,*n* a dislocation line can change locally the electronic character from semiconductor to metallic and vice versa [111, 112]. The use of electron irradiation techniques for arranging defects along the tube length can then in particular cases modulate the electronic structure of the tube.

5.2 Irradiating BN nanotubes

Irradiation conditions similar to the previously used for carbon nanotubes can be chosen for shaping single walled boron nitride nanotubes. When compared to carbon irradiation, defects in BN nanotubes appear at lower irradiation energies (§ 4.2.3). An irradiation beam energy of 80 KeV, slightly above the electron irradiation energy threshold, has thus been chosen in order to control the irradiation damage. Fig. 5.5.a presents a single walled boron nitride nanotube before irradiation; Fig. 5.5.b is taken after 60 s of irradiation, the dashed red rectangle in Fig. 5.5.a represents the 2×3 nm^2 scanned area. After irradiation the tube diameter is locally reduced in correspondence with the irradiated region and two kinks appear in the tube walls. In section 3.2 we obtained analogous defective structures in BN nanotubes through homogeneous electron irradiation and explained by the generation of a dislocation line along the tube axis. Similarly to single walled carbon nanotubes, it is possible to re-shape a single walled BN

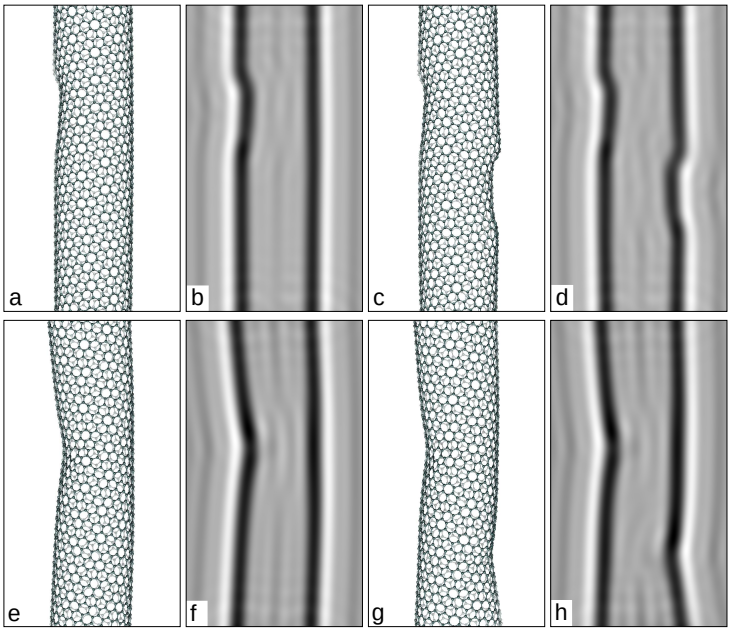

Figure 5.4: *Relaxed structure and respective STEM bright field simulated images for different dislocation lines in a (20,5) single walled carbon nanotube. Structures a and e correspond to a single dislocation line made of 12 missing atoms with different orientations. Structures c and g corresponds to the presence of two dislocations in the tube.*

nanotube by repeating the irradiation procedure in different sections of the tube (Fig. 5.5). Scanning regions are represented in Fig. 5.5 by the dashed rectangles and correspond to a 2×3 nm^2 area which partially illuminate the external section of the tube walls.

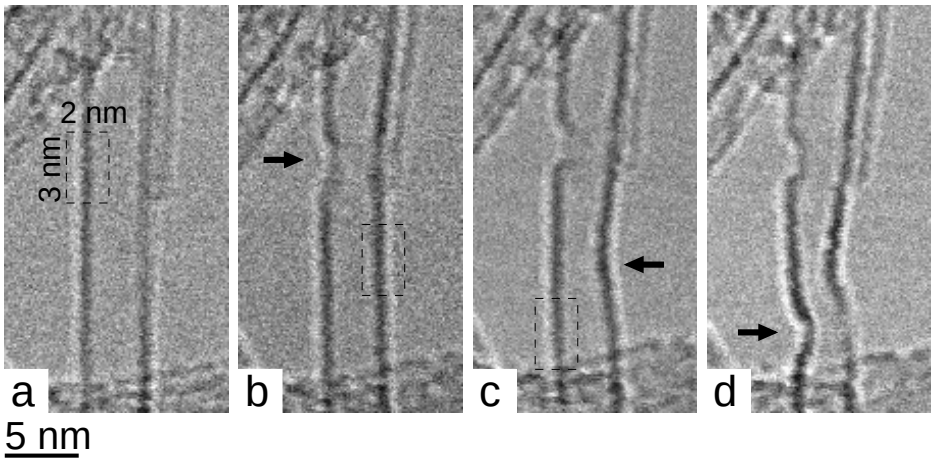

Figure 5.5: *Localised irradiation of a single walled BN nanotube. Irradiation regions are represented by the dashed rectangles. Starting from a perfect single walled BN nanotube (a) we obtain a progressive reshaping of the tube (b-d).*

In figure Fig. 5.6 we show that ,as for carbon nanotubes, local irradiation can produce a relevant bending of the tube. However this bending effect seams to be less common than for carbon nanotubes. We propose that also for BN nanotubes this effect is related with the shorting of one of the tube wall sides.

Annular dark field images, in figures 5.7.c and 5.7.d, give a direct correlation between local intensity of the image and local atomic density of the sample. In the graph of figure 5.7 we show the transversal intensity profile obtained for the central tube section indicated by the yellow rectangles in figures 5.7.c-d, the solid line refers to the tube before irradiation, the dashed line to the tube after irradiation. The maxima of intensity correspond to the side walls of the tube and the local minimum between them corresponds to the internal tube cavity. After irradiation the profile shows a decrease in intensity in correspondence with the irradiated right side wall and the tube diameter shrinks from 2.0 nm to 1.8 nm. The profile integral is directly proportional to the number of atoms in the considered region; on this basis we have estimated that a 4% of the atoms, corresponding to few tens of atoms, have been sputtered from the tube during the irradiation time.

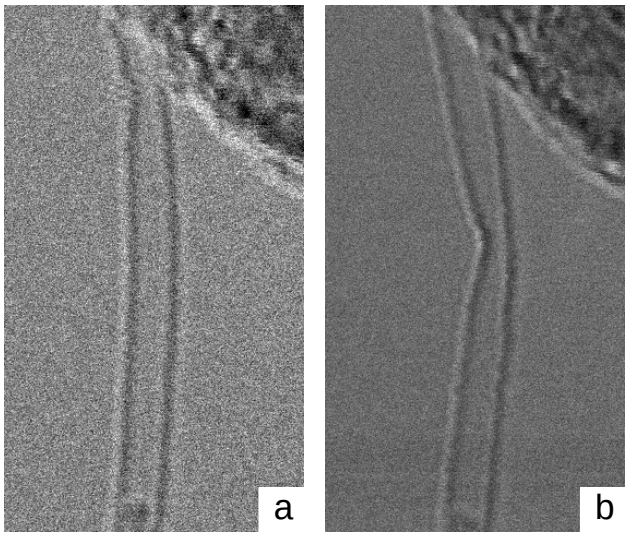

Figure 5.6: *BN nanotube bending obtained through localised electron irradiation*

In Sec. 3.7 we have shown that in BN nanotubes different types of defects give rise to a same electronic configuration, with one empty intrinsic defect level associated with homopolar bonds at edge dislocation cores. Through local irradiation we can introduce these additional electronic levels IN BN nanotubes with a nanometrical spatial distribution.

5.3 Fullerenes

In Sec. 4.2.4 we have found for carbon atoms in C_{60} fullerenes a lower emission energy threshold than for atoms on tube walls. We have then extended these results to carbon nanotube caps and even more generally to all carbon based structures on which pentagonal rings appear in honeycomb lattices. We have calculated the knock-on cross section for a carbon atom in a C_{60} at an irradiation energy of 130 keV, without considering the effect of the orientation of a C_{60} with respect to the incidence direction of the electron beam. We obtain a maximum value of 3.7 barn which compared to the maximum value of 1.4 barn obtained for a carbon atom in SWNT gives an emission probability three times larger.

Carbon cages with a diameter of few nanometers can be easily found in non purified carbon nanotubes samples. On them we have performed local irradiation experiments at an electron beam energy of 100 keV. Instead of defining a rectangular irradiation region as illustrated for nanotubes,

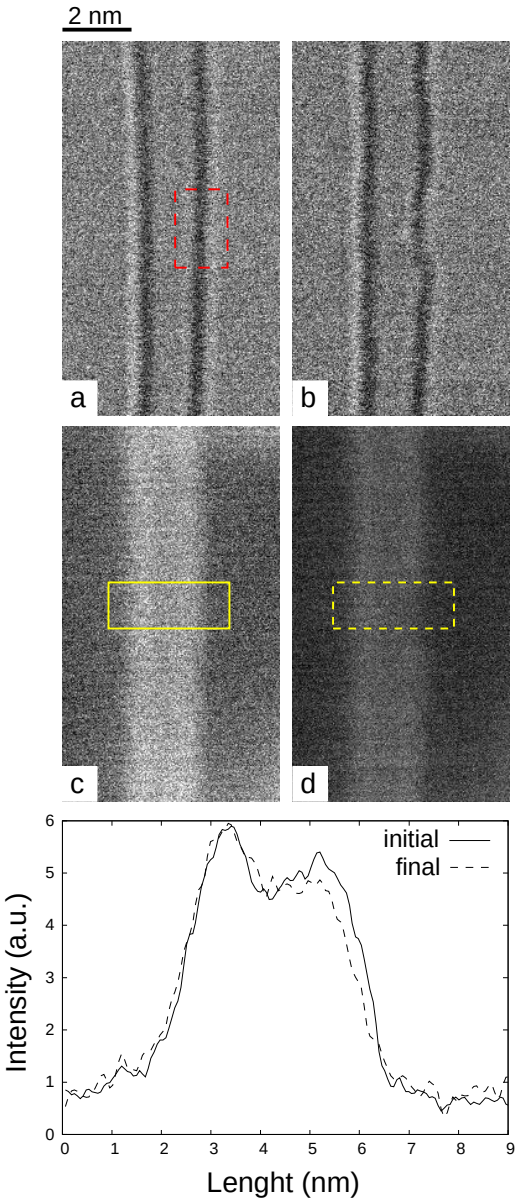

Figure 5.7: *Localised irradiation of a single walled BN nanotube. (a-b) Experimental STEM bright field images before and after the irradiation cycle of the nanotube. (c-d) Corresponding STEM dark field images before and after the irradiation cycle. Lower part of the figure, STEM dark field profile of the nanotube showing tube thinning on the right. Calculations using the tube diameter and the STEM profile give around 40 vacancies created.*

we have used a slightly different approach using a spot irradiation method on which the electron beam probe was left fixed. This amounts to have extremely limited irradiation areas of the size of the electron probe whose diameter in the VG microscope is about 0.8 nm. These irradiation conditions corresponds to higher current density and subsequently shorter irradiation times are needed in order to control irradiation damages. For our experiments we have used shot irradiations for times as short as 10 s. Results obtained for three irradiation cyles of a carbon cage are presented in Fig. 5.8. The black arrow indicates the position of the electron probe during each irradiation cycle. Starting from a close rounded structure (Fig. 5.8.a) we obtain after a first irradiation the appearence of a local ditching on one of the side of the particle (Fig. 5.8.b). Pentagonal rings are expected at the apex of the particle and thus apexes should be more sensitive to irradiation damages. Irradiating one of these appexes we obtain firstly a more rounded structure (Fig. 5.8.c) and then open the particle in correspondence of the irradiated zone (Fig. 5.8.d).

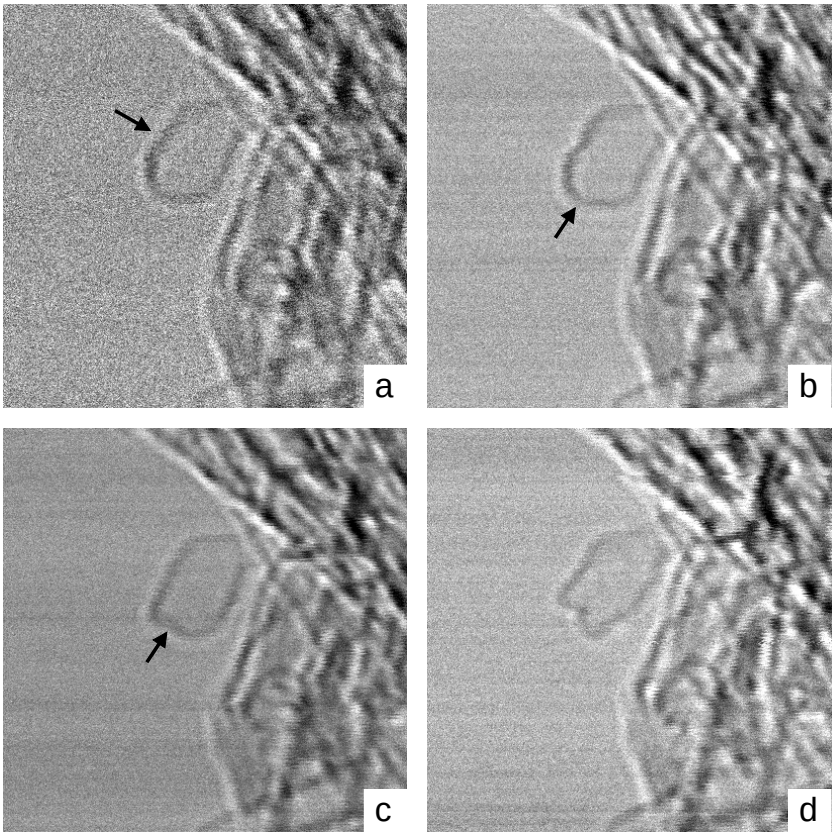

Figure 5.8: *Local irradiation of a fullerene like carbon structure. The black arrows indicate the zones irradiated during the successive irradiation cycles. Starting from a rounded carbon cage (a) we obtain after a first cycle a local ditching (b). Successive irradiation of one particule apex lead to the opening of the particle correspondently to the irradiated area.*

CHAPTER 6

CONCLUDING REMARKS

DIFFERENT ASPECTS regarding defects in carbon and boron nitride nanotubes have been investigated in this work using a combined experimental and theoretical approach. The purpose of this chapter is to summarise the main results of this thesis and to give an overview of new research lines that might be opened.

In the present thesis it has been shown that single point defects and dislocation lines can be produced and directly imaged in single walled boron nitride nanotubes through transmission electron microscopy techniques. Similar result had previously been reported on carbon based systems (carbon nanotubes and nanohorns) but the heteronuclear nature of BN makes the interpretation of experimental results more complex. For this purpose the structure and energetics of defective BN nanotubes have been calculated using a DFT-DFTB combined approach. It has thus revealed the existence of a strong interaction between boron and nitrogen vacancies which promotes the appearence of boron-nitrogen vacancy pairs instead of a random distribution of single vacancies. The analysis of the formation energies extended to larger defective structures demonstrates that long dislocation lines can be easily generated through a laddering mechanism by sequentially removing weakly bonded atoms close to vacancy sites and at the edges of dislocation lines. This mechanism may be general to a large variety of materials, particularly for heteronuclear structures. For the same reason such materials may also exhibit a tendency to form divacancies under electron irradiation. Similar effects, to those observed here in BN, may then be expected for other heteronuclear fullerene-like materials such as WS_2 nanotubes, MoS_2 fullerenes or BN nanohorns, where such defects may also control the reactivity properties.

Thermal stability of mono- and di-vacancies in h-BN has been investigated and migration paths have been derived using a DFTB-NEB combined method. The temperature dependence of migration energy barriers and diffusion coefficients has been obtained explicitely taking into account entropic terms in the Gibbs free energy. This study has shown that, com-

pared to analogous carbon structures, mono- and di-vacancies in h-BN have a higher thermal stability and vacancy mobility is limited up to temperatures of several hundreds of kelvin. This excludes that dislocation lines may appear within the microscope due to vacancy migration and nucleation and gives an additional confirmation to the existence of a laddering mechanism. Furthermore, we propose that thermal treatements in a temperature range between 680 and 1200 K may reduce the number of primary single vacancies: within this temperature range only boron vacancies are mobile and may be trapped by nitrogen vacancies forming divacancies complexes. These results may have a broader interest than the field of BN nanotubes since h-BN is used by industry for its particular thermal properties. The high melting point of h-BN makes this material a good substitute to graphite in numbers of technological application. Moreover, there is a rising interess in nuclear reactors technology on h-BN which is already used as coating for nuclear fuels. We expect that defects migration may have a critical importance for nuclear applications. As in the case of graphite, irradiated h-BN would store a Wigner energy that can be relieved by heating the material.

An analysis of the electronic properties of defective BN nanotubes has shown that defects do not alter significantly the band gap energy but defects introduce additional electronic shallow states within the electronic gap. Futhermore, all dislocation lines have an electronic structure similar to that of BN divacancies, which demonstrates that under irradiation BN SWNTs may have a very stable alteration of their electronic and optical properties. However, electron ground state calculations, presented in this thesis, are not able to predict in a quantitative way the influence of defects on the conductivity of the tubes. Higher level theory calculation have already been performed in the study of optical reponse and conduction properties of perfect BN nanotubes [32] and thus their extension to the case of defective tubes would be of a great interest. The interpretation of cathodoluminescence experiments on highly defective BN nanotubes [113] would require such accurate calculations.

The technological potential of electron irradiation of nanotubes is far from being realized to date. This is primarily because, until now, theory was not able to predict quantitatively the expected defect structures and the experiments were not performed with a sufficient spatial control. The total knock-on cross section has been derived for perfect carbon and boron nitride nanotubes and for defective carbon nanotubes.The electron beam energy dependence of atom emission probability has been calculated as a

function of the position of the atoms within the tube. This has allowed to predict quantitatively the quantity of sputtered atoms under electron irradiation and to design new optimised microscopy experiments. The analysis of knock on cross sections has given also a more direct confirmation of the existence of a laddering mechanism for the generation of long dislocation lines under electron irradiation. The method illustrated here for calculating knock-on cross sections, based on extended DFTB molecular dynamics symulations, could be adopted to the study of electron irradiation effects in other covalent bonded materials.

Using irradiation conditions optimised on the basis of calculated knock-on cross sections, we have shown how electron irradiation in a dedicated scanning transmission microscope can be used in a new top-down approach to locally change the tube structure with a nanometrical precision. We have thus demonstrated the possibility to change the chirality of limited sections of the tubes while preserving their crystallinity. This can eventually locally change, for particular chiralities, the electronic character of the tubes. Electron irradiation in a scanning transmission microscope opens then new opportunities for generating a wide variety of carbon-based quasi-1D conductive systems, from quantum wells to nanodiodes. This "nano-electron-lithography" procedure applied to carbon and BN nanotubes could be extended to other systems opening a new way for the designing of specific nanostructured materials.

Recent developements in sample holders for TEM microscopes allows simultaneus structural investigations (diffraction or HREM) with *in situ* conductivity mesurements. Considering that electron microscopy experiments may introduce defects in the structure of the tubes, experiments combining *in situ* electron irradiation and conductivity mesurements may directly record changes in the transport properties of the tubes induced by the appearence of defective sites.

Irradiation experiments for shaping the tubes have been conducted using an electron beam energy slightly above the atom emission energy threshold. In Fig. 6 is presented the local irradiation of a single walled carbon nanotubes using an acceleration voltage of 80 keV, slightly below the emission energy threshold. The serie of images shows that no morphological modification have been induced on the tube walls after an irradiation time of 15 minutes. This example shows that a correct control of the microscope acceleration voltage can thus allows to perform non destructive experiments on single nano-objects. Specific defective structures can thus be generated by electron beam irradiation and successively, lowering the

electron beam energy, post-analysed without inducing further structural modifications.

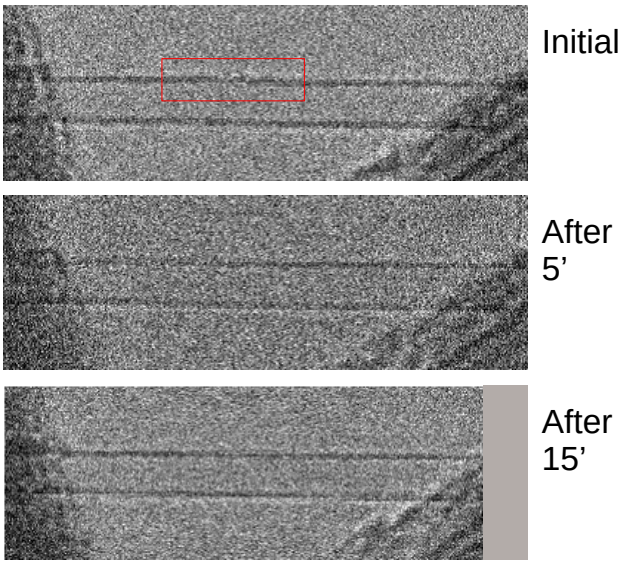

Figure 6.1: *Local irradiation of a single walled carbon nanotube with an electron beam energy below the energy threshold.*

A scanning transmission microscopes of new generation, the NION SUPER-STEM, will be installed in a short time at the Solid State Physics Laboratory of Orsay. The machine will have a spatial resolution of less than 1 Å, an energy resolution around 0.2 eV and should be able to operate at acceleration voltages as low as 40 keV. This specific characteristics will open the way to EELS experiments on individual defective sites, eventually produced *in situ* by electron irradiation.

List of Publications Related with the Thesis

- A. Zobelli, C.P. Ewels, A. Gloter, G. Seifert, O. Stephan, S. Csillag, C. Colliex, *Defective structure of BN nanotubes: From single vacancies to dislocation lines* Nano Lett. **6**, 1955 (2006)
- A. Zobelli, C.P. Ewels, A. Gloter, G. Seifert, C. Colliex, *Vacancy migration in hexagonal boron nitride* Phys. Rev. B **75**, 94104 (2007)
- A. Zobelli, A. Gloter, C.P. Ewels, G. Seifert, C. Colliex, *Electron knock-on cross section of carbon and boron nitride nanotubes* Phys. Rev. B **75**, 245402 (2007)
- A. Zobelli, A. Gloter, C.P. Ewels, G. Seifert, C. Colliex, *Shaping single walled nanotubes with an electron beam* To appear in Phys. Rev. B

BIBLIOGRAPHY

[1] H. Kroto, J. Health, S. O'Brian, R. Curl, and R. Smalley, *Buckminsterfullerene*, Nature **318**, 6042 (1985).

[2] S. Iijima, *Helical Microtubules of Graphitic Carbon*, Nature **354**, 56 (1991).

[3] N. Chopra, R. Luyken, K. Cherrey, V. Crespi, M. Cohen, S. Louie, and A. Zettl, *Boron Nitride Nanotubes*, Science **269**, 966 (1995).

[4] R. Tenne, L. Margulis, M. Genut, and G. Hodes, *Polyhedral and cylindrical structures of tungsten disulphide*, Nature **360**, 444 (1992).

[5] B. Biel, F. García-Vidal, A. Rubio, and F. Flores, *Anderson localization in carbon nanotubes: defect density and temperature effects*, Phys. Rev. Lett. **95**, 266801 (2005).

[6] M. Sammalkorpi, A. Krasheninnikov, A. Kuronen, K. Nordlund, and K. Kaski, *Mechanical properties of carbon nanotubes with vacancies and related defects*, Phys. Rev. B **70**, 245416 (2004).

[7] M. Hulman, V. Skákálova, S. Roth, and H. Kuzmany, *Raman spectroscopy of single-wall carbon nanotubes and graphite irradiated by γ rays*, J. Appl. Phys. **98**, 24311 (2005).

[8] V. Skákálova, U. Dettlaff-Weglikowska, and S. Roth, *Gamma-irradiated and functionalized single wall nanotubes*, Diam. Relat. Mater. **13**, 296 (2004).

[9] F. Beuneu, C. l'Huillier, J. Salvetat, J. Bonard, and L. Forro, *Modification of multiwall carbon nanotubes by electron irradiation: An ESR study*, Phys. Rev. B **59**, 5945 (1999).

[10] A. Kis, G. Csanyi, J. Salvetat, T. Lee, E. Couteau, A. Kulik, W. Benoit, J. Brugger, and L. Forró, *Reinforcement of single-walled carbon nanotube bundles by intertube bridging*, Nature Mater. **3**, 153 (2004).

[11] V. Basiuk, K. Kobayashi, T. Kaneko, Y. Negishi, E. Basiuk, and J. Saniger-Blesa, *Irradiation of single-walled carbon nanotubes with high-energy protons*, Nano Lett. **2**, 789 (2002).

[12] B. Khare, M. Meyyappan, M. Moore, P. Wilhite, H. Imanaka, and B. Chen, *Proton irradiation of carbon nanotubes*, Nano Lett. **3**, 643 (2003).

[13] C. Gómez-Navarro, P. de Pablo, J. Gómez-Herrero, B. Biel, F. Garcia-Vidal, A. Rubio, and F. Flores, *Tuning the conductance of single-walled carbon nanotubes by ion irradiation in the Anderson localization regime*, Nature Mat. **4**, 534 (2005).

[14] F. Banhart, *Irradiation effects in carbon nanostructures*, Rep.Prog. Phys. **62**, 1181 (1999).

[15] F. Banhart, J. Li, and A. Krasheninnikov, *Carbon nanotubes under electron irradiation: Stability of the tubes and their action as pipes for atom transport*, Phys. Rev. B **71**, 241408 (2005).

[16] A. Hashimoto, K. Suenaga, A. Gloter, K. Urita, and S. Iijima, *Direct evidence for atomic defects in graphene layers*, Nature **430**, 870 (2004).

[17] K. Suenaga, H. Wakabayashi, M. Koshino, Y. Sato, K. Urita, and S. Iijima, *Imaging active topological defects in carbon nanotubes*, Nature Nanotechnology **2**, 358.

[18] M. Yoon, S. Han, G. Kim, S. Lee, S. Berber, E. Osawa, J. Ihm, M. Terrones, F. Banhart, J. Charlier, N. Grobert, H. Terrones, P. Ajayan, and D. Tománek, *Zipper Mechanism of Nanotube Fusion: Theory and Experiment*, Phys. Rev. Lett. **92**, 75504 (2004).

[19] P. Ajayan, C. Colliex, P. Bernier, and J. Lambert, *Shape transformations in single layer carbon nanotubes*, Microsc. Microanal. Microstruct. **4**, 501 (1993).

[20] K. Urita, K. Suenaga, T. Sugai, H. Shinohara, and S. Iijima, *In-situ observation of thermal relaxation of interstitial-vacancy pair defects in a graphite gap*, Phys. Rev. Lett. **94**, 155502 (2005).

[21] T. Yuzvinsky, W. Mickelson, S. Aloni, G. Begtrup, A. Kis, and A. Zettl, *Shrinking a carbon nanotube*, Nano Lett. **6**, 2718 (2006).

[22] J. Huang, S. Chen, Z. Wang, K. Kempa, Y. Wang, S. Jo, G. Chen, M. Dresselhaus, and Z. Ren, *Superplastic carbon nanotubes*, Nature(London) **439**, 281 (2006).

[23] J. Huang, S. Chen, Z. R. Z. Q., Wang, D. Wang, M. Vaziri, Z. Suo, G. Chen, and M. Dresselhaus, *Kink Formation and Motion in Carbon Nanotubes at High Temperatures*, Phys. Rev. Lett. **97**, 75501 (2006).

[24] A. El-Barbary, R. Telling, C. Ewels, M. Heggie, and P. Briddon, *Structure and energetics of the vacancy in graphite*, Phys. Rev. B **68**, 144107 (2003).

[25] A. Krasheninnikov, P. Lehtinen, A. Foster, and R. Nieminen, *Bending the rules: Contrasting vacancy energetics and migration in graphite and carbon nanotubes*, Chem. Phys. Lett. **418**, 132 (2006).

[26] C. Ewels, M. Heggie, A. El-Barbary, J. Goss, A. Zobelli, and P. Briddon, *Third neighbour re-hybridisation: a new class of metastable defects*, Nature Mat. (2007).

[27] J. Li and F. Banhart, *The engineering of hot carbon nanotubes with an electron beam*, Nano Lett. **4**, 1143 (2004).

[28] T. Yuzwinsky, A. Fennimore, W. Mickelson, C. Esquivias, and A. Zettl, *Precision cutting of nanotubes with a low-energy electron beam*, Appl. Phys. Lett. **86**, 53109 (2005).

[29] A. Rubio, J. Corkill, and M. Cohen, *Theory of graphitic boron nitride nanotubes*, Phys. Rev. B **49**, 5081 (1994).

[30] A. Loiseau, F. Willaime, N. Demoncy, G. Hug, and H. Pascard, *Boron nitride nanotubes with reduced numbers of layers synthesized by arc discharge*, Phys. Rev. Lett. **76**, 4737 (1996).

[31] R. S. Lee, J. Gavillet, M. L. de la Chapelle, A. Loiseau, J.-L. Cochon, D. Pigache, J. Thibault, and F. Willaime, *Catalyst-free synthesis of boron nitride single-wall nanotubes with a preferred zig-zag configuration*, Phys. Rev. B **64**, 121405(R) (2001).

[32] L. Wirtz, A. Marini, and A. Rubio, *Excitons in boron nitride nanotubes: dimensionality effects*, Phys. Rev. Lett. **96**, 126104 (2006).

[33] C. Park, C. Spataru, and S. Louie, *Excitons and many-electron effects in the optical response of single-walled boron nitride nanotubes*, Phys. Rev. Lett. **96**, 126105 (2006).

[34] R. Arenal, O. Stéphan, M. Kociak, D. Taverna, A. Loiseau, and C. Colliex, *Electron energy loss spectroscopy measuremen t of the optical gaps on individual boron nitride single-walled and multiwalled nanotubes*, Phys. Rev. Lett. **95**, 127601 (2005).

[35] T. Schmidt, R. Baierle, P. Piquini, and A. Fazzio, *Theoretical study of native defects in BN nanotubes*, Phys. Rev. B **67**, 113407 (2003).

[36] P. Piquini, R. Baierle, T. Schmidt, and A. Fazzio, *Formation energy of native defects in BN nanotubes: an ab inition study*, Nanotechnology **16**, 827 (2005).

[37] W. Moon and H. Hwang, *Molecular-dynamics simulations of defect formation energy in boron nitride nantubes*, Phys. Lett. A **320**, 446 (2004).

[38] Y. Miyamoto, A. Rubio, S. Berber, M. Yoon, and D. Tomànek, *Spectroscopic characterization of Stone-Wales defects in nanotubes*, Phys. Rev. B **69**, 121413 (2004).

[39] H. Bettinger, T. Dumitrica, G. Scuseria, and B. Yakobson, *Mechanically induced defects and strength of BN nanotubes*, Phys. Rev. B **65**, 41406 (2002).

[40] T. Dumitrica, H. Bettinger, G. Scuseria, and B. Yakobson, *Thermodynamics of yield in boron nitride nanotubes*, Phys. Rev. B **68**, 85412 (2003).

[41] R. A. de la Concha, *Synthése de nanotubes de nitrure de bore: études de la structure et des propriétés vibrationnelles et électroniques*, PhD thesis, Université Paris-Sud, 2005.

[42] E. Kirkland, *Advanced Computing in Electron Microscopy*, Plenum Press, New York, 1998.

[43] P. Hohenberg and W. Kohn, *Inhomogeneous Electron Gas*, Phys. Rev. **136**, B864 (1964).

[44] W. Kohn and L. Sham, *Self-Consistent Equations Including Exchange and Correlation Effects*, Phys. Rev. **140**, A1133 (1965).

[45] R. Jones and P. Briddon, *The ab initio cluster method and the dynamics of defects in semiconductors*, volume 51A of *Semiconductors and Semimetals*, chapter 6, Academic Press, Boston, 1998.

[46] P. Briddon, *Ab initio modelling techniques applied to c-Si*, volume 20 of *EMIS Datareviews Series*, chapter 6-9, INSPEC, Institute of Electrical Engineers, London, 1999.

[47] P. Briddon and R. Jones, *LDA calculations using a basis of Gaussian orbitals*, Phys. Status Solidi B **217**, 131 (2000).

[48] C. Hartwingster, S. Goedecker, and J. Hutter, *Relativistic separable dual-space Gaussian pseudopotentials from H to Rn*, Phys. Rev. B **58**, 3641 (1998).

[49] C. Goringe, D. Bowler, and E. Hernandez, *Tight-binding modelling of materials*, Rep. Prog. Phys. **60**, 1447 (1997).

[50] T. Frauenheim, G. Seifert, M. Elstner, T. Niehaus, C. Kohler, M. Amkreutz, M. Sternberg, Z. Hajnal, A. Di Carlo, and S. Suhai, *Atomistic simulations of complex materials: ground-state and excited-state properties*, J. Phys.: Condens. Matter **14**, 3015 (2002).

[51] W. Foulkes and R. Haydock, *Tight-binding models and density-functional theory*, Phys. Rev. B **39**, 12520 (1989).

[52] H. Eschring, *Optimised LCAO Method and the electronic structure of extended systems*, Akademie-Verlag, Berlin, 1988.

[53] J. Knaup, B. Hourahine, and T. Frauenheim, *Initial Steps toward Automating the Fitting of DFTB* $E_{rep}(r)$, J. Phys. Chem. A **111**, 5637 (2007).

[54] M. Elstner, D. Porezag, G. Jungnickel, J. Elsner, M. Haugk, T. Frauenheim, S. Suhai, and G. Seifert, *Self-consistent-charge density-functional tight-binding method for simulations of complex materials properties*, Phys. Rev. B **58**, 7260 (1998).

[55] C. Köhler, G. Seifert, and T. Frauenheim, *Density functional based calculations for* $\mathrm{Fe_n}(n \leq 32)$, Chem. Phys. **309**, 23 (2005).

[56] A. Köster, R. Flores, G. Geudtner, A. Goursot, T. Heine, S. Patchkovskii, J. Reveles, A. Vela, and D. Salahub, deMon 2004, NRC, Ottawa, Canada, 2004.

[57] B. Aradi, B. Hourahine, C. Koehler, and T. Frauenheim, *Sparse matrix based implementation of the DFTB method.*, J. Phys. Chem. A **111**, 5678 (2007).

[58] D. Porezag, T. Frauenheim, T. Köhler, G. Seifert, and R. Kaschner, *Construction of tight-binding-like potentials on the basis of density-functional theory: Application to carbon*, Phys. Rev. B **51**, 12947 (1995).

[59] J. Widany, Köhler, M. Sternberg, D. Porenzag, G. Jungnickel, and G. Seifert, *Density-functional-based construction of transferable nonorthogonal tight-binding potentials for B,N,BN,BH and NH*, Phys. Rev. B **53**, 4443 (1996).

[60] G. Seifert, P. Fowler, D. Porezag, and T. Frauenheim, *Boron-nitrogen analogues of the fullerenes: Electronic and structural properties*, Chem. Phys. Lett. **268**, 352 (1997).

[61] K. Rogers, P. Fowler, and G. Seifert, *Chemical versus steric frustration in boron nitride heterofullerene polyhedra*, Chem. Phys. Lett. **332**, 43 (2000).

[62] P. Fowler, K. Rogers, G. Seifert, M. Terrones, and H. Terrones, *Pentagonal rings and nitrogen excess in fullerene-based BN cages and nanotubes caps*, Chem. Phys. Lett. **299**, 359 (1999).

[63] M. Meyer, *Diffusion et défauts ponctuels: quel est l'apport de la simulation numérique?*, J. Phys. III France **5**, 1771 (1995).

[64] G. Mills and H. Jónsson, *Quantum and thermal effects in H_2 dissociative adsorption: Evaluation of free energy barriers in multidimensional quantum systems*, Phys. Rev. Lett. **72**, 1124 (1994).

[65] G. Henkelman, B. Uberuaga, and H. Jónsson, *A climbing image nudged elastic band method for finding saddle points and minimum energy paths*, J. Chem. Phys. **113**, 9901 (2000).

[66] G. Henkelman and H. Jónsson, *Improved tangent estimate in the nudged elastic band method for finding minimum energy paths and saddle points*, J. Chem. Phys. **113**, 9978 (2000).

[67] G. Fischer, R. Barthel, and G. Seifert, *Molecular dynamics study of the reaction $C_3 + H_3^+$*, Eur. Phys. J. D **35**, 479 (2005).

[68] W. Orellana and H. Chacham, *Stability of native defects in hexagonal and cubic boron nitride*, Phys. Rev. B **63**, 125205 (2001).

[69] A. Golovacheva and P. D'yachkov, *Effect of intrinsic defects on the electronic structure of BN nanotubes*, JETP Lett. **82**, 737 (2005).

[70] M. Khusidman and V. Neshpor, *F centres in hexagonal boron nitride enriched with the B^{10} isotope*, Sov. Phys. Solid State **10**, 975 (1968).

[71] A. Katzir, J. T. Suss, A. Zunger, and A. Halperin, *Point defects in hexagonal boron nitride. I. EPR, thermoluminescence, and thermally-stimulated-current measurements*, Phys. Rev. B **11**, 2370 (1975).

[72] E. Y. Andrei, A. Katzir, and J. T. Suss, *Point defects in hexagonal boron nitride. III. EPR in electron-irradiated BN*, Phys. Rev. B **13**, 2831 (1976).

[73] T. Kolodiazhnyi and D. Golberg, *Paramagnetic defects in boron nitride nanostructures*, Chem. Phys. Lett. **413**, 47 (2005).

[74] A. Panich, A. Shames, N. Froumil, C. Tang, and Y. Bando, *Magnetic resonance study of multiwall boron nitride nanotubes*, Phys. Rev. B **72**, 85307 (2005).

[75] H. Himmel, *Structural motifs and reactivity of small molecules containing subvalent Group 13 elements: matrix isolation and quantum chemical studies*, Dalton Trans. **2003**, 3639 (2003).

[76] S. Iijima, M. Yudasaka, R. Yamada, S. Bandow, K. Suenaga, F. Kokai, and K. Takahashi, *Nano-aggregates of single-walled graphitic carbon nano-horns*, Chem. Phys. Lett. **309**, 165 (1999).

[77] W. Moon and H. Hwang, *A force field approach of structures and formation energy of defects of boron nitride nanotubes with tetragon-optagon pairs*, Mat. Lett. **58**, 2331 (2004).

[78] D. Golberg, Y. Bando, M. Eremets, K. Takemura, K. Kurashima, K. Tamiya, and H. Yusa, *Boron nitride nanotube growth defects and their annealing-out under electron irradiation*, Chem. Phys. Lett. **279**, 191 (1997).

[79] A. Rodríguez and L. del Río Caballero, *SIMULATEM: a program for the multislice simulation of images and diffraction patterns of non-crystalline objects*, Rev. LatinAm. Met. Mat. **21**, 255 (2001).

[80] G. Hinman, A. Haubold, J. Gardner, and J. Layton, *Vacancies and interstitial clusters in irradiated graphite*, Carbon **8**, 341 (1970).

[81] E. Asari, M. Katajima, K. Nakamura, and T. Kawabe, *Thermal relaxation of ion-irradiation damage in graphite*, Phys. Rev. B **47**, 11143 (1993).

[82] R. Telling, C. Ewels, A. El-Barbary, and M. Heggie, *Wigner defects bridge the graphite gap*, Nature Mat. **2**, 333 (2003).

[83] M. Scheffler and J. Dabrowski, *Parameter-free calculations of total energies, interatomic forces and vibrational netropies of defects in semiconductors*, Phil. Mag. A **58**, 107 (1988).

[84] E. Rauls and T. Frauenheim, *Entropy of point defects calculated within periodic boundary conditions*, Phys. Rev. B **69**, 155213 (2004).

[85] T. Frauenheim, G. Seifert, M. Elstner, Z. Hajnal, G. Jungmickel, D. Porezag, S. Suhai, and R. Scholz, *A self-consistent charge density-functional based tight-binding method for predictive materials simulations in physics*, Phys. Satus Solidi B **217**, 41 (2000).

[86] R. Egerton, P. Li, and M. Malac, *Radiation damage in the TEM and SEM*, Micron **35**, 399 (2004).

[87] R. Egerton, *Electron Energy-Loss Spectroscopy in the Electron Microscope*, Springer, 1996.

[88] D. Taverna, M. Kociak, V. Charbois, and L. Henrard, *Electron energy-loss spectrum of an electron passing near a locally anisotropic nanotube*, Phys. Rev. B **66**, 235419 (2002).

[89] E. Pop, D. Mann, Q. Wang, K. Goodson, and H. Dai, *Thermal conductance of an individual single-wall carbon nanotube above room temperature*, Nano Lett. **6**, 96 (2006).

[90] K. Niwase, *Irradiation-induced amorphization in graphite*, Phys. Rev. B **52**, 15785 (1995).

[91] K. Niwase, *Formation of dislocation dipoles in irradiated graphite*, Mater. Sci. Eng., A **400**, 101 (2005).

[92] J. Kotakoski, A. Krasheninnikov, and K. Nordlung, *Energetics, structure, and long-range interaction of vacancy-type defects in carbon nanotubes: Atomistic simulations*, Phys. Rev. B **74**, 245420 (2006).

[93] A. Krashenninikov, F. Banhart, J. Li, A. Foster, and R. Nieminen, *Stability of carbon nanotubes under electron irradiation: Role of tube diameter and chirality*, Phys. Rev. B **72**, 125428 (2005).

[94] M. Fanciulli, *Electron paramagnetic resonance and relaxation in BN and BN:C*, Phil. Mag. B **76**, 363 (1997).

[95] F. Banhart, *Irradiation of Carbon Nanotubes with a Focused Electron Beam in the Electron Microscope*, J. Mater. Sci. **41**, 4505 (2006).

[96] V. Crespi, N. Chopra, M. Cohen, A. Zettl, and S. Louie, *Anisotropic electron-beam damage and the collapse of carbon nanotubes*, Phys. Rev. B **54**, 5927 (1996).

[97] B. Smith and D. Luzzi, *Electron irradiation effects in single wall carbon nanotubes*, J. Appl. Phys. **90**, 3509 (2001).

[98] N. Mott, *The scattering of fast electrons by atomic nuclei*, Proc. Roy. Soc. A **124**, 425 (1929).

[99] N. Mott, *The polarisation of electrons by double scattering*, Proc. Roy. Soc. A **135**, 429 (1932).

[100] J. Motz, H. Olsen, and H. Koch, *Electron scattering without atomic or nuclear excitation*, Rev. Mod. Phys. **36**, 881 (1964).

[101] W. McKinsley and H. Feshbach, *The Coulomb scattering of relativistic electrons by nuclei*, Phys. Rev. **74**, 1759 (1948).

[102] F. Seitz and J. Koehler, *Solid State Physics*, volume 2, Academic Press Inc, New York, 1956.

[103] T. Loponen, A. Krasheninnikov, M. Kaukonen, and R. Nieminen, *Nitrogen-doped carbon nanotubes under electron irradiation simulated with a tight-binding model*, Phys. Rev. B **74**, 073409 (2006).

[104] B. Smith, M. Monthioux, and D. Luzzi, *Encapsulated C_{60} in carbon nanotubes*, Nature **396**, 323 (1998).

[105] D. Luzzi and B. Smith, *Carbon cage structures in SWNT: A new class of materials*, Carbon **38**, 1751 (2000).

[106] E. Hernández, V. Meunier, B. Smith, R. Rurali, H. Terrones, M. B. Nardelli, M. Terrones, D. Luzzi, and J.-C. Charlier, *Fullerene coalescence in nanopeapods: a path to novel tubular carbon*, Nano Lett. **3**, 1037 (2003).

[107] W. Mickelson, S. Aloni, W.-Q. Han, J. Cumings, and A. Zettl, *Packing C_{60} in boron nitride nanotubes*, Science **300**, 467 (2003).

[108] A. Zettl, J. Cumings, W.-Q. Han, and W. Mickelson, Boron nitride nanotube peapods, in *Structural and electronic properties of molecular nanostructures*, volume 633 of *AIP Conference Proceedings*, page 140, 2002.

[109] F. Ding, K. Jiao, M. Wu, and B. Yakobson, *Pseudoclimbing and dislocation dynamics in superplastic nanotubes*, Phys. Rev. Lett. **98**, 75503 (2007).

[110] F. Ding, K. Jiao, M. Wu, and B. Yakobson, *How evaporating carbon nanotubes retain their perfection?*, Nano Lett. **7**, 681 (2007).

[111] L. Chico, V. Crespi, L. Benedict, S. Louie, and M. Cohen, *Pure carbon nanoscale devices: nanotube heterojunctions*, Phys. Rev. Lett. **76**, 971 (1996).

[112] L. Ruppalt and J. Lyding, *Metal-induced gap states at a carbon-nanotube intramolecular heterojunction observed by scanning tunneling microscopy*, Small **3**, 280 (2007).

[113] Q. Huang, Y. Bando, A. Sandanayaka, C. Tang, J. Wang, T. Sekiguchi, C. Zhi, D. Golberg, Y. Araki, O. Ito, F. Xu, and L. Gao, *Photoinduced charge injection and bandgap-engineering of high-specific-surface-area BN nanotubes using a zinc phthalocyanine monolayer*, Small **3**, 1330 (2007).